CHAPTER NO.

FULLY NONLINEAR POTENTIAL FLOW MODELS USED FOR LONG WAVE RUNUP PREDICTION

(S. Grilli, Department of Ocean Engineering, University of Rhode Island, Kingston 02881, RI)

Abstract

A review of Boundary Integral Equation methods used for long wave runup prediction is presented in this chapter.

In Section 1, a brief literature review is given of methods used for modeling long wave propagation and of generic methods and models used for modeling highly nonlinear waves. In Section 2, fully nonlinear potential flow equations are given for the Boundary Element Model developed by the author, including boundary conditions for both wave generation and absorption in the model. In Section 3, details are given for the generation of waves in the model using various methods (wavemakers, free surface potential, internal sources). In Section 4, the numerical implementation of the author's model based on a higher-order Boundary Element Method is briefly presented. In Section 5, many applications of the model are given for the computation of wave propagation, shoaling, breaking or runup on slopes, and interaction with submerged and emerged structures. The last application presented in this Section is the Benchmark #3 problem for the runup of solitary waves on a vertical wall that was proposed as part of the "International Workshop on Long-wave Runup Models (San Juan Island, WA, USA, 09/95). Finally, Appendices A to F give more details about various aspects of the numerical model.

1. Introduction

1.1. Modeling of long wave propagation, shoaling, breaking and runup

Over the past forty years, ocean wave propagation, shoaling, breaking or runup over a slope, have been the object of numerous theoretical and numerical studies, particularly for the case of—essentially two-dimensional—long waves or swells generated by wind (wind waves) or earthquakes (tsunamis).

Main approaches pursued were based on using : (i) linear or nonlinear Shallow Water Wave equations (Carrier and Greenspan [8] 1958, Carrier [7] 1966, Camfield and Street [6] 1969, Hibberd and Peregrine [50] 1979, Kobayashi *et al.* [57] 1989, and Synolakis [89] 1990); (ii) Boussinesq or parabolic approximations of Boussinesq equations (Peregrine [72] 1967, Pedersen and Gjevik [71] 1983, Freilich and Guza [24] 1984, Zelt and Raichlen [97] 1990, and

Kirby [55] 1991) [a]. Most of the methods used in these works, however, are based on first- or low-order theories whose assumptions—for instance small amplitude, mildly nonlinear waves, or mild bottom slope—may no longer be valid for waves that, due to shoaling, may be close to breaking at the top of a slope (i.e., strongly nonlinear) before they run-up or break on the slope.

Until recently, state-of-the-art methods used for predicting characteristics of highly nonlinear waves shoaling over a sloping bottom up to impending breaking (e.g., shoaling coefficients, breaker height and kinematics), were based on higher-order expansion methods originally developed for waves of permanent form over constant depth (Stiassine and Peregrine [84] 1980, Peregrine [73] 1983, Sobey and Bando [82] 1991). These methods, however, by nature cannot include effects of finite bottom slope or changes of wave form during shoaling. Long waves, in particular, are known to become strongly asymmetric when shoaling over a gentle slope and approaching breaking (e.g., experiments by Skjelbreia [78] 1987, Grilli *et al.*[41] 1994), an effect that is not included in the above approaches. Griffiths *et al.* [28] 1992, compared measurements of internal kinematics of periodic waves shoaling up a 1:30 slope with predictions of the 5th-order Stokes theory, the 9th- and higher-order streamfunction theory, and the full nonlinear model by New *et al.* [65]. They found that horizontal velocities were correctly predicted by most theories below still water level but [b], in the high crest region, low-order theories underpredicted velocities by as much as 50% whereas predictions of the fully nonlinear theory were quite good up to the crest [c]. Grilli *et al.*[41] 1994 showed that computations with a fully nonlinear potential model quite well predicted the shape of solitary waves during shoaling over a 1:35 slope, as measured in well-controlled laboratory experiments. The agreement was within 2%, both in time and space, up to the breaking point. The same computations also showed that, even for long waves, horizontal velocities under a shoaling wave crest eventually become significantly non-uniform over depth (in some cases by more than 200%), an effect which is neglected in (first-order) nonlinear shallow water wave theories.

Grilli *et al.*[40] 1994 and Wei *et al.*[93] 1995 recently compared predictions of classical (i.e., weakly nonlinear and weakly dispersive) and modified (i.e., with improved dispersion characteristics and/or full nonlinearity) Boussinesq models (BM) to the full nonlinear potential flow solution—used as a reference—for the shoaling of solitary waves over slopes 1:100 to 1:8, up to the breaking point. They found that, in the region of large nonlinearity where the ratio wave height over depth is larger than 0.5, the classical BM significantly overpredicts crest height and particle velocity. This model also predicts spurious secondary troughs behind the main crest. The fully nonlinear BM, however, was found much more accurate in predicting both wave shape and horizontal velocity under the crests, from bottom to surface. Similar conclusions were reached for the propagation of highly nonlinear undular bores over constant depth.

---

[a] The reader can find details on various wave theories and summaries of some of the above referenced works in Mei [63] 1983, and Dean and Dalrymple [17] 1984.

[b] see Ref.[17] for definitions of these wave theories.

[c] Note that these comparisons were only done for a mild slope (i.e, with limited bottom effect) and for cases in which breaking occurred by spilling. The authors pointed out that "all theories are grossly in error when compared to severe plunging breakers".

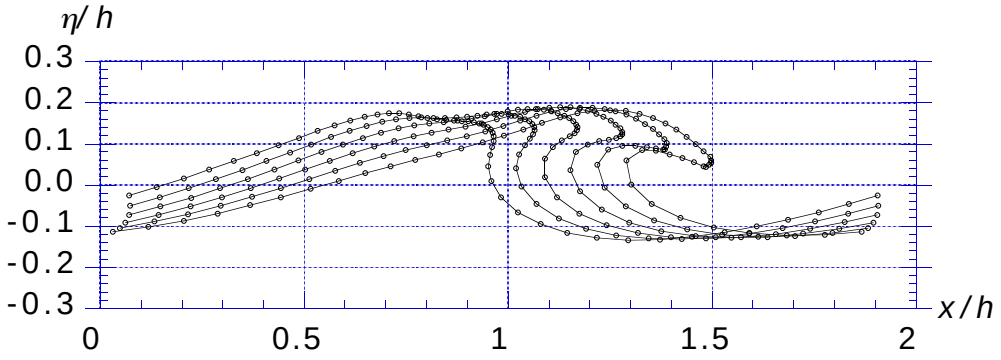

Fig. 1. Instability by plunging breaking of a large sine wave over constant depth h, as computed with the model by Grilli *et al.* [36], 1989. Initial wave height is $H/h = 0.333$, length $L/h = 1.85$, and period $T\sqrt{g/L} = 2.50$. A periodicity condition is used in the model on lateral boundaries, to create a situation similar to that examined by Longuet-Higgins and Cokelet [62]. Symbols (○) denote BEM discretization nodes, identical to individual fluid particles whose motion is calculated in time.

In the above studies, it is thus seen that a correct representation of both the shape and kinematics of strongly nonlinear long waves can only be achieved when using highly or fully nonlinear models, i.e., models in which no approximation are introduced for the free surface boundary conditions. Even for long waves with very small nonlinearity when approaching the deep water end of a slope, it is also seen that long distances of propagation over a gentle slope can make such waves both strongly asymmetric and nonlinear towards the top of the slope, whether they subsequently break or simply run up the slope.

These conclusions justify using fully nonlinear models for studying shoaling, runup or breaking, of large long waves close to the shore.

1.2. Modeling of highly nonlinear waves

Over the past twenty years, considerable efforts have been devoted to developing increasingly accurate and efficient models for fully nonlinear water waves at sea. Starting with the key work by Longuet-Higgins and Cokelet[62] 1976, the most successful approaches so far have been based on describing the physical problem based on potential flow theory (i.e., neglecting both viscous and rotational effects on the wave flow) while keeping full nonlinearity in the free surface boundary conditions (i.e., a "Fully Nonlinear Potential Flow" (FNPF) model). Most methods have also used a representation of the flow that allows for multi-valued free surface elevations appearing during breaking (i.e., a mixed Eulerian-Lagrangian representation; see Fig. 1). Despite its intrinsic limitations, potential flow theory has been shown in many applications to model the physics of wave propagation and overturning in deep water, and wave shoaling up to breaking or runup over slopes, with a surprising degree of accuracy (e.g., Dommermuth *et al.*[20], Grilli[30], and Grilli *et al.*[41,47,48]; see below for a discussion).

Many quite exhaustive reviews of the relevant literature have been published to date and can be consulted for more information (e.g., Grilli[30], Grilli *et al.*[36,38], Peregrine[73,74], Yeung[95]). For the purpose of introducing the present numerical model and its applications to long wave propagation and runup, the following is a brief description of the main steps in

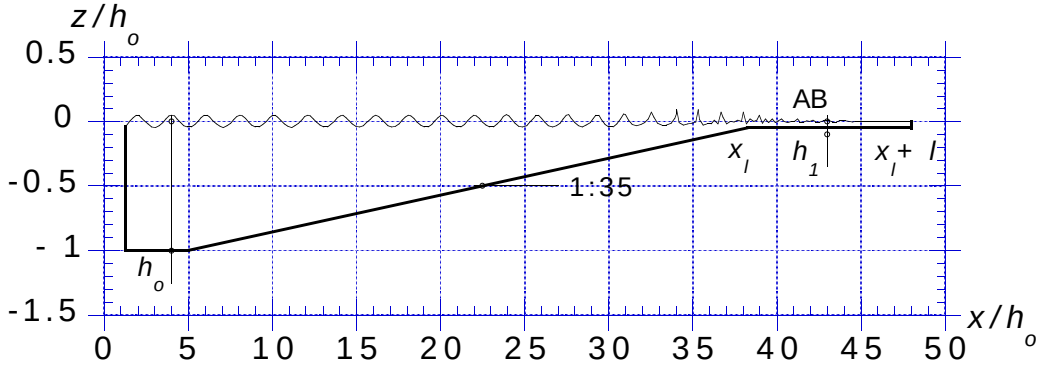

Fig. 2. Generation and shoaling over a 1:35 slope of numerically exact periodic waves (streamfunction waves) with initial height $H_o/h_o = 0.1$ and period $T\sqrt{g/h_o} = 3.55$, as computed by Grilli and Horrillo [31]. To achieve zero-mass-flux and thus constant volume in the computational domain, waves are generated on top of an opposite current equal to the mean mass transport velocity. An absorbing beach (AB) of length l, with counteracting free surface pressure, is specified for $x_l' > 38$ over a shelf of depth $h_1 = 0.05$.

the development of FNPF models that will identify key elements of the problem. Starting with Longuet-Higgins and Cokelet [62], the problem was first formulated in deep water by assuming that waves were two-dimensional in the vertical plane—i.e., long crested—and periodic in space, thus making it possible to use conformal mapping techniques which wrap the computational domain on itself and eliminate the need for lateral boundaries in the model. Doing so, deep water plunging breakers could be calculated up to touch down of the jet on the free surface (Fig. 1). Along this line, various increasingly accurate and stable numerical formulations were proposed for both deep and constant water depth, and applications sometimes also included periodic structures (Dold and Peregrine [18], New *et al.*[65], and Vinje and Brevig [92]) [d]. Results of such computations were compared to laboratory measurements and found to agree with them up to the latest stages of wave breaking, thus confirming the validity of the FNPF approach to model the physics of wave breaking far from the shore (e.g., Dommermuth *et al.* [20]).

Most of the previous and similar models—except perhaps the improvement of Dold and Peregrine's model by Cooker[13] and Cooker *et al.*[15]—due to their intrinsic nature, were unable or had the greatest difficulties generating and propagating waves over complex bottom topography. This, however, is required for solving problems of wave shoaling and breaking in shallow water and over beaches, and problems of wave interaction with coastal structures and runup on slopes. To solve such problems, models working in the so-called *physical space* must be used which brings additional problems of wave generation and/or wave absorption in the computational domain and of treatment and representation of corners in the modeled boundary (these aspects are discussed in individual Sections below). Early works that addressed problems of wave generation by a wavemaker in the physical space are the model by Kim *et al.*[54] which, however, was limited to non-breaking (single-value elevation) waves, and the model by Lin *et al.*[60], who used and improved Vinje and Brevig's formulation but somewhat restricted their scope of application. More recent models working

[d] Also note the somewhat different method introduced by Zaroodny and Greenberg [96], and Baker *et al.*[5], based on a vortex sheet approach.

in the physical space can accommodate almost arbitrary incident waves, complex bottom topography, and moving boundaries (e.g., Cointe[10], Grilli *et al.*[36,39], Klopman[56], Ohyama and Nadaoka[67]). An example of such recent computations for the shoaling and absorption of periodic waves over a gentle slope is given in Fig. 2.

In most FNPF applications to date, the governing (Laplace's) equation is solved using a higher-order Boundary Element Method (BEM), either based on Green's identity or on Cauchy integral theorem formulations, and on time integrating the free surface boundary condition using either a time marching predictor-corrector method [62,92] (Runge-Kutta and/or Adams-Bashforth-Moulton schemes) or a Taylor series expansion method[18,36]. The FNPF model by Grilli *et al.*[36,39,46], which will be used in the present applications, was developed in the physical space following the strategy of deep water and constant depth nonlinear wave models mentioned above (e.g., Dold and Peregrine [18]). It is based on a mixed Eulerian-Lagrangian representation with full nonlinearity in the free surface boundary conditions. FNPF equations are solved by a BEM based on Green's identity, which easily accounts for arbitrary bottom topography and almost arbitrary incident wave conditions. Development of this model was carried out under a 2D formulation, which makes the model directly applicable to shoaling and breaking and/or runup over arbitrary slopes of normally incident long crested waves, without any approximation on the wave shape or on the free surface boundary conditions [e]. Many validations (both analytical and experimental) of Grilli *et al.*'s model and of its more recent improved versions were carried out, mostly using solitary waves, for : (i) shallow water wave generation, propagation, and reflection, by Grilli and Svendsen[45,47]; (ii) wave runup over a steep slope, by Svendsen and Grilli[87]; (iii) shoaling and breaking over both gentle and steep slopes, by Grilli *et al.*[41,48]; (iv) wave impact on a mixed breakwater, by Grilli *et al.*[33,35]; and (v) wave propagation over a submerged obstacle, by Grilli *et al.*[32,34].

For completeness, other fully nonlinear wave models used for calculating wave propagation and runup on slopes (most of them based on boundary integral formulations) will be mentioned. These models have either inherently been limited to non-breaking waves (Fenton and Rienecker [23] 1982, Nakayama [64] 1983, Liu *et al.*[61] 1992) or have represented extensions (e.g., to axisymmetric problems) or variant of existing methods—mostly by[18,62,92]—(Isaacson [51] 1982, Jansen [53] 1986, Dommermuth and Yue [19] 1987, Gravert [26] 1987, Greenhow [27] 1987, Tanaka *et al.* [91] 1987, Romate [76] 1990, Seo and Dalrymple [77] 1990).

Detailed equations and numerical procedures for Grilli *et al.*'s wave model are presented in Sections 2,3, and 4, and applications of the model to cases of long wave propagation in shallow water and runup on slopes are presented in Section 5.

[e] Note that all elements in Grilli *et al.*'s model were selected to allow implementation of a three-dimensional model as a direct extension of the 2D formulation. This is unlike 2D FNPF models based on complex variable formulations. Such extensions of FNPF models in the physical space to three-dimensional problems have already been proposed by Romate [75,76] 1990, Yue[94] 1992, and Broeze[3] 1993, but still face challenges posed by the formidable size of the computational problem as well as problems of both representation of the free surface and boundary conditions at intersections between side walls and the free surface.

2. Mathematical model

Governing equations for the two-dimensional FNPF model by Grilli *et al.* [36,46] and its most recent extensions are presented in the next subsections. Full nonlinearity is maintained in the free surface boundary conditions, and time integration of these conditions is based on higher-order Taylor expansions, for both the free surface position and the potential. No-flow boundary conditions are prescribed along solid boundaries of the domain (bottom, coastal structures) and arbitrary waves are generated in the model, either by specifying an initial wave on the free surface, either by simulating a wavemaker at the open-sea boundary of the computational domain (as in laboratory experiments), or by using a line of internal sources. Finally, wave energy absorption can be specified in the model using an absorbing beach.

2.1. Governing equations and solid boundary conditions

The velocity potential $\phi(\mathbf{x},t)$ is used to describe inviscid irrotational 2D flows in the vertical plane (x,z), where the velocity is given by $\mathbf{u} = \boldsymbol{\nabla}\phi = (u,w)$. Continuity equation in the fluid domain $\Omega(t)$, with boundary $\Gamma(t)$, is a Laplace's equation for the potential (see Fig. 3 for definitions),

$$\nabla^2\phi = 0 \qquad \text{in } \Omega(t) \tag{1}$$

On the free surface $\Gamma_f(t)$, ϕ satisfies the nonlinear kinematic and dynamic boundary conditions,

$$\frac{D\mathbf{r}}{Dt} = \mathbf{u} = \boldsymbol{\nabla}\phi \qquad \text{on } \Gamma_f(t) \tag{2}$$

$$\frac{D\phi}{Dt} = -gz + \frac{1}{2}\,\boldsymbol{\nabla}\phi\cdot\boldsymbol{\nabla}\phi - \frac{p_a}{\rho} \qquad \text{on } \Gamma_f(t) \tag{3}$$

respectively, with $\mathbf{r}$ the position vector of a free surface fluid particle, g the acceleration due to gravity, z the vertical coordinate (positive upwards, and $z = 0$ at the undisturbed free surface), p_a the atmospheric pressure, and ρ the fluid density. The material derivative is defined as,

$$\frac{D}{Dt} \equiv \frac{\partial}{\partial t} + \mathbf{u}\cdot\boldsymbol{\nabla} \tag{4}$$

Along the stationary bottom Γ_b and other fixed boundaries denoted as Γ_{r2}, a no-flow condition is prescribed as,

$$\boldsymbol{\nabla}\phi\cdot\mathbf{n} \equiv \overline{\frac{\partial\phi}{\partial n}} = 0 \qquad \text{on } \Gamma_b \text{ and } \Gamma_{r2} \tag{5}$$

in which $\mathbf{n}$ is the unit outward normal vector.

2.2. Boundary conditions for wave generation

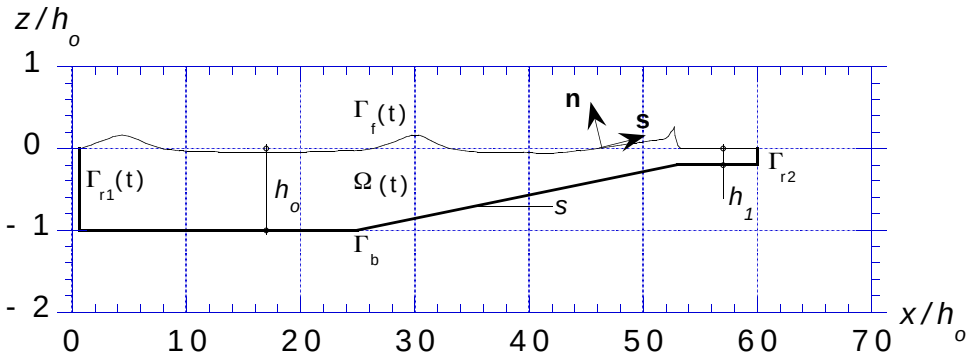

Fig. 3. Typical computational domain for wave shoaling over a slope, with definition of various boundaries. The domain has a slope s, terminated by a shelf of depth h_1 at its upper part (case where waves break before reaching the top of the slope). The sketched free surface profile corresponds to a cnoidal wave of initial height $H_o/h_o = 0.2$ and period $T\sqrt{g/h_o} = 25$, generated by a piston wavemaker on boundary $\Gamma_{r1}(t)$.

In models developed in the physical space, it is necessary to generate waves at one extremity of the computational domain. Kim *et al.*[54], Lin *et al.*[60], Cointe[10], Dommermuth *et al.*[19,20], and Grilli *et al.*[36] generated waves in their FNPF models using surface-piercing numerical wavemakers. Brorsen and Larsen[4] proposed a different approach for generating waves using internal sources, which was also used by Grilli and Svendsen[43] and Ohyama and Nadaoka[66] in their models.

When using a wavemaker to generate waves, there is a corner in the model, at the intersection between the wavemaker and the free surface, separating boundary segments with both different boundary conditions and normal directions. Possible singularity of the flow near such an intersection has given rise to substantial concern in the literature. Grilli and Svendsen[46] reviewed such singularity problems and showed that, in the particular context of wavemakers starting from a state of rest ("cold start"), provided the initial acceleration of the wavemaker is small with respect to gravity and corner boundary conditions are well-posed in the model, numerically speaking, there will be no strong singularity at the free surface corner (at least in the FNPF regime). Thus, in the applications, they used an initial damping function for the wavemaker motion in such a way that the acceleration remain small during the first few time steps of the computations. They also ensured well-posedness of governing equations and boundary conditions on both sides of corners using a double-node representation combined with (continuity and compatibility) conditions expressing that potential and velocity are unique at corners (see Grilli and Svendsen[46] for more details). Many validations of Grilli and Svendsen's model were conducted for numerical piston or flap type wavemakers, particularly with solitary waves (e.g., Grilli *et al.*[33,34,36,41,45,46,47]). Extensions of compatibility relationships that further improve numerical accuracy at corners were proposed by Otta *et al.*[70] and Svendsen *et al.*[88], and their application and validation for the wavemaking problem was further discussed by Grilli and Subramanya[39].

Assuming "numerically well-posed" wavemaker boundary conditions, it is well known, however, that a clean finite amplitude wave cannot be generated using solid wavemakers, whether in laboratory tanks or in nonlinear wave models (see, e.g., Mei[63] p. 578). Essen-

tially, due to wave nonlinearity, higher-order harmonics are being generated that modulate the shape of the wave one intends to generate. This is because sinusoidal waves or other first-order solutions like Boussinesq solitary waves are not exact solutions of the fully nonlinear problem. To overcome this difficulty and generate "clean" finite amplitude waves in their model, Grilli and Svendsen[46] used the numerically exact method by Tanaka[90] to generate solitary waves, and Klopman[56], Subramanya and Grilli[85], and Grilli and Horrillo[31] used the exact periodic wave solution of the FNPF problem (i.e., a *streamfunction wave* (SFW) solution; Dean and Dalrymple[17] p. 305) to generate periodic waves [f].

In the present model, waves are thus generated either by prescribing a wavemaker motion on the "open sea" boundary $\Gamma_{r1}(t)$ of the computational domain, either by prescribing the elevation and potential on the free surface of a known "exact" wave solution of flow equations, or by using an internal line of sources.

General boundary conditions for these three types of wave generation are given in the following. Generation of specific waves is discussed in Section 3.

2.2.1. Plane wavemaker

A plane wavemaker motion $\overline{x} = x_p(z,t)$ can be specified on the moving boundary $\Gamma_{r1}(t)$ to generate waves as in laboratory experiments. In this case, normal velocity is specified over the surface of the paddle as,

$$\overline{\frac{\partial \phi}{\partial n}} = \mathbf{u}_p \cdot \mathbf{n} = \frac{\frac{\partial x_p}{\partial t}}{\sqrt{1+(\frac{\partial x_p}{\partial z})^2}} \qquad \text{on } \Gamma_{r1}(t) \tag{6}$$

in which the right hand side represents the normal paddle velocity. Eq. (6) is developed in Section 3 for the case of piston or flap wavemakers.

2.2.2. Exact wave solutions

"Numerically exact" permanent form solutions of the FNPF boundary value problem over constant depth (eqs. (1)-(5); i.e., solitary or streamfunction waves) can be generated either by specifying their potential $\phi(x,t_o)$ and elevation $\eta(x,t_o)$ on the free surface $\Gamma_f(t_o)$ at initial time t_o (solitary waves), or by specifying their horizontal velocity and acceleration $(u(z), \partial u/\partial t)$ along a vertical wavemaker boundary (streamfunction waves).

For *exact solitary waves*, normal velocity is also prescribed to $U(t)$ over the fixed vertical lateral boundaries Γ_{r1}, Γ_{r2}. We thus get,

$$\overline{\phi} = \phi(x,t_o)\ ,\ \overline{z} = \eta(x,t_o) \qquad \text{on } \Gamma_f(t_o)$$

$$\overline{\frac{\partial \phi}{\partial n}} = U(t) \qquad \text{on } \Gamma_{r1},\ \Gamma_{r2} \tag{7}$$

in which overbars denote prescribed values.

[f] Note that SFW's were also used in periodic FNPF models by Skourup *et al.*[80] and Grilli *et al.*[36].

Streamfunction waves, unlike linear periodic waves, have a non-zero horizontal mass flux. When specified at one extremity of the model, such waves thus lead to a continuous accumulation of water in the computational domain. In Klopman's[56] computations, only steep slopes were modeled in fairly short computational domains and waves were computed over a few periods only. Hence, water accumulation was small and did not cause any apparent problem. In Subramanya and Grilli's[85] shoaling computations, however, with a longer computational domain and for a larger number of wave periods, water accumulation resulted in a significant increase in the mean water level that clearly affected wave shape. For the corresponding coastal problem, one would expect an offshore return flow to occur under wave troughs (undertow) and cancel the incoming wave mass flux at some distance from the shore, thereby ensuring constant water volume in the nearshore region. Hence, water accumulation in the computational domain is non-physical and should be prevented. Grilli and Horrillo[31] 1995 proposed a method for achieving zero-average-mass flux in a SFW generation which they implemented and tested in their model. In this method, a depth uniform current, equal and opposite to the wave mean mass transport velocity is superimposed to the SFW [g].

For generating SFW's, a vertical wavemaker boundary is horizontally moved at one extremity of the model, following the motion, $x_p(t) = x_1(t)$, of the first node on the free surface, and wave kinematics is specified along the vertical boundary according to the SFW solution. Wave phase at time t is thus calculated along the wavemaker as,

$$\theta(t) = k\,(x_p(t) \;-\; c\,t) \;-\; \theta_o \tag{8}$$

where θ_o is an initial shift to the location of "zero-up-crossing " towards the wave crest, for which both wave elevation and horizontal velocity are zero. To avoid problems due to the "cold start" of the wave generation, the SFW velocity field is multiplied by a ("tanh-like") damping function $\mathcal{D}(t)$ smoothly varying between 0 to 1 over a specified number of wave periods. Boundary conditions on the wavemaker boundary thus read,

$$\begin{aligned} \overline{\frac{\partial \phi}{\partial n}} &= -u(\theta, z)\,\mathcal{D}(t) \qquad \text{on } \Gamma_{r1}(t) \equiv \{x = x_p(t); z \in [-h_o, \eta(x_p(t))]\} \\ \overline{\frac{\partial^2 \phi}{\partial t \partial n}} &= -u(\theta, z)\,\dot{\mathcal{D}}(t) \;-\; \frac{\partial u}{\partial t}(\theta, z)\,\mathcal{D}(t) \end{aligned} \tag{9}$$

where u and $\partial u/\partial t$ are calculated using both the coefficients and the wave characteristics obtained from Dean's[17] streamfunction solution [h].

2.2.3. Internal sources

[g] Note that since a current affects wave characteristics due to Doppler effects, SFW's have to be calculated by iteration so as to satisfy the zero-mass-flux condition as well as the streamfunction wave equations (see details in Ref.[31]).

[h] Acceleration terms have been mentioned in Eq. (9) since they will be needed in the model, as described below in Section 2.4.

The traditional way of generating waves by specifying a velocity distribution or the motion along part of the boundary has the disadvantage that this boundary also reflects waves propagating towards the boundary, from inside the computational domain (such as the scattered wave field from a structure). This is a major problem in any physical model. In a computational model, this can be avoided to a large degree by generating waves by internal sources (an idea first suggested by Brorsen and Larsen [4], for a linear wave model). If oscillating sources are distributed along a vertical, say, line placed a short distance inside the fluid domain, waves will be generated and will propagate away from the sources in both directions. The waves moving into the computational domain are the ones we are interested in. On the other hand waves scattered from structures inside the computational domain will essentially pass through the sourceline. Those scattered waves, along with waves generated away from the domain, should be leaving the domain through its open sea boundary. Hence, a radiation condition or an absorbing beach should also be specified with this type of wave generation (see, Grilli and Svendsen[43], Otta *et al.* [70], Ohyama and Nadaoka[66], and Grilli and Horrillo[31], for detail).

When sources (or sinks which are negative sources) are introduced in the fluid domain, Laplace's equation (1) becomes the Poisson equation,

$$\nabla^2\phi = b(\mathbf{x},t) \qquad \text{in } \Omega(t) \tag{10}$$

where $b(\mathbf{x},t)$ is the density of a known distribution of sources inside the domain $\Omega(t)$. Values of $b(\mathbf{x},t)$ are discussed in Section 3 for the generation of specific waves in the model.

2.3. Boundary condition for wave absorption

Energy absorption may be necessary in a FNPF model to calculate shoaling of a train of waves for sufficiently long time over a slope, whether these waves break and/or runup on the slope. As discussed above, absorption may also be necessary for the generation of waves by an internal line of sources.

Within the frame of potential flow theory, no purely dissipative process can be used to absorb the energy of incident waves. To overcome this difficulty, two main approaches were proposed in the literature mostly for the absorption of linear waves or weakly nonlinear long waves : (i) wave radiation through an open boundary (e.g., Engquist and Majda[22], Israeli and Orszag[52], Orlanski[68], Sommerfeld[83]); and/or (ii) wave damping directly on the free surface or within a so-called "sponge layer" (e.g., LeMehaute[59], Larsen and Dancy[58]). No general method has yet been proposed for the absorption/radiation of fully nonlinear transient waves. Instead, some rather heuristic boundary conditions were proposed.

Along the line (i), Lin *et al.*[60] matched exterior linear solutions to the nonlinear interior solution at finite distance. Dommermuth and Yue[19] used the same method as Lin *et al.*'s to compute the forced heaving motion of an axisymmetric cylinder. Some of the radiation conditions developed for linear waves are also applicable to fully nonlinear waves of permanent form like solitary or streamfunction waves. Grilli *et al.*[36], for instance, developed an implicit iterative radiation condition based on Sommerfeld's[83] condition. A more accurate explicit approach was proposed by Otta *et al.*[70] who combined Orlanski's[68]

radiation condition with the incident wave field kinematics calculated at internal nodes in the model, close to the radiation boundary. The method worked well for periodic waves but only showed limited success when applied to irregular waves.

Along the line (ii), Larsen and Dancy[58] developed a sponge layer method based on the idea of an "absorbing beach" (AB), first suggested by LeMehaute[59]. They only implemented the method in a (weakly nonlinear) Boussinesq model but their method was later used by Ohyama and Nadaoka[66] in a FNPF model. Similar methods were successfully used by Baker *et al.*[5] and Cointe[10] in their FNPF models, and by Subramanya and Grilli[85] and Grilli and Horrillo[31], who implemented an AB with active control of the beach parameter in their FNPF model. Boundary conditions for the latter AB are briefly presented in the following. In this case, the AB is always located at the top of a slope but the same principle can be (and has been) used to generate waves at an open ocean boundary in combination with a distribution of internal sources (Ohyama and Nadaoka[66]) or to simulate bottom discontinuities—like shelf-breaks or reefs—inducing local energy loss in incident waves.

The principle of the AB is similar to the ideas developed in Refs.[5,10] : a negative work is created against incident waves over a given section of the free surface by specifying an external counteracting pressure, $p_a = P$, in the dynamic free surface condition (3) (with $z = \eta$), which effectively extracts energy from the incident wave train. For shoaling problems, the AB is located in the model over a shallow shelf region of maximum depth h_1 in the upper part of the slope (Fig. 2). In most earlier approaches, P was specified proportional to the free surface potential ϕ but this could result in creating a positive work in the AB in some cases and, hence, lead to increased wave energy in the beach. In order for the AB to always produce a negative work against the wave motion and thus to always remove energy from the wave train, as suggested by Cao *et al.*[9], the external pressure is defined here as proportional to the normal particle velocity, $\partial\phi/\partial n$, along the free surface. The modified dynamic free surface condition thus reads,

$$\frac{D\phi}{Dt} - \frac{1}{2}\boldsymbol{\nabla}\phi \cdot \boldsymbol{\nabla}\phi + g\eta + \frac{P}{\rho} = 0 \tag{11}$$

with,

$$P(x,\eta,t) = \nu(x,t)\frac{\partial\phi}{\partial n}(\eta(x,t)) \tag{12}$$

in which ν, the beach absorption function, varies smoothly along the AB as,

$$\nu(x,t) = \nu_o(t)\,\rho\sqrt{gh_1}\,(\frac{x-x_l}{l})^{\alpha} \tag{13}$$

where $\alpha = 2$ to 3 and ν_o is a non-dimensional beach absorption coefficient. In earlier approaches, ν_o was specified as constant (e.g., Refs.[5,9,10]). To optimize absorption of incident wave energy in the AB and make it easier, at a later stage, to deal with irregular waves, Grilli and Horrillo[31] adaptively calculated ν_o in the model as a function of time (i.e., for each time step in the model) for the AB to exactly absorb the period-averaged wave energy entering the beach over time step Δt. Details and validation of adaptive energy absorption in the AB can be found in Ref.[31].

2.4. The time integration

Free surface boundary conditions (2) and (3) are integrated at time t, to establish both the new position and the relevant boundary conditions on the free surface, at a subsequent time $t + \Delta t$ (with Δt being a small time step). In the model, this is done following the approach introduced by Dold and Peregrine [18], using Taylor expansions for both the position $\mathbf{r}(t)$ and the potential $\phi(\mathbf{r}(t))$ on $\Gamma_f(t)$. Series, truncated to Nth-order, are expressed in terms of the material derivative (4) and of time step Δt, as,

$$\overline{\mathbf{r}}(t+\Delta t) = \mathbf{r}(t) + \sum_{k=1}^{N} \frac{(\Delta t)^k}{k!} \frac{D^k \mathbf{r}(t)}{Dt^k} + \mathcal{O}[(\Delta t)^{N+1}] \tag{14}$$

for the free surface position, and,

$$\overline{\phi}(\mathbf{r}(t+\Delta t)) = \phi(\mathbf{r}(t)) + \sum_{k=1}^{N} \frac{(\Delta t)^k}{k!} \frac{D^k \phi(\mathbf{r}(t))}{Dt^k} + \mathcal{O}[(\Delta t)^{N+1}] \tag{15}$$

for the potential. The last terms in Eqs. (14) and (15) represent truncation errors. The time updating of the free surface geometry described by Eq. (14) actually corresponds to following the motion of fluid particles in time. This procedure is often referred to as a "Mixed Eulerian-Lagrangian" formulation.

Second-order series are used in the present case (N=2). Higher-order Taylor series, however, have successfully been used by others to provide highly accurate solutions for periodic problems (e.g., Dold and Peregrine [18] (N=3), and Seo and Dalrymple [77] 1990 (N=4)).

First-order coefficients in Eqs. (14) and (15) are obtained, based on Eqs. (2) and (3), using ϕ and $\frac{\partial \phi}{\partial n}$ as provided by the solution of Laplace's equation (1) at time t. Second-order coefficients are expressed as $\frac{D}{D\,t}$ of (2) and (3), and are calculated using the solution of a second elliptic problem of the form (1) for ($\frac{\partial \phi}{\partial t}$, $\frac{\partial^2 \phi}{\partial t \partial n}$). This is because all time derivatives of the potential satisfy Laplace's equation. Higher-order series would simply require that more Laplace's equations are solved for higher-order time derivatives of ϕ. Detailed expressions of the coefficients of Taylor series (14) and (15) are given in Appendix A, in a curvilinear coordinate system $(\mathbf{s}, \mathbf{n})$ defined along the boundary (Fig. 3).

No-flow boundary conditions for a second Laplace's equation for $\frac{\partial \phi}{\partial t}$ are readily obtained along solid boundaries, as,

$$\overline{\frac{\partial^2 \phi}{\partial t \partial n}} = 0 \qquad \text{on } \Gamma_b \text{ and } \Gamma_{r2} \tag{16}$$

The boundary condition at the free surface is obtained from Eqs. (3) and (4) as,

$$\overline{\frac{\partial \phi}{\partial t}} = -\frac{1}{2} \boldsymbol{\nabla}\phi \cdot \boldsymbol{\nabla}\phi - \frac{p_a}{\rho} - gz \qquad \text{on } \Gamma_f(t) \tag{17}$$

which indicates that $\overline{\frac{\partial \phi}{\partial t}}$ can be specified on the free surface as a function of known geometry and potential at time t.

When $\Gamma_{r1}(t)$ represents a wavemaker boundary moving at velocity $\mathbf{u}_p(\mathbf{x}_p(t),t)$, we have by (6),

$$\overline{\frac{\partial^2\phi}{\partial t\partial n}} = \frac{\partial}{\partial t}(\mathbf{u}_p\cdot\mathbf{n})$$

or,

$$\overline{\frac{\partial^2\phi}{\partial t\partial n}} = [\frac{d\,(\mathbf{u}_p\cdot\mathbf{n})}{d\,t} - \mathbf{u}_p\cdot\boldsymbol{\nabla}(\mathbf{u}_p\cdot\mathbf{n})] \qquad \text{on } \Gamma_{r1}(t) \tag{18}$$

in which, $\frac{d}{d\,t} = \frac{\partial}{\partial t} + \mathbf{u}_p\cdot\boldsymbol{\nabla}$, denotes time derivative following the motion of the boundary $\mathbf{x}_p(t)$. This boundary condition is further developed in Section 3.

When waves are generated by a line of internal sources, the time derivative of the source strength $\frac{\partial b}{\partial t}(\mathbf{x},t)$ is introduced in a Poisson equation of the form (10), for $\frac{\partial\phi}{\partial t}$.

2.5. Discussion of model assumptions and limitations

No approximations other than potential flow theory have been made in the model. In particular, unlike analytical or numerical expansion wave theories (see, Dean and Dalrymple [17]), no small parameter, periodicity, or permanent form wave conditions, have been assumed. This makes the present model valid from deep to shallow water and for arbitrary length waves.

The main limitations—inherent to potential flow theory—of this type of model are that bottom friction and flow separation cannot be modeled, and that computations have to be interrupted shortly after breaking of a wave first occurs. These limitations are discussed in the following :

- Long wave theory shows that bottom friction should attenuate long waves in shallow water, whereas short waves should be relatively unaffected.
  For solitary waves shoaling over gentle bottom slopes, however, experiments by Camfield and Street [6] showed that "bottom roughness has no measurable effect". This was later confirmed in other experiments by Grilli *et al.* [41] (see Fig. 14 and applications in Section 5.4). The likely reason for this is that bottom friction only becomes significant when wave height is large and this only occurs in a small region over the slope, just before the wave starts breaking.
  For large solitary waves running up a steep slope, Grilli and Svendsen[44,45,47] and Svendsen and Grilli [87] compared their nonlinear computations to experiments and found that frictional effects were also negligible. In this case, the distance of propagation over steep slopes was likely too small for friction to significantly affect waves, despite their large amplitude.
  Hence, bottom friction is not an important factor when wave height and/or distance of propagation are small.
- Flow separation over obstacles on the bottom is significant for steep obstacles (like steps or rectangular bars) of large height to depth ratios, and for high waves (Grilli *et al.* [32,33] 1992; see Figs. 5-8 in Section 5.2).

Flow separation leads to an energy loss at the obstacle that reduces wave height downstream of the obstacle. As mentioned before, although not yet tested in the model, localized energy loss could be specified to model dissipation at steps and obstacles on the bottom based on the energy absorption method used by Grilli and Horrillo[31] for their absorbing beach.

- When a wave starts overturning, a small horizontal jet forms in the highest region of the wave crest (Figs. 1 and 4). The jet curls up on itself and falls towards the free surface. Breaking occurs when the tip of the falling jet impinges on the free surface, leading to a local violation of continuity equation manifesting itself by strongly unstable numerical results. Hence, computations with the model are in essence limited to prior to the time such an impact of a wave on the free surface first occurs. Because of potential flow theory hypotheses, however, computationally accurate results may not be physically realistic up to that stage. This is discussed below.

  Dommermuth *et al.* [20] compared wave profiles calculated using a FNPF model to experimental results for deep water overturning breakers. They concluded that potential theory is valid up to the moment the tip of the breaker jet hits the free surface (i.e., slightly further in time than in the situation illustrated in Fig. 1).

  Skyner *et al.* [81] confirmed this conclusion and compared computed and measured velocities inside plunging breakers. The good agreement they found for the velocities further confirmed the validity of potential flow theory.
- For a train of solitary or periodic waves shoaling over a sloping beach, the front wave of the train is also the steepest wave that first breaks in the shallower water. Hence, the model can be used to calculate detailed shoaling coefficients over the length of the beach, up to the point the front wave breaks (breaker line). In this case, computations are not greatly affected by the limitation of the model to the first breaking wave, discussed above.

  For periodic waves, computations can be pursued for a longer time by using an absorbing beach in the upper slope region of the model (Subramanya and Grilli[85], Grilli and Horrillo[31]). Doing so, waves can shoal the slope up to a very large fraction of their breaking height and then be absorbed in the beach. A quasi-steady state can thus be reached in the model for which characteristics of fully nonlinear waves shoaling over a slope (or more complex bottom geometry) can be calculated.

  For irregular wave trains and/or complex bottom geometry, breaking is likely to occur almost anywhere in the shoaling region, due to nonlinear interactions between wave components and between waves and bottom geometry. Hence, computations may have to be stopped when breaking first occurs, and this limitation may reduce the utility of the model in its present form for addressing these situations.
- Finally, runup of non-breaking waves on steep or gentle slope can be accurately calculated in a FNPF model (e.g., Grilli *et al.*[41], Grilli and Svendsen[44,45,47], Svendsen and Grilli[87]), again, provided wave reflection does not make another incoming wave break, or a thin jet of water is not expelled at runup (like, e.g., in the computations with a vertical wall in Cooker[12], Cooker and Peregrine[14], and Grilli *et al.*[33,35]), or breaking does not occur during the backwash (like in Grilli and Svendsen[47], Svendsen

and Grilli[87], Otta *et al.*[69]).

3. Wave generation in the model

3.1. Exact solitary waves

Tanaka [90] proposed a method to calculate numerically exact solitary wave solutions of the FNPF problem in constant depth h_o. This method has been implemented in the model to specify initial *exact* solitary waves for which surface elevation and potential are directly prescribed on the free surface [i], using (7).

In the applications with solitary waves, standard dimensionless variables, x', z', t' and c', will be used with definitions,

$$x' = \frac{x}{h_o}\ ,\ z' = \frac{z}{h_o}\ ,\ t' = t\sqrt{\frac{g}{h_o}}\ ,\ c' = \frac{c}{\sqrt{g h_o}} = \ F \tag{19}$$

in which c denotes wave celerity and F is the wave Froude number. For solitary waves, initial wave height H_o is identical to the maximum elevation above $z = 0$, and we further denote by, $H' = H/h_o$, the nondimensional wave height. Details of Tanaka's method are given in Appendix B.

3.2. Exact periodic waves

The streamfunction wave (SFW) theory was introduced by Dean[16] (see also Dean and Dalrymple[17]) to calculate numerically exact periodic solutions of the FNPF problem in constant depth h_o. The original method worked in a coordinate system moving with the wave celerity, $c = L/T$ (with L the wavelength and T the wave period), and accounted for the presence of a depth-uniform current U.

A streamfunction wave solution is thus defined as,

$$\psi(\theta, z) = \sum_{j=1}^{N} X(j)\ \sinh j k(h_o + z)\ \cos j\theta\ - (U - c)z \tag{20}$$

where, $\theta = k(x - c\,t)$, is the wave phase and $X(j)$ is a set of N coefficients that are numerically calculated, along with $L = 2\pi/k$, to satisfy free surface boundary conditions (2) and (3), and specified wave height and period (H, T).

Horizontal velocity is easily obtained from Eq. (20) in the original coordinate system as a function of depth as,

$$u(\theta, z) = -\frac{\partial \psi}{\partial z}\ +\ c\ =\ -\sum_{j=1}^{N} (j\,k)\ X(j)\ \cosh j k(h_o + z)\ \cos j\theta\ +\ U \tag{21}$$

[i] In applications, initial *exact* solitary waves are specified far enough from lateral boundaries of the model for $U(t) \simeq 0$ to be assumed with sufficient accuracy.

Noting that, $\partial\theta/\partial t = -c\,k$, local horizontal acceleration is obtained as,

$$\frac{\partial u}{\partial t}(\theta, z) = -c \sum_{j=1}^{N} (j\,k)^2 \; X(j) \; \cosh j\,k(h_o + z) \; \sin j\theta \tag{22}$$

Equations (21) and (22) are used to specify the kinematics of an incident SFW over a vertical wavemaker boundary located at, $x = x_p$, in the model (Eq. (9)).

Following the method by Grilli and Horrillo[31], current U can be specified as opposite to the direction of wave propagation, with a magnitude such as to generate zero-mass-flux SFW's in the model.

3.3. Wave generation by a plane wavemaker

3.3.1. Introduction

An oscillating paddle wavemaker can be specified on boundary $\Gamma_{r1}(t)$ to generate waves the same way as in laboratory wave tanks. The wavemaker motion $\mathbf{x}_p(t)$ and velocity $\mathbf{u}_p(\mathbf{x}_p(t), t)$ required to generate specific incident waves can be obtained from first-order wave theory (i.e., Boussinesq theory for long waves and first-order Stokes theory for periodic short waves) [j].

Waves generated with a first-order method propagate without change of form only in a model solving first-order theory equations. In the present fully nonlinear model—or for this respect in a laboratory wavetank—such waves are not expected to correspond to permanent form solutions (for this matter, a SFW solution would be needed). Goring [25], for instance, found that solitary waves of small amplitude ($H' < 0.2$) generated by a piston wavemaker in a wave flume kept their shape constant within a very small margin. For such small waves, the first-order wave profile is quite close to an *exact* solitary wave. For steeper waves ($H' \geq 0.2$), however, Goring found that solitary waves shed a tail of oscillations behind them as they propagated down the flume. Similarly, in computations with their model, Grilli and Svendsen [47] observed that waves of significantly large height generated by a wavemaker adjusted their shape as they propagated down a numerical tank. Such results were reproduced in many different numerical set-ups and found to agree quite well with corresponding laboratory experiments (Grilli and Svendsen [47], Grilli *et al.* [32,33,34,41], Svendsen and Grilli [87]).

3.3.2. General wavemaker boundary condition

General boundary conditions for $\frac{\partial \phi}{\partial n}$ and $\frac{\partial^2 \phi}{\partial t \partial n}$ can be derived for any specified wavemaker motion and velocity, based on Eqs. (6) and (18). The latter equation for $\frac{\partial^2 \phi}{\partial t \partial n}$ includes a time derivative with respect to the rigid body motion that needs to be carefully derived.

[j] Note that second-order corrections can also be applied to wavemaker motion in the model as done in laboratory flumes (e.g., Skourup[79] 1995).

This was done by Cointe [11] for the motion of a rigid body of arbitrary shape. In the case of a plane rigid body like a wavemaker, Cointe's expression reads,

$$\overline{\frac{\partial^2\phi}{\partial t\partial n}} = (\ddot{\boldsymbol{\alpha}}\cdot\mathbf{n}) + \dot{\theta}\,[(\dot{\boldsymbol{\alpha}}\cdot\mathbf{s}) - \frac{\partial\phi}{\partial s}\,] - \frac{\partial^2\phi}{\partial n\partial s}(\dot{\boldsymbol{\alpha}}\cdot\mathbf{s}) + \frac{\partial^2\phi}{\partial s^2}(\dot{\boldsymbol{\alpha}}\cdot\mathbf{n}) \tag{23}$$

in which $\boldsymbol{\alpha}$ denotes the position vector for points on the wavemaker surface, θ is the angle of rotation around point $\mathbf{x}_g$, and dots denote absolute time derivatives with respect to the body motion, $d/d\,t$, defined as in Eq. (18).

Expressions for the velocity and the acceleration of boundary points $(\dot{\boldsymbol{\alpha}}, \ddot{\boldsymbol{\alpha}})$ can be derived for various types of wavemakers as a function of wavemaker stroke x_p and used in Eq. (23) to specify boundary conditions in the model. This is done in Appendix C for both piston and flap type wavemakers.

In the next two sections, expressions of wavemaker stroke used for generating first-order waves in the model are discussed.

3.3.3. Generation of long waves by a piston wavemaker

In a long wave of permanent form over constant depth h_o, due to mass conservation, we have at any instant,

$$\int_{-h_o}^{\eta} u\ \mathrm{d}z = c_a\eta + Q_s + u_c h_o \tag{24}$$

in which c_a is the propagation speed of the wave in a fixed frame of reference, $\eta(x,t)$ is the wave elevation above still water level, Q_s is the nonlinear mass flux averaged over a wave period, and u_c is the speed of the current defined as the averaged particle velocity below wave trough level.

For a first-order long wave, the right hand side of Eq. (24) simply reduces to $c\eta$, where c is the speed of the wave relative to the water, so that Eq. (24) becomes the simpler expression used, e.g. by Goring [25], for determining the motion required by a piston wavemaker to generate a specified water surface elevation immediately in front of the wavemaker. Since the piston motion creates a depth uniform horizontal velocity $u_p(x_p(t),t)$, Eq. (24) reduces to,

$$u_p(t) = \frac{c\eta}{h_o+\eta} \tag{25}$$

which means that a surface elevation η can be generated by specifying the piston velocity u_p as defined above. In this case, horizontal piston motion $x_p(t)$ is given by,

$$x_p(t) = \int_0^t \frac{c\,\eta(x,\tau)}{h_o+\eta(x,\tau)}\ \mathrm{d}\tau \tag{26}$$

Developments of this equation for generating first-order solitary or cnoidal waves are given in Appendix D.

As mentioned before, this method will only generate accurate permanent form long waves for sufficiently small initial wave height (i.e., smaller than $\simeq 0.2h_o$). This is illustrated in the applications in Section 5.

3.3.4. Generation of a sum of periodic sine waves by a flap wavemaker

As commonly done in laboratory experiments, a sum of sine waves can be generated in the model using a flap wavemaker in water of depth h_o and specifying boundary conditions based on *first-order* Stokes theory.

To do so, the paddle stroke $x_p(t)$ is specified as the sum $\mathcal{S}(t)$ of n sine functions of frequency $2\pi\omega_i$, phase φ_i, and amplitudes A_i. The latter are related (in a linear sense) to corresponding wave component amplitudes a_i to be generated, by a linear transfer function, $\mathcal{T}(\omega_i, h_o)$, which can be obtained from wavemaker theory (e.g., Dean and Dalrymple [17]). Furthermore, a smooth start of the wavemaker, with small initial acceleration, is ensured by multiplying $x_p(t)$ by a damping function $\mathcal{D}(t)$ varying from 0 to $(1-\varepsilon_z)$ over a given time $2\,t_{\varepsilon_z}$. For $\varepsilon_z \ll 1$, the damping function gives a smooth transition from 0 to $\sim \mathcal{S}(t)$ over a time $2\,t_{\varepsilon_z}$.

We thus get,

$$x_p(t) = \mathcal{S}(t)\mathcal{D}(t) \qquad \text{with} \qquad \mathcal{S}(t) = \sum_{i=1}^{n} A_i\,[1-\cos(\omega_i\,t+\varphi_i)]/2$$

$$a_i = A_i\,\mathcal{T}(\omega_i, h_o) \qquad \text{with} \qquad \mathcal{T}(k_i(\omega_i, h_o), h_o) = \frac{4\sinh^2 k_i h_o}{2k_i d + \sinh 2k_i h_o} \tag{27}$$

with, $H_i = 2a_i$, the wave height (predicted by linear wave theory) and $k_i(\omega_i, h_o)$, the wavenumber of a given sine wave component to be generated obtained using the linear dispersion relation as,

$$k_i \tanh k_i h_o = \frac{\omega_i^2}{g} \tag{28}$$

Detailed expressions for $\mathcal{D}(t)$ and resulting wavemaker boundary conditions are given in Appendix E.

As discussed before, due to nonlinearities, it is well known that free second and higher-order harmonics will be created when monochromatic waves of finite amplitude propagate down a tank (see, e.g., Mei [63]). This is illustrated in the applications in Section 5.

3.4. Wave generation by an internal line of sources

Using a BIE representation based on free space Green's function, Poisson equation (10) transforms into (see Section 4.2),

$$\begin{aligned}\alpha(\mathbf{x}_l)\phi(\mathbf{x}_l) &= \int_{\Gamma(\mathbf{x})} [\frac{\partial\phi}{\partial n}(\mathbf{x})G(\mathbf{x},\mathbf{x}_l) - \phi(\mathbf{x})\frac{\partial G(\mathbf{x},\mathbf{x}_l)}{\partial n}]\,d\Gamma(\mathbf{x}) \\ &+ \int_{\Omega(\mathbf{x})} b(\mathbf{x},t)G(\mathbf{x},\mathbf{x}_l)\,d\Omega(\mathbf{x})\end{aligned} \tag{29}$$

where $b(\mathbf{x},t)$ denotes the source field contribution. Eq. (29) can be solved by a Boundary Element Method (BEM) (see Section 4.3.) but, in the present case, besides boundary integrals, domain integrals must be calculated to account for the source field contribution.

For a vertical line of sources with linear density $q(s(\mathbf{x}),t)$ (with $s(\mathbf{x})$ measured along the line Γ_ℓ), the source contribution in Eq. (29) reduces to,

$$\int_\Omega b(\mathbf{x},t)G(\mathbf{x},\mathbf{x}_l)\,d\Omega = \int_{\Gamma_\ell} q(s(\mathbf{x}),t)G(\mathbf{x},\mathbf{x}_l)\,d\Gamma_\ell \tag{30}$$

In two dimensions, a line of sources with continuously varying strength creates a velocity normal to the line equal to $q/2$. Thus, specification of the strength of the source distribution q is straightforward if particle velocities are known along the line for the waves to be generated. In most cases, it is sufficient to specify the source strength only at N_s points along the line Γ_ℓ. In this case, only point sources of strength $B_s(t)$ are specified along a vertical line from bottom to surface at say, $x = x_s$, thus defining N_s segments of constant strength,

$$B_s(t) = 2\,\frac{\eta(x_s,t)+h_o}{N_s}\,\overline{u_w}(x_s,z_s,t) \qquad ;s = 1,\ldots,N_s \tag{31}$$

where $\overline{u_w}(x_s,z_s,t)$ denotes the mean horizontal velocity of the wave within the s-th segment and $\eta = \eta(x_s,t)$ is the wave elevation above the source line (a stretching is applied to the line to account for changes in wave elevation above the line). Hence, in Eq. (30), we have,

$$q(s(\mathbf{x}),t) = \sum_{s=1}^{N_s} B_s(t)\delta(\mathbf{x}-\mathbf{x_s}) \qquad ;s = 1,\ldots,N_s \tag{32}$$

where $\delta(\mathbf{x}-\mathbf{x_s})$ denotes a Dirac function at point $\mathbf{x_s}$ and, due to the sifting property of the Dirac function, Eq. (30) simplifies into,

$$\int_\Omega b(\mathbf{x},t)G(\mathbf{x},\mathbf{x}_l)\,d\Omega = \sum_{s=1}^{N_s} B_s(t)G(\mathbf{x}_s,\mathbf{x}_l) \tag{33}$$

This method of wave generation makes it possible to model any wave motion for which particle velocity distribution is given along a chosen bottom-to-surface line. Two such cases are detailed in Appendix F.

4. Numerical Model

4.1. Time stepping method

If initial conditions are known at time t on the free surface boundary $\Gamma_f(t)$, i.e., the position $\mathbf{r}(t)$ and the potential $\phi(t)$, together with relevant boundary conditions on the rest of the boundary, one can calculate $\frac{\partial\phi}{\partial n}$ and the time derivatives $\frac{\partial\phi}{\partial t}$ and $\frac{\partial^2\phi}{\partial t\partial n}$ along $\Gamma_f(t)$ by solving two Laplace's equations of the type (1) for ϕ and $\frac{\partial\phi}{\partial t}$, expressed in the same geometry [k]. At this stage, both the free surface position and potential can be updated to subsequent time, $t+\Delta t$, using Taylor series expansions (14) and (15), truncated to second-order in Δt ($N = 2$). Lateral boundary conditions (e.g., wavemakers) are then updated, if needed, to

[k] This is done in the model using a Boundary Element Method (BEM), as detailed in the following Sections.

complete a full time stepping loop. The whole process is repeated to carry computations further in time.

Coefficients in the Taylor series are expressed as function of $\{\phi, \frac{\partial\phi}{\partial n}, \frac{\partial\phi}{\partial s}, \frac{\partial^2\phi}{\partial n\partial s}, \frac{\partial^2\phi}{\partial s^2}, \frac{\partial\phi}{\partial t}, \frac{\partial^2\phi}{\partial t\partial n}, \frac{\partial^2\phi}{\partial t\partial s}, \beta, \frac{\partial\beta}{\partial s}, p_a, \frac{D\,p_a}{D\,t}\}$ along the free surface, using equations (A.7), (A.14), (A.15) and (A.21) developed in Appendix A, with $\mathbf{s}$ and $\mathbf{n}$ given by (A.1),(A.2) as a function of β, the angle between $\mathbf{s}$ and the x-axis. Tangential s-derivatives of field variables that appear in some of these coefficients are computed within a 4th-order "sliding" polynomial on the boundary. At the intersection between the free surface and a moving wavemaker boundary, the accuracy of the s-derivatives is in general not sufficient and special relationships developed by Grilli and Svendsen [46] ("compatibility conditions") are used for calculating derivatives [l].

More specifically, for any given time t, values of $\frac{\partial\phi}{\partial n}$ and the geometry are specified along lateral boundaries depending on the specific problem under consideration [m]. These boundary conditions, together with the specification of ϕ on the free surface at time t, define a first Laplace problem which is solved to calculate ϕ or $\frac{\partial\phi}{\partial n}$ along Γ (whichever is unknown). Following this, $\frac{\partial\phi}{\partial t}$ is specified on the free surface using Bernoulli equation (17) as,

$$\overline{\frac{\partial\phi}{\partial t}} = -\frac{1}{2}[(\frac{\partial\phi}{\partial s})^2 + (\frac{\partial\phi}{\partial n})^2] - \frac{1}{\rho}p_a - gz(\mathbf{r}) \qquad \text{on } \Gamma_f(t) \tag{34}$$

in which all right hand side variables and the geometry are known at time t. Depending on the type of conditions along the rest of the boundary, $\frac{\partial^2\phi}{\partial t\partial n}$ is similarly specified and a second Laplace problem is solved to calculate $\frac{\partial\phi}{\partial t}$ or $\frac{\partial^2\phi}{\partial t\partial n}$ whichever is unknown [n]. At this stage, both the geometry and values of $\{\phi, \frac{\partial\phi}{\partial n}, \frac{\partial\phi}{\partial t}, \frac{\partial^2\phi}{\partial t\partial n}\}$ are known at time t along the boundary and the free surface updating to subsequent time $t + \Delta t$ can proceed as described above.

These operations are globally referred to as "time stepping" at time t, with time step value being Δt.

4.2. Transformation of Laplace's equations into BIE's

In the model, Laplace's equations for ϕ and $\frac{\partial\phi}{\partial t}$ are transformed into Boundary Integral Equations (BIE) using third Green's identity and free space Green's function G defined as,

$$\nabla^2 G(\mathbf{x}, \mathbf{x}_l) + \delta(\mathbf{x}, \mathbf{x}_l) = 0 \tag{35}$$

in which $\delta(\mathbf{x}, \mathbf{x}_l)$ is a Dirac function at point $\mathbf{x}_l$ of domain Ω. With definition (35), third

[l] These relationships were later extended by Otta *et al.*[70], Svendsen *et al.*[88], and Grilli and Subramanya[39], and the extended expressions are used in the applications of the model in Section 5.

[m] Boundary motion and $\frac{\partial\phi}{\partial n}$ can for instance be calculated using Eq. (C.5) for a piston wavemaker and $\frac{\partial\phi}{\partial n}$ is invariably zero along solid boundaries.

[n] Since both Laplace problems are expressed for the same boundary geometry $\Gamma(t)$, the additional computational effort required to solve the second problem is quite small.

Green's identity for the potential ϕ reads,

$$\phi(\mathbf{x}_l) \;=\; \int_{\Gamma(\mathbf{x})} [\, G(\mathbf{x},\mathbf{x}_l)\,\frac{\partial \phi}{\partial n}(\mathbf{x}) - \;\phi(\mathbf{x})\frac{\partial G}{\partial n}(\mathbf{x},\mathbf{x}_l)\,]\,d\Gamma(\mathbf{x}) \tag{36}$$

in which the "sifting" property of the Dirac function has been used to eliminate the domain integral. In two-dimensions, the solution of Eq. (35) yields (e.g., Brebbia [2])

$$G(\mathbf{x},\mathbf{x}_l) \;=\; -\frac{1}{2\pi}\log|\;\mathbf{x}-\mathbf{x}_l\;| \tag{37}$$

Thus, Green's function $G(\mathbf{x},\mathbf{x}_l)$, also referred to as *fundamental solution* of Laplace's equation, has a logarithmic singularity when point $\mathbf{x}$ approaches point $\mathbf{x}_l$.

A system of BIE's for values of $\phi(\mathbf{x}_l)$ is obtained by selecting a set of points $\mathbf{x}_l$ on the boundary. Doing so, some of the integrals in Eq. (36) become strongly singular and the "extraction" of such singularities (in a Cauchy Principal Value sense) creates so-called jumps in the potential value when moving from inside the domain to the boundary (e.g., Brebbia [2]). After some transformations, weakly singular BIE's corresponding to Laplace problems for ϕ and $\frac{\partial \phi}{\partial t}$ are derived as,

$$\begin{aligned}
\alpha(\mathbf{x}_l)\phi(\mathbf{x}_l) &= \int_{\Gamma(\mathbf{x})}[\frac{\partial \phi}{\partial n}(\mathbf{x})G(\mathbf{x},\mathbf{x}_l) - \phi(\mathbf{x})\frac{\partial G}{\partial n}(\mathbf{x},\mathbf{x}_l)]\,d\Gamma(\mathbf{x}) \\
\alpha(\mathbf{x}_l)(\mathbf{x}_l) &= \int_{\Gamma(\mathbf{x})}[\frac{\partial^2 \phi}{\partial t \partial n}(\mathbf{x})G(\mathbf{x},\mathbf{x}_l) - (\mathbf{x})\frac{\partial G}{\partial n}(\mathbf{x},\mathbf{x}_l)]\,d\Gamma(\mathbf{x})
\end{aligned} \tag{38}$$

in which $\mathbf{x} = (x,z)$ and $\mathbf{x}_l = (x_l, z_l)$ are points on boundary Γ and $\alpha(\mathbf{x}_l)$ is a geometric coefficient function of the angle of the boundary at point $\mathbf{x}_l$ which contains the jumps in potential value mentioned above.

Other integral equations approaches can be (and have been) proposed for solving potential flow equations in FNPF models. Cauchy Integral theorem can be used to derive BIE's for the complex velocity potential (e.g. Dold and Peregrine[18], Vinje and Brevig[92]). A vortex sheet method can also be used to derive BIE's for the vorticity density (Biot-Savart equations; Zaroodny and Greenberg[96] and Baker *et al.*[5]).

In all cases singular BIE's are obtained which are discretized into algebraic equations and numerically evaluated (see next Section).

4.3. Discretization and solution of Boundary Integral Equations

The numerical solution of the two BIE's (38) requires both the selection of *N collocation nodes* $\mathbf{x}_l$ along the entire boundary (discretization), to describe the variation of boundary geometry as well as boundary conditions and unknown functions of the problem, and *interpolation functions* to describe this variation in between the collocation nodes. In the present model, this is done using a Boundary Element method (BEM) (Brebbia [2]) in which the variation of all quantities is represented by means of shape functions or splines and the boundary is divided into M elements, each of which contains two or more nodes. In the applications in Section 5, quadratic isoparametric elements (Grilli, *et al.*[36]) are used on lateral and bottom boundaries, and cubic elements ensuring continuity of the boundary

slope are used on the free surface. In these elements, geometry is modeled by a cubic spline approximation and field variables are interpolated between each pair of nodes on the free surface either using linear shape functions (Quasi-spline elements (QS); Grilli and Svendsen[46]) or the mid-section of a four-node "sliding" isoparametric element (Mixed Cubic Interpolation (MCI); Grilli and Subramanya[39]).

Using a set of boundary elements, each boundary integral is transformed into a sum of M integrals over each element. Non-singular integrals are computed by a standard Gauss quadrature rule. A kernel transformation is applied to weakly singular integrals which are then integrated by a numerical quadrature which is exact for the logarithmic singularity (Grilli *et al.*[36]). Adaptive integration methods based on subdividing the integrals are used to improve the accuracy of regular integrations near corners and in other areas of the domain where elements on different parts of the boundary may get close to each other and create almost singular situations (Grilli and Subramanya[37]).

Corners are represented by double nodes and compatibility relationships are specified for boundary velocity components on each side of corners, to ensure both uniqueness and regularity of the solution (Grilli and Subramanya[39]; Grilli and Svendsen[46]). Double nodes represent two nodes of identical coordinates with different nodal values of the field variables. Hence, two algebraic BIE's are obtained for each double node, which, however, are not independent. Continuity conditions express uniqueness of ϕ or $\frac{\partial \phi}{\partial t}$ for both nodes of a double node and compatibility conditions express uniqueness of the velocity or the acceleration vectors, based on values of ($\frac{\partial \phi}{\partial s}$, $\frac{\partial \phi}{\partial n}$) or ($\frac{\partial^2 \phi}{\partial t \partial s}$, $\frac{\partial^2 \phi}{\partial t \partial n}$), respectively, on both intersecting boundaries at the corner.

Discretization and numerical integrations transform the BIE's into a system of N linear algebraic equations in which boundary conditions are directly specified. The system is then solved for the unknowns at collocations nodes using a direct elimination method. After solution, Eq. (38) can be expressed for known boundary values to explicitly calculate the solution (and its gradient : the velocity and acceleration) for any location inside the domain, without further numerical approximation. This, in fact, represents one of the major advantages of a BEM approach versus domain discretization type methods (e.g., finite differences or finite elements) : the representation of the solution over the computational domain is *exact*. The only approximation in the method resides in the discretization of the boundary and the numerical evaluation of integrals in the BIE's. Other more obvious advantages result from the limitation of the discretization to boundaries which makes the generation of discretization data and analysis of results much easier than when using domain discretization methods, and usually allows for a higher-order representation of the boundary solution and thus of the internal solution.

In an Eulerian-Lagrangian modeling approach, free surface discretization nodes represent fluid particles which, for nonlinear wave flows, slowly drift away in the direction of the mean mass transport. With time, particularly for periodic wave problems, such a node drift leads either to a concentration of nodes in flow convergence regions of the free surface (like wave crests and breakers) which creates quasi-singular situations due to node proximity, or to a poor resolution of the discretization in regions of flow divergence, like close to a wavemaker [o], which may induce instability of computations. To either add and

[o]Note that, in applications with a SFW generation, the vertical wavemaker boundary Γ_{r1} is horizontally

redistribute nodes in regions of poor resolution of the free surface or to remove and redistribute nodes in regions of flow convergence, a *node regridding* technique was introduced by Grilli and Subramanya[39] (see also Subramanya and Grilli[86]) and implemented in the model in combination with the MCI interpolation method.

4.4. Global accuracy of the solution

In the applications, accuracy of computations is checked for each time step by computing errors in total volume m and energy e of the generated wave train. As a general rule, results are deemed inaccurate and computations are stopped when—usually due to impending breaking—these errors become larger than 0.05% or so.

Based on results of computations made in various spatio-temporal discretizations, for a large solitary wave propagating over constant depth h_o, Grilli and Svendsen [46] showed that numerical errors in the model are function of both the size (i.e., the initial distance between nodes Δx_o) and the degree (i.e., quadratic, cubic,...) of boundary elements used in the spatial discretization, and of the size of the selected time step Δt_o. Based on these computations, they developed a criterion for selecting the optimum time step in the model. Using QS elements on the free surface and quadratic isoparametric elements elsewhere, they showed that, for a constant time step, errors in m and e are minimum when the mesh Courant number is approximately 0.5 or,

$$\mathcal{C}_o = \sqrt{g h_o}\,\frac{\Delta t_o}{\Delta x_o} \simeq 0.5 \tag{39}$$

Based on these results, they developed an adaptive time step procedure, applicable to highly transient waves like breakers, in which the time step is calculated as a function of time based on the optimum mesh Courant number $\mathcal{C}_o$ and on the minimum distance between nodes on the free surface, $\Delta \mid \boldsymbol{r}(t) \mid^{min}$, for the given time t as,

$$\Delta t = \mathcal{C}_o \frac{\Delta \mid \boldsymbol{r}(t) \mid^{min}}{\sqrt{g h_o}} \tag{40}$$

Similar calculations were carried out by Grilli and Subramanya [39] using the more accurate MCI elements for the interpolation on the free surface. These showed that the optimum value of $\mathcal{C}_o$ is around 0.35-0.40 for the MCI elements.

5. Applications

Many applications of the FNPF model described in Sections 2-4 were performed over the past few years for various types of wave propagation, shoaling and runup, and for wave interaction with emerged and submerged coastal structures or obstacles in the bottom. A brief review of these applications is given in Section 5.1, along with references to selected publications with more details on both computational and physical aspects of the problems.

---

moved in time with the Lagrangian motion of the first free surface node/particle, which eliminates resolution problems mentioned above, close to the wavemaker boundary.

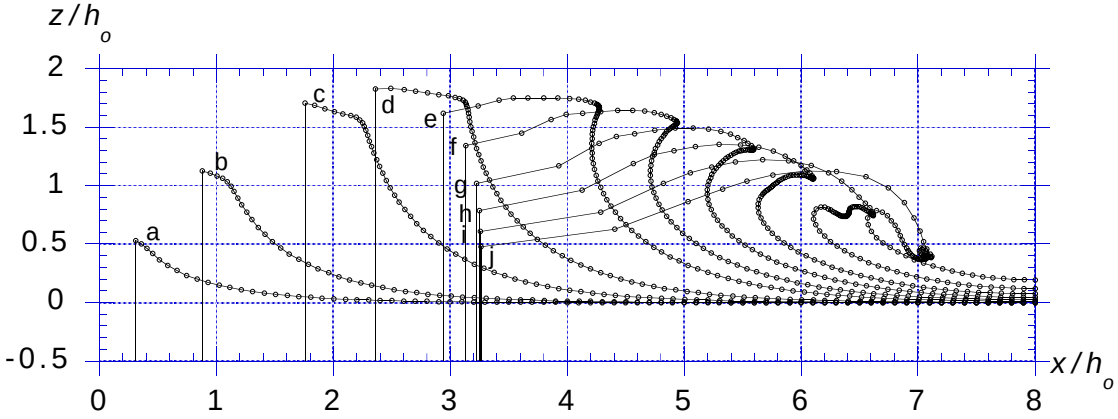

Fig. 4. Wave breaking induced by a piston wavemaker (solitary wave motion with $H'_o = 2.0$) with : $\Delta x'_o = 0.10$ and $\mathcal{C}_o = 0.4$; (○) denote discretization nodes and vertical lines mark successive locations of the piston wavemaker. Time of plotted wave profiles is $t' =$ a : 1.442, b : 2.064, c : 2.843, d : 3.381, e : 4.011, f : 4.353, g : 4.681, h : 4.936, i : 5.191, j : 5.438.

In Sections 5.2 to 5.5, details of data and results are given for specific applications of the model to problems of long wave shoaling, runup, and/or breaking over plane slopes. Although the model can address more general problems, new applications presented here have been limited to academic cases both for sake of simplicity and because of the focus of the present work on long wave runup. In this line, Section 5.5 reports on the Benchmark Problem #3 for solitary wave runup on a vertical wall that was proposed as part of the "International Workshop on Long-wave Runup Models (San Juan Island, WA, USA, 09/95).

5.1. Review of past applications of the model to long wave propagation, runup, and interaction with coastal structures

5.1.1. Wave generation by a moving vertical boundary

Grilli and Svendsen [46] studied the generation of breaking waves by horizontally moving vertical boundaries. They analyzed the accuracy of computed results as a function of both discretization and time step and evaluated the performance of corner compatibility relationships in the very demanding case where both lateral and free surface boundaries take large displacements. Similar computations were performed by Grilli and Subramanya [39], using improved free surface discretization methods (MCI elements), extended corner compatibility conditions, and node regridding methods. Fig. 4 gives an example of such computations.

Grilli [29] extended the model to the calculation of breaking bow waves and wave resistance coefficients for forward moving slender ships. This application is implemented in the present model but has not been described in this chapter.

5.1.2. Wave runup over and reflection from steep slopes

Grilli and Svendsen [42,44,45,47] and Svendsen and Grilli[87], through careful numerical experiments, extensively studied the runup on, and reflection of solitary waves from steep slopes, and from vertical walls. They compared model results to laboratory experiments and, in general, found surprisingly good agreement between both of these.

As an illustration of such computations, two applications are presented in Section 5.2 for the runup of a solitary wave of incident height $H_o/h_o = 0.12$ over slopes of angle $\theta = 20°$ and 45°, and one application is presented in Section 5.3 for the runup of a cnoidal wave of incident height $H_o/h_o = 0.10$ over a slope of angle $\theta = 20°$.

These applications were selected for sake of comparison with results earlier obtained by Liu *et al.*[61] with their nonlinear model, and experiments by Hall and Watts[49].

5.1.3. Wave shoaling and breaking over a gentle slope

Grilli *et al.*[45], Otta *et al.*[69], and Grilli *et al.*[41] used the model to calculate shoaling of solitary waves over a gentle slope up to initiation of breaking.

Grilli *et al.*[41] compared their results to classical Green's and Boussinesq's shoaling laws and to careful laboratory experiments. They concluded that none of the theoretical laws could accurately predict observed shoaling and breaking behaviors but that the present FNPF model agreed quite well with experiments up to the breaking point.

Otta *et al.* [69], based on their calculations with the model, developed a criterion for breaking of solitary waves over slopes and analyzed the kinematics of waves at breaking. Using improved numerical methods by Grilli and Subramanya[39] (particularly node regridding), Grilli *et al.*[48] performed a more detailed analysis of breaking types and characteristics of breaking jets for solitary wave shoaling over slopes 1:4 to 1:100. Based on their computations, they proposed an improved breaking criterion for solitary waves on plane slopes that was shown to agree quite well with experimental results. In particular, no solitary wave that can propagate stably over constant depth was found to break on a slope steeper than 12°. In Section 5.4, a similar application is presented for the shoaling and breaking of an incident solitary wave of initial height $H_o/h_o = 0.20$ over a slope s =1:35.

More recently, cases with periodic waves shoaling up to breaking over a slope were calculated by Subramanya and Grilli[85] and Grilli and Horrillo[31], using a combination of zero-mass-flux SFW's and an absorbing beach, to study the kinematics and integral properties of waves on beaches (Fig. 2). Such results are of importance to surf-zone dynamics modelers.

5.1.4. Wave interactions with submerged obstacles

Accurate prediction of water wave interaction with submerged obstacles is of prime importance in coastal engineering. Submerged breakwaters are becoming increasingly used as both aesthetic and economical means of shoreline protection against extreme storms and even tsunamis. Natural reefs and sandbars are frequent coastal features that function as natural submerged breakwaters. In addition, the study of waves close to the shoreline and in the surf zone requires that the offshore wave climate be accurately "propagated" over

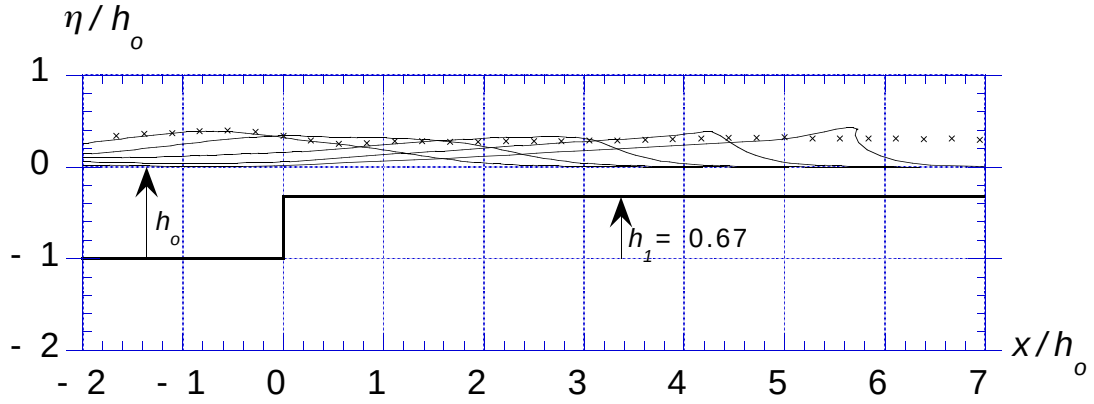

Fig. 5. Computed profiles at successive times, $t' = t\sqrt{g/h_o} = 19.45$, 20.78, 22.11, 23.44 and 24.77 (left to right), for a solitary wave of height $H_o/h_o = 0.33$ propagating and breaking over a step $h_1 = 0.67h_o$ in the bottom. Initial discretization is with $\Delta x'_o = 0.1875$ and $\mathcal{C}_o = 0.43$. Symbols ($\times$) represent the free surface envelope measured by Grilli *et al.* [32].

any existing submerged obstacle, man-made or natural.

Propagation of waves was calculated with the present nonlinear model over three different types of submerged obstacles of various engineering implications. Cases with both large incident waves or shallow submerged obstacles led to stronger nonlinear interactions between incident waves and the obstacles and to various instabilities and breaking of incident waves on or downstream of the obstacles. It is worth pointing out that most of these phenomena cannot be accurately modeled by standard wave theories but require fully (or highly) nonlinear theories to be accurately described,

- **Step in the bottom :** The simplest possible steep obstacle on the bottom is the step discontinuity between two constant depth regions (Fig. 5). Numerous studies of the interaction of a long wave with a step have been carried out using various wave theories, from linear to mildly nonlinear, and numerical models. The main motivation for these studies has been to answer the question : How do long waves behave when they propagate from deep water into shallow water over the continental shelf ? More specific questions have also been addressed, by assuming that the step represents a first approximation for a wide crested obstacle in shallow water—like a bar or a reef—or even a submerged breakwater.
  In this line, Grilli *et al.*[32] used the present model to study strong nonlinear interactions—leading to breaking—of large solitary waves over steps in the bottom. They compared numerical results to laboratory experiments and found fairly good agreement between both of these for wave shape and wave envelope. An illustration of such computations is given in Fig. 5.
- **Rectangular bar :** After the step in the bottom, the rectangular obstacle has the simplest possible geometry for representing submerged bars or breakwaters (Fig. 6). One may expect, in fact, that most of the phenomena observed or computed for rectangular bars also occur, at least qualitatively, for obstacles of more complex geometry.

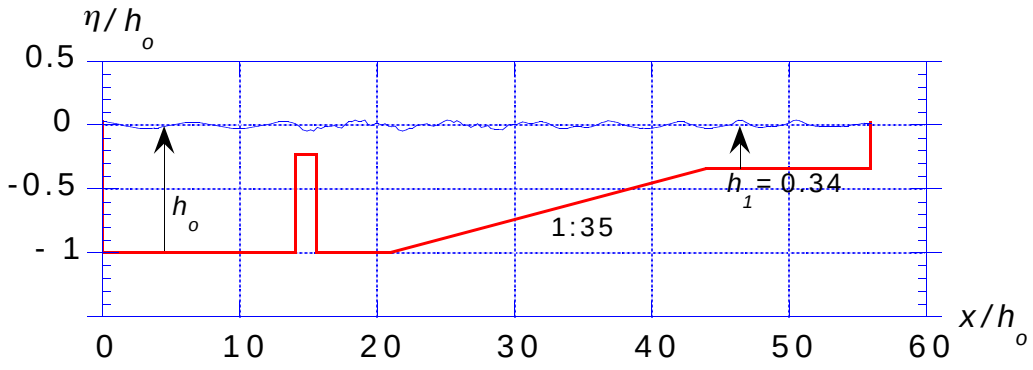

Fig. 6. Propagation of a cnoidal wave of height $H_o/h_o = 0.05$, and period $T' = T\sqrt{g/h_o} = 7.52$ over a submerged rectangular bar of height 0.768 and width 1.576. Free surface profile is plotted at $t' = 85.57$ (or $11.38T'$). Initial free surface discretization has $\Delta x'_o = 0.25$ and $\mathcal{C}_o = 0.50$. Vertical exaggeration is 10.

Driscoll *et al.* [21] studied the propagation of small amplitude cnoidal waves over a submerged shallow bar with rectangular cross-section. They compared laboratory experiments to first and second-order analytic models and to the present fully nonlinear BEM model. They found that the BEM model could accurately predict the generation of higher-order harmonics observed in laboratory in the wave train, downstream of the obstacle. An illustration of these computations is given in Fig. 6.
A similar, more extensive, numerical study was recently presented by Ohyama and Nadaoka[66].

- **Submerged trapezoidal breakwaters :** Submerged breakwaters used for shoreline protection are usually built by dropping rocks from barges at selected offshore locations and, hence, take an approximate trapezoidal shape (Fig. 7). The protection offered by submerged breakwaters consists in inducing breaking and partial reflection-transmission of large incident waves, while small wave propagation and, in some cases, local navigation can still take place over the structure during normal conditions.
Cooker *et al.* [15] used an extension of Dold and Peregrine's [18] nonlinear model to calculate solitary wave interactions with a submerged semicircular cylinder of radius R in water of depth h_o. Results showed that a variety of behaviors occur depending on wave height and cylinder radius. In short, for small cylinders ($R/h_o < 0.5$), waves essentially transmit and exhibit a tail of oscillations. This is a regime of weak interactions. For larger cylinders ($R/h_o \geq 0.5$), interactions are much stronger : small waves partially transmit and reflect (crest exchange); medium waves undergo a stronger crest exchange over the cylinder, and the first oscillation in their tail may break backward onto the cylinder (direction opposite to propagation); and large waves break forward (plunging), slightly after passing over the cylinder. A limited number of experiments confirmed these theoretical predictions.
Grilli *et al.* [34] repeated the above study for submerged breakwaters with a more realistic trapezoidal cross-section. Computations using the present model were compared

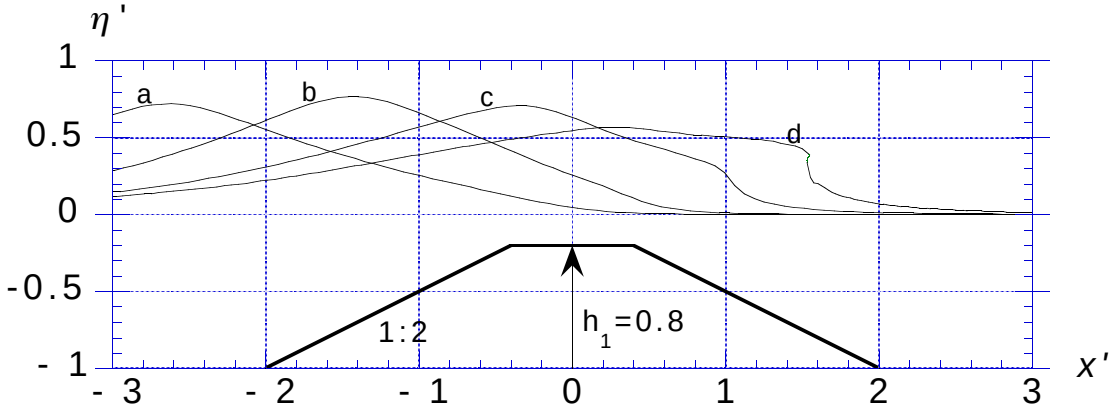

Fig. 7. Propagation of a solitary wave of height $H_o/h_o = 0.70$, (generated using Tanaka's[90] method) over a submerged trapezoidal breakwater of height $h_1 = 0.8$. Free surface profiles are given at successive times, $t' =$ a: 2.72; b: 3.69; c: 4.65; and (d) 5.20. Initial free surface discretization has $\Delta x'_o = 0.125$ and $\mathcal{C}_o = 0.50$.

to laboratory experiments for a large number of solitary waves of various heights H and for a breakwater geometry defined by : a height $h_1 = 0.8h_o$, a width at the crest $b = h_1$, and two (seaward and landward) 1:2 slopes. Results qualitatively agreed with earlier observations by Cooker *et al.* [15] as far as crest exchange and breaking behaviors are concerned. In all cases, a reflected wave formed at the breakwater seaward face and propagated backward into the tank. An illustration of such computations is given in Fig. 7.

Despite the renewed interest for underwater breakwaters mentioned above, the general conclusion of these studies is that underwater breakwaters only offer limited protection against long waves, since they only create large reflection (i.e., low energy transmission) for very low depth of their crest.

5.1.5. Wave impact on coastal structures

Two cases with more realistic coastal structures were studied in earlier applications with the model that illustrated its ability to predict shoaling of incident waves from deep to shallow water over a mild slope and interaction with a structure in the shallow water region.

In the latter application, the model was able to predict peak impact pressures from breaking waves on the vertical wall of mixed breakwater. Such numerical simulations are helpful for designing coastal structures,

- **Mixed berm breakwaters :** Most classical breakwaters used for shoreline or harbor protection are made of a main trapezoidal breakwater, with a small submerged berm at the toe of the emerged structure. Part of the incident wave energy dissipates by breaking over the berm which, hence, offers some protection to the main structure. Such a case was studied by Grilli and Svendsen [45], for which, unlike with traditional berm breakwaters, a small detached submerged structure was simply located slightly

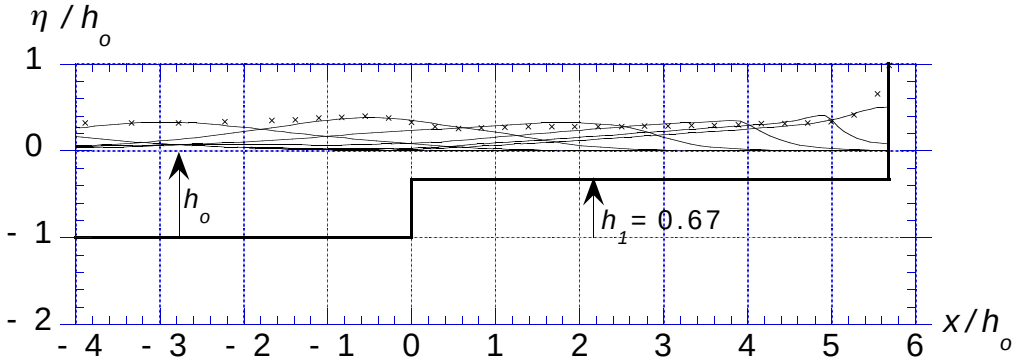

Fig. 8. Computation of solitary wave impact over a mixed vertical breakwater with a berm height $h_1 = 0.67h_o$, and length $5.7h_o$, and an incident wave height $H_o/h_o = 0.33$. Symbols ($\times$) mark free surface envelope measured by Grilli *et al.* [33].

in front of the main structure. The combination of the two structures was called a "mixed berm breakwater". This configuration, while offering the same degree of protection as classical berm breakwaters, may be more economical and simpler to build. It was found, in particular, that the toe structure could substantially reduce maximum runup of solitary waves on the main steep slope.

- **Mixed vertical breakwaters :** Mixed vertical breakwaters are composed of a vertical concrete caisson sitting on a wide berm made of rocks. They function as vertical walls during high tide and as mound breakwaters during low tide (Fig. 8). Their upper section is designed to be safe against sliding and overturning induced by wave impact force. Laboratory and field experiments show that impacts of normally incident breaking waves are the most severe. In this case, the maximum impact force on the wall may rise up to 10 times the hydrostatic force based on wave elevation at the wall.

  Cooker [12] and Cooker and Peregrine [14] confirmed these observations by solving 2D fully nonlinear potential flows. Their model, however, although very accurate, was limited to a simple vertical wall and used a large incident long wave with characteristics selected to create a large scale breaker in the model.

  Grilli *et al.* [33,35] computed violent impacts of breaking waves on mixed vertical breakwaters with the present nonlinear model, i.e., using both more realistic incident waves and a breakwater geometry closely reproducing the experimental set-up. An example of such computations is given in Fig. 8. Good qualitative agreement was found between laboratory experiments and computations but the model overpredicted peak pressures by up to 50%. This is believed to be due in large part to geometric irregularities in the experimental set-up that limited both the jet formation and the pressure build up at the wall. In fact, a poor repeatability was found for measured peak pressures whereas wave shape and kinematics could be reproduced to within a few percent for 9 repetitions of the same experiment.

5.2. Runup of solitary waves on a steep slope

The computational domain for this problem is similar to the case sketched in Fig. 3, except that, due to the steep slope used in the present case, there is no need for a shallow shelf at the rightward extremity of the computational domain (Γ_{r2}). The domain length is 30 times the depth. The runup of a solitary wave of incident height $H_o/h_o = 0.12$ is calculated over two slopes of angle $\theta = 20°$ and 45°. The incident wave is generated by simulating a piston wavemaker on the leftward boundary (Γ_{r1}).

For the first slope, a discretization with 120 two-node QS elements is used on the free surface. Three-node isoparametric elements are used on the leftward boundary, on the rightward boundary (i.e., the slope in the present case), and on the bottom. The discretization thus has 254 nodes and 185 elements with an initial distance between nodes $\Delta x_o = 0.25$ on the free surface, 0.167 on boundary Γ_{r1}, 0.20 on boundary Γ_{r2}, and 0.25 on the bottom Γ_b. The initial time step is $\Delta t_o = 0.09$ and the Courant number is thus $\mathcal{C}_o = 0.36$ (with $g = h_o = 1$). The average CPU time per time step is 3.3 s (IBM9000/3) or about 66 min for the whole run of 1200 time loops. Similar data are generated for the 45° slope.

Results for the free surface elevation at selected times are presented in Fig. 9 (20° slope) and Fig. 10 (45° slope). One can see that waves propagate from left to right up to about $t' = 43$ (curves a-f) and 41 (curves a-e), respectively. The maximum runup calculated for both slopes is $R_u = 2.351 H_o$ (at $t' = 43.07$), and $R_u = 2.275 H_o$ (at $t' = 41.16$), respectively, which agrees quite well with both computations by Liu *et al.*[61] and experiments by Hall and Watts[49]. After runup, waves rundown, reflect on the slopes, and propagate backward into the numerical tank (curves f-l and e-l), trailing a (well resolved) tail of oscillations behind them, slightly more pronounced for the smaller slope. For time $t' \geq 60$, the leading oscillations in the reflected waves re-reflect on the wavemaker.

Fig. 11 gives indicators of global accuracy of computations for each case. These are the relative errors on total (dimensionless) wave energy $\Delta e/e$ and volume $\Delta v/v$, in which $e = 0.06762$ and $v = 0.83227$ for the generated solitary wave. Both numerical errors are small quantities for the initial stages of wave propagation ($\mathcal{O}(10^{-7})$) and then gradually increase. Errors temporarily decrease during runup and rundown of the waves on the slopes and then increase to stabilize at about $\mathcal{O}(10^{-3})$ or smaller [p].

5.3. Runup of cnoidal waves on a steep slope

The runup of a cnoidal wave of incident height $H_o/h_o = 0.10$ and period $T\sqrt{g/h_o} = 20$ (i.e., $\omega = 0.31416$, for which $L/h_o \simeq 20$) is calculated over a slope of angle $\theta = 20°$, using the same discretization and initial data as for the solitary wave in the previous Section. The wave is generated by a piston wavemaker with motion $x_p(t)$ as in Fig. 13a.

Results for the free surface elevation at selected times are presented in Fig. 12. One can see that waves propagate from left to right and a first crest runs-up the slope at about $t' = 36$ (curve d), reflects, and then propagates back into the tank. This crest then interacts with the second crest to produce a slightly larger runup for the second crest at about $t' = 56$

[p] Accuracy of these results can be greatly improved by using MCI elements on the free surface instead of QS elements. This will be illustrated in the applications in Sections 5.4 and 5.5.

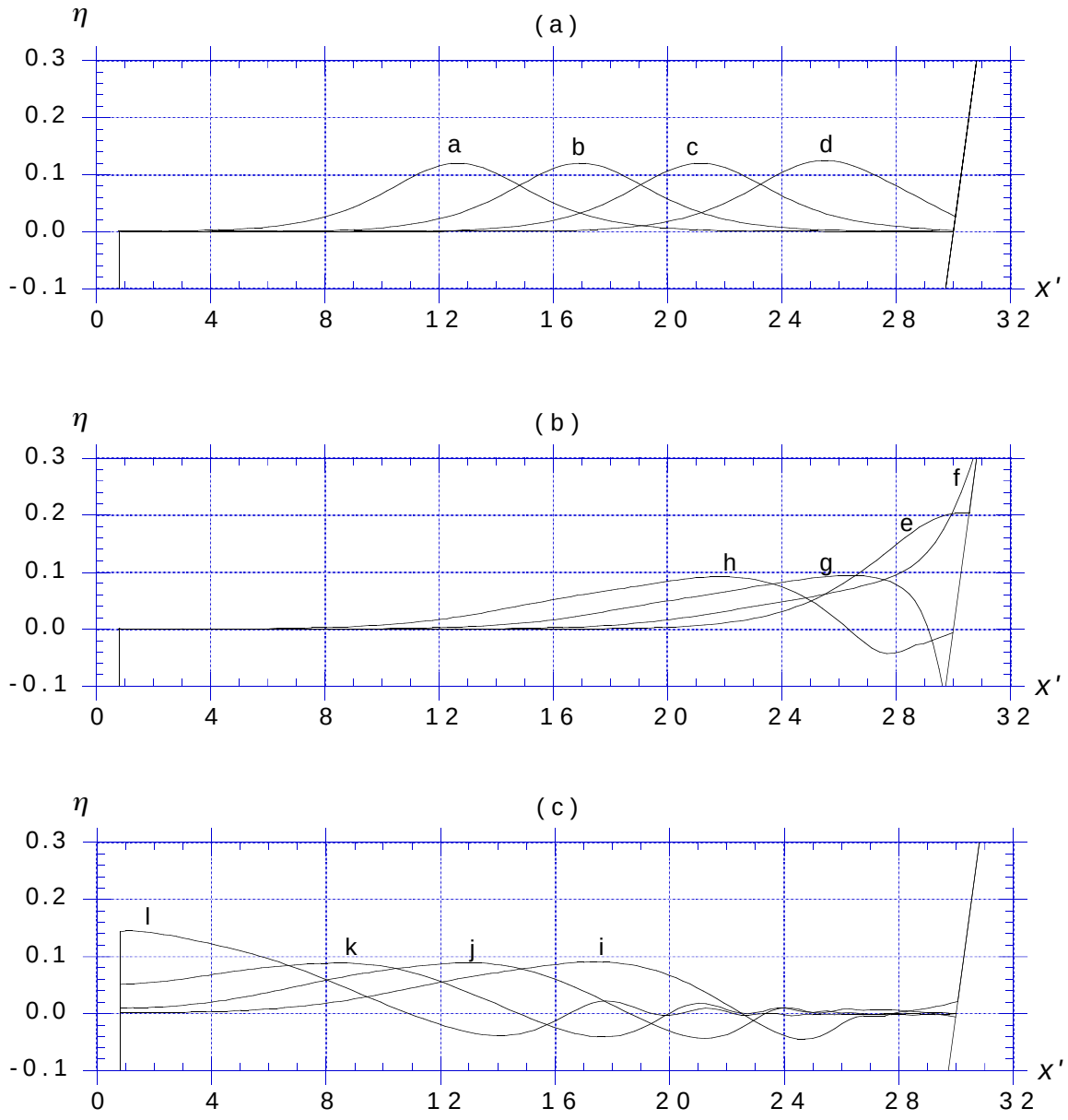

Fig. 9. Runup of a solitary wave of height $H_o/h_o = 0.12$, on a 20° slope. Axes are non-dimensional with respect to depth h_o and curves correspond to successive dimensionless time $t' =$ a: 24; b: 28; c: 32; d: 36; e: 40; f: 44; g: 48; h: 52; i: 56; j: 60; k: 64; l: 68.

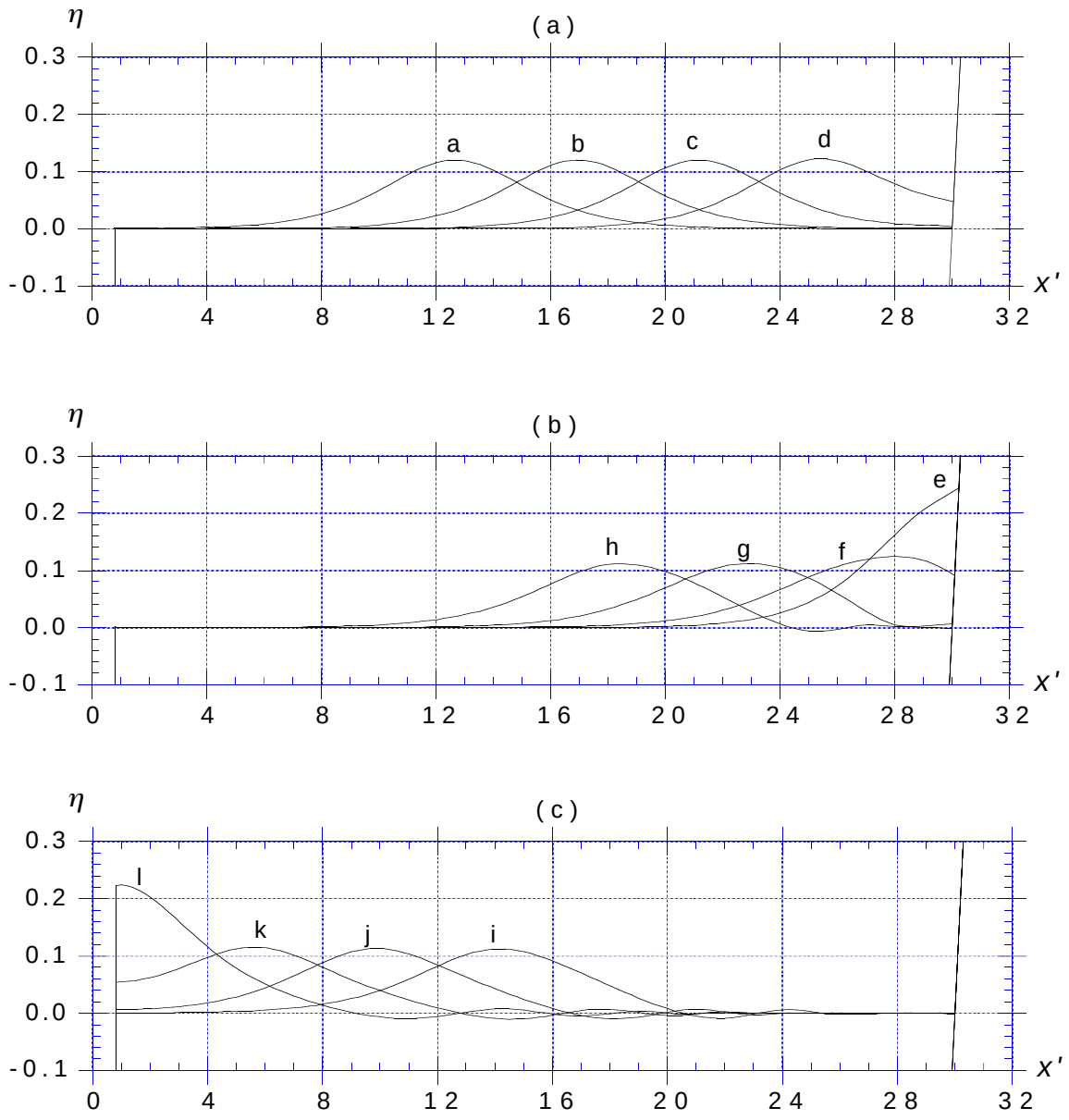

Fig. 10. Runup of a solitary wave of height $H_o/h_o = 0.12$, on a 45° slope. Axes are non-dimensional with respect to depth h_o and curves correspond to successive dimensionless time $t' =$ a: 24; b: 28; c: 32; d: 36; e: 40; f: 44; g: 48; h: 52; i: 56; j: 60; k: 64; l: 68.

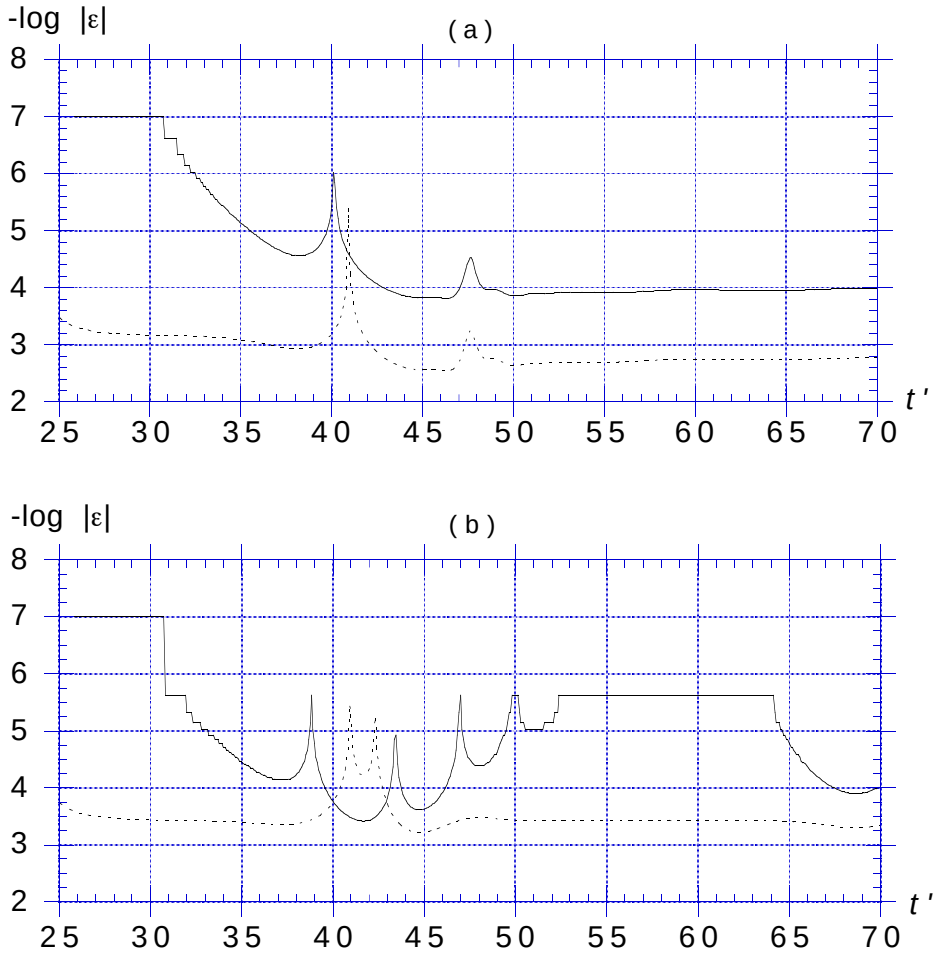

Fig. 11. Relative numerical error on total wave energy (- - - - -) $\varepsilon = \Delta e/e$, and volume (———) $\varepsilon = \Delta v/v$, for the computations reported in : (a) Fig. 9; and (b) Fig. 10.

(curve i), and so forth. The time history of runup on the slope in Fig. 13b confirms that the second and later runups are reinforced by successive incoming crests. The first crest runs-up to about twice the incident wave height, and the second and third crests run-up to about 2.4 times the incident wave height, while keeping the same rundown value. These results also fairly well agree with results by Liu *et al.* [61], as far as one can tell from their figures.

Fig. 13c shows the relative error, $\Delta V/V$, on total volume of the computational domain ($V = 28.626$), as a function of time. One sees that this error stays quite small during all computations.

5.4. Solitary wave shoaling and breaking over a gentle slope

A case similar to those calculated by Grilli *et al.*[41] and Otta *et al.* [69] (also analyzed by Wei *et al.*[93]) is presented in the following, for the shoaling and breaking of an incident solitary wave of initial height $H'_o = 0.20$ over a 1:35 slope. The computational domain is as sketched in Fig. 3 with the toe of the slope at $x' = 5$. The incident solitary wave is generated on the leftward lateral boundary of the domain using the numerical piston wavemaker. To improve accuracy of regular integrations in the upper part of the slope where the domain geometry becomes very narrow, a small shelf is specified to the right of the domain in depth $h_1 = 0.1h_o$ (unlike in computations with steeper slopes reported in the previous Sections) [q].

The free surface discretization has 226 two-node MCI elements, with $\Delta x'_o = 0.20$, and there are 100 quadratic elements on the bottom and lateral boundaries. The total number of nodes is 429. The distance between nodes on the bottom is 0.5 in the constant depth region, and reduces to 0.40, 0.25, 0.20, 0.15, and 0.10 on the slope, in order to get increased resolution where depth decreases. The distance between nodes is 0.15 on the shelf bottom. Adaptive integration with up to 2^6 subdivisions (as function of the geometry) is specified on the free surface and on the bottom, for the elements located between $x' = 31$ and 40. The mesh Courant number is $\mathcal{C}_o = 0.40$ and, hence, $\Delta t'_o = 0.08$. With these data, the CPU time is 12.9 sec per time step (IBM9000).

Fig. 14a shows computed stages of wave shoaling and breaking. During propagation, time step reduces down to $\Delta t' = 0.020$ at the time of breaking defined by a vertical tangent occurring on the front face (curve d in Fig. 14a, $t' = 44.52$, $x'_b = 36.3$). The total number of time steps up to this stage is 950 and the average time step is 0.047. The wave height at breaking is $H_b = 0.364$ and the ratio wave height over depth at breaking is $H_b/h_b = 1.402$. This is much larger than the usually accepted value for gentle slopes (~ 0.80) and agrees to within 5% with measurements by Grilli *et al.*[41]. A detailed comparison of free surface elevations measured at several locations over the slope (gages) to computed results is given in Fig. 14c. One can see that the agreement between both of these is very good up to the last gage which is virtually at the computed breaking point.

---

[q] This is to avoid that elements on different parts of the boundary get too close to each other, leading to a loss of accuracy of numerical integrations of the Green's function kernels. This change in geometry—as compared to a plain slope—does not affect shoaling and breaking of a solitary wave, provided these occur, as observed in the present case, before reaching the shelf, i.e., for $x' \leq 41$.

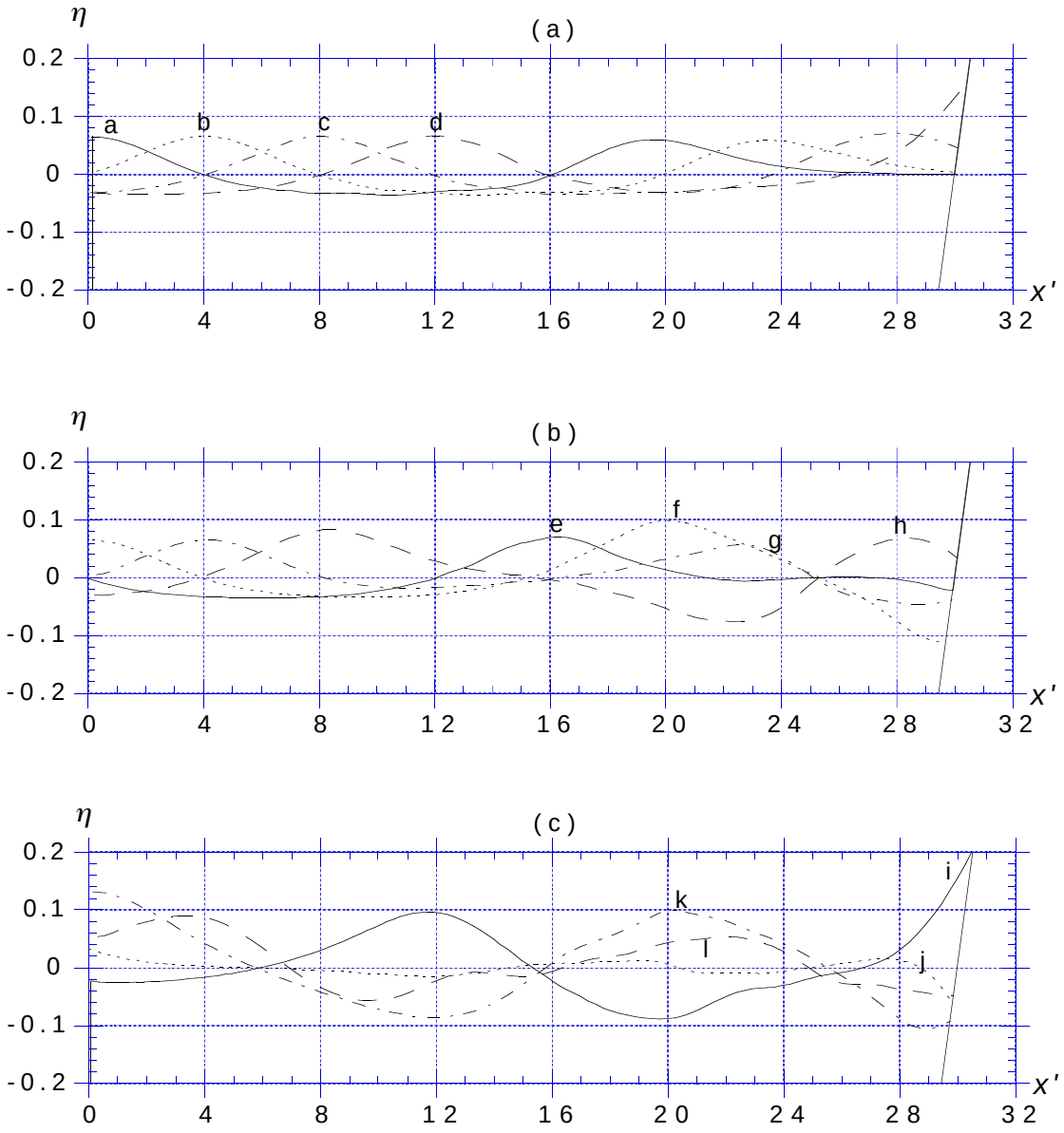

Fig. 12. Runup of a cnoidal wave of height $H_o/h_o = 0.10$ and period $T' = T\sqrt{g/h_o} = 20$, on a 20° slope. Axes are non-dimensional with respect to depth h_o and curves correspond to successive dimensionless time t' = a: 24; b: 28; c: 32; d: 36; e: 40; f: 44; g: 48; h: 52; i: 56; j: 60; k: 64; l: 68.

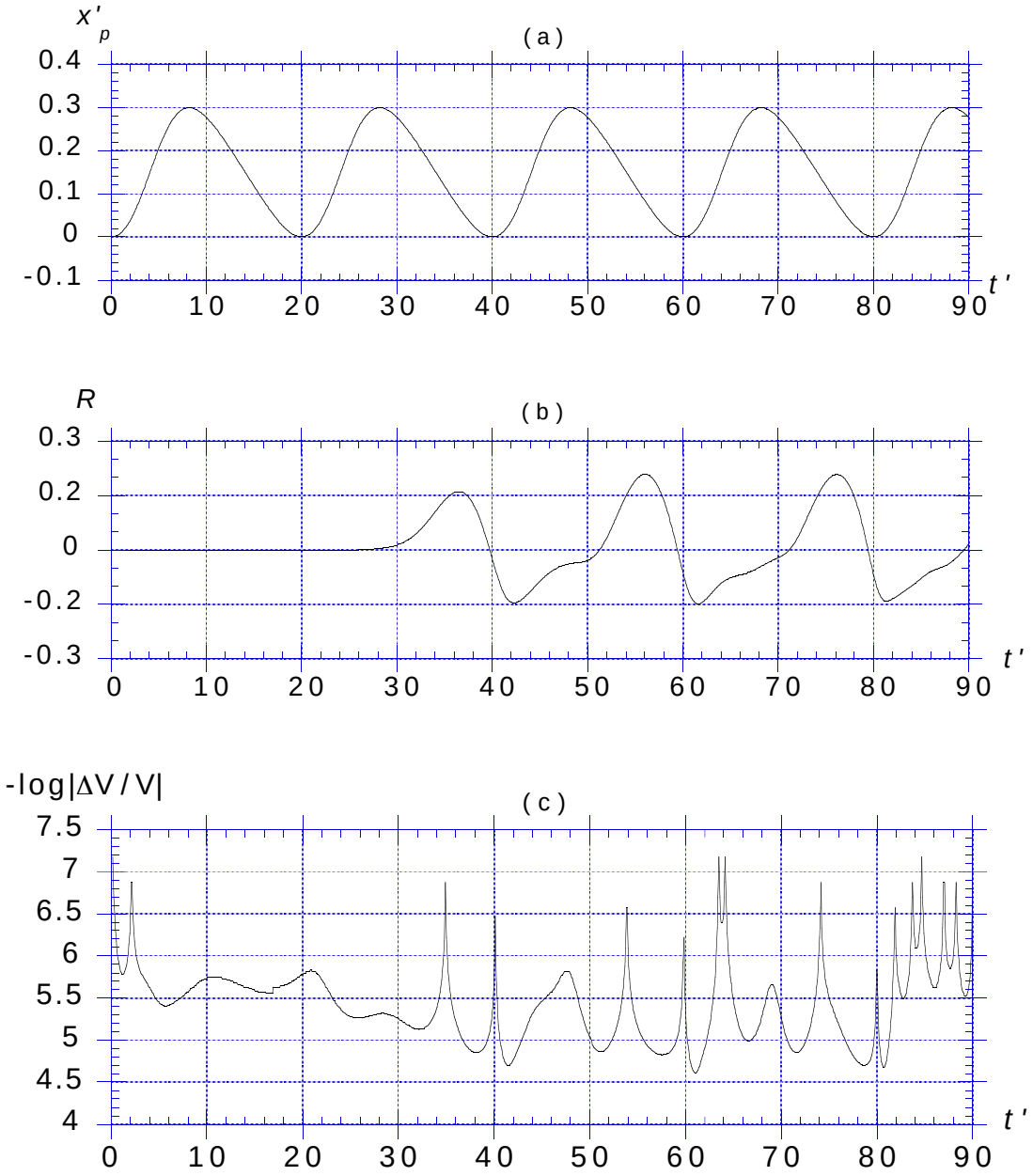

Fig. 13. (a) Horizontal motion of piston wavemaker $x_p(t)$ for cnoidal wave generation; (b) runup at the slope $R(t)$; and (c) relative numerical error on computational domain volume, $\Delta V/V$, for the computations reported in Fig. 12.

To be able to accurately pursue computations beyond the breaking point, the regridding method by Subramanya and Grilli[86] and Grilli and Subramanya[39] is used to add 40 nodes in the crest region, between $x' = 33.26$ and 37.80, at the time of curve d (Fig. 14). Computations are restarted and Fig. 14b shows blow-ups of the region over the slope where breaking occurs. Discretization nodes are marked on the figure and one sees that the breaker jet is well resolved up to touch down on the free surface. The wave breaks as a large scale plunging breaker. Details and accuracy for such computations beyond the breaking point are discussed in Grilli and Subramanya[39] and a further analysis of results is done in Grilli *et al.*[48].

5.5. Solitary wave runup on a vertical wall : Benchmark #3

5.5.1. Wave generation

In Benchmark #3 application, three solitary waves were generated in a laboratory tank at the U.S. Army Engineering Waterways Experiment Station (Vicksburg) using a piston wavemaker with motion $x_p(t)$ provided to the workshop participants as a set of digital data.

Wavemaker motion Eq. (D.6) was first used to best fit the digitized paddle trajectories and find corresponding incident waves $H'_o = H_o/h_o$ to be used in Eq. (D.7) to calculate boundary conditions (C.5), for the paddle velocity and acceleration as a function of time on boundary Γ_{r1}, needed to generate solitary waves in the model (Fig. 15). We thus obtained $H'_o =$ (case A) 0.0440; (case B) 0.2602; and (case C) 0.6087. As can be seen, with these wave heights, only small differences are observed between experimental and calculated curves.

5.5.2. Wave propagation over constant depth

The wave tank geometry provided to the workshop participants is sketched in Fig. 16 with a region with constant depth, $h_o = 0.218$ m, length $68.991h_o$, and three successive slopes 1:53 (length $20.00h_o$), 1:150 (length $13.44h_o$), and 1:13 (length $4.13h_o$). A vertical wall is located at the tank far end.

In all three cases, due to the large region of constant depth in front of the slopes, to save computational time, waves were first generated and propagated in a (shorter) computational domain of constant depth h_o and length $69h_o$. Waves were then introduced in a second computational domain containing part of the constant depth region and the rightward region of the tank with varying water depth. Doing so, parts of the oscillatory tails shed behind the generated waves were cut out of the second computational domain whereas the main leading waves were kept for further propagation over the slopes.

The same discretization was used in all three cases for the constant depth domain, with 141 nodes on the free surface and 140 MCI elements ($\Delta x'_o = 0.5$) and three-nodes quadratic elements elsewhere, with a node spacing 0.5 on the bottom. Initial time step was $\Delta t'_o = 0.15$ for a Courant number 0.3. For the propagations over constant depth, relative errors on wave volume and energy were typically small in all three cases, around 0.001%

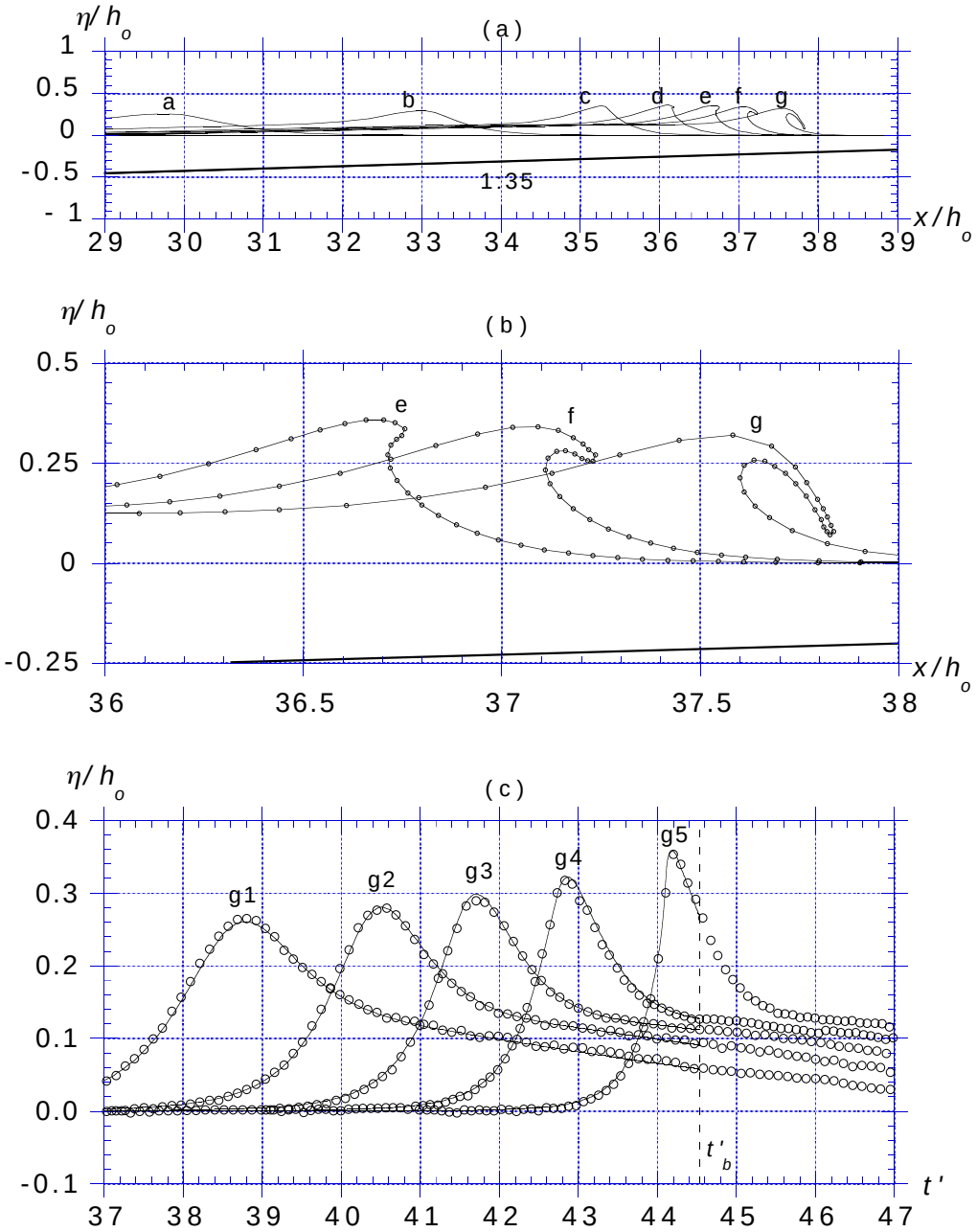

Fig. 14. Shoaling and breaking of a solitary wave with initial height $H_o' = 0.20$, over a 1:35 slope. The wave is generated by a piston wavemaker at $x' = 0$. The slope starts at $x' = 5$ and plots in Fig. (a) correspond to profiles at time t' = a: 37.17; b : 40.73; c: 43.48; d: 44.53; f: 44.94; f: 45.40; g: 46.00. Fig. (b) is a blow-up of last three profiles in (a) with (○) denoting BEM discretization nodes. Fig. (c) shows a comparison of computed (——) and measured (○) free surface elevation at gages at x' = g1: 30.96; g2: 32.55; g3: 33.68; g4: 34.68; and g5: 36.91 (from Grilli *et al.*[41]).

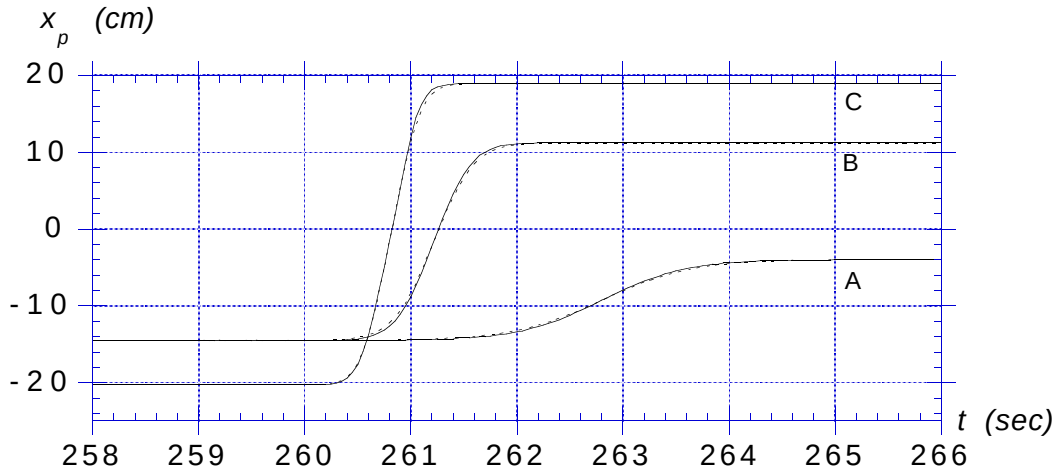

Fig. 15. Piston wavemaker paddle trajectories $x_p(t)$ for Benchmark #3 application : (——) experimental; (- - - - -) numerical with H_o' = (case A) 0.0440; (case B) 0.2602; and (case C) 0.6087.

or less.

Time histories of surface elevation computed at gages 1-3 are given in Fig. 17 for all three cases. One can see that, as expected, the larger the wave the larger and the longer the tail of oscillations it sheds behind its main crest. This is due, as discussed before, to the piston wavemaker generation of approximate (first-order) solitary waves in the tank. When shedding tails of oscillations, as pointed at by Grilli and Svendsen[47], the main crest height of waves also gradually decreases over constant depth until the wave shape stabilizes and the main crest adjusts to the (more peaky) shape of exact solitary waves (those that Tanaka's[90] method would have generated). Thus at gage 2, for instance, the computed maximum wave height is, 0.0440, 0.254, and 0.589, for cases A, B, and C, respectively, i.e., 0.0, 2.4, and 3.2% smaller than the incident wave generated at $x' = 0$, respectively. It is seen that these maximum values do not significantly change from gage 2 to 3, indicating that incident waves have reached their permanent form. Finally, one also sees from the results that the wave for case A has the theoretical height specified at the wavemaker and no noticeable oscillatory tail, confirming that such a small wave (with $H_o' < 0.2$ according to Goring[25]) has a shape very close to a first-order solitary wave.

5.5.3. Wave propagation over the sloping bottom and runup on the wall

Computations are pursued in the second computational domain. For case A, the domain extends from $x' = 18.72$ onward, with a total of 491 nodes, 150 of which on the free surface ($\Delta x_o' = 0.5$) and 370 elements. The distance between nodes on the bottom is progressively reduced from 0.5 to 0.15. For case B, the domain extends from $x' = 46.1$ onward (the wave is higher and much narrower and travels faster than in case A), with a total of 471 nodes, 240 of which on the free surface ($\Delta x_o' = 0.25$) and 378 elements. The distance between nodes on the bottom is progressively reduced from 0.5 to 0.15. For case C, the domain is chosen identical to case B.

Fig. 18 gives a summary of results computed for case A. In Fig. 18a, the time history of

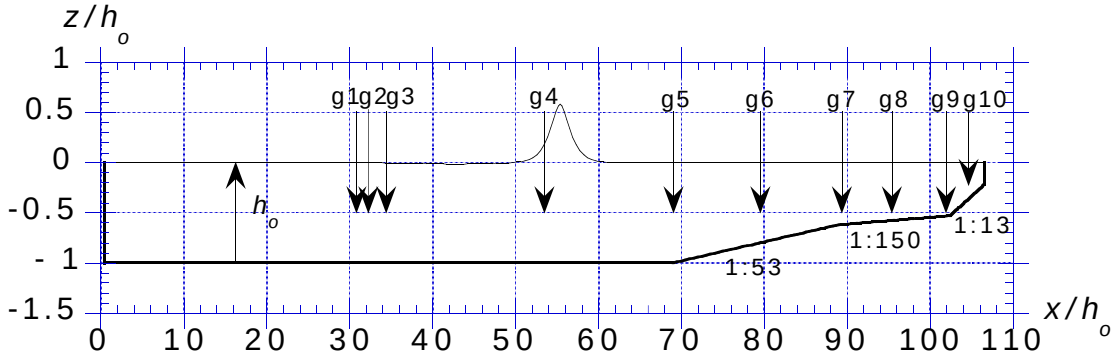

Fig. 16. Sketch of computational domain for Benchmark #3 application with 10 gages located at $x' =$ g1: 31.00; g2: 32.00; g3:34.00; g4: 54.00; g5: 69.00; g6: 79.00; g7: 89.00; g8: 95.69; g9: 102.43; g10: 104.50. Sketched wave corresponds to case C at $t' = 49.00$.

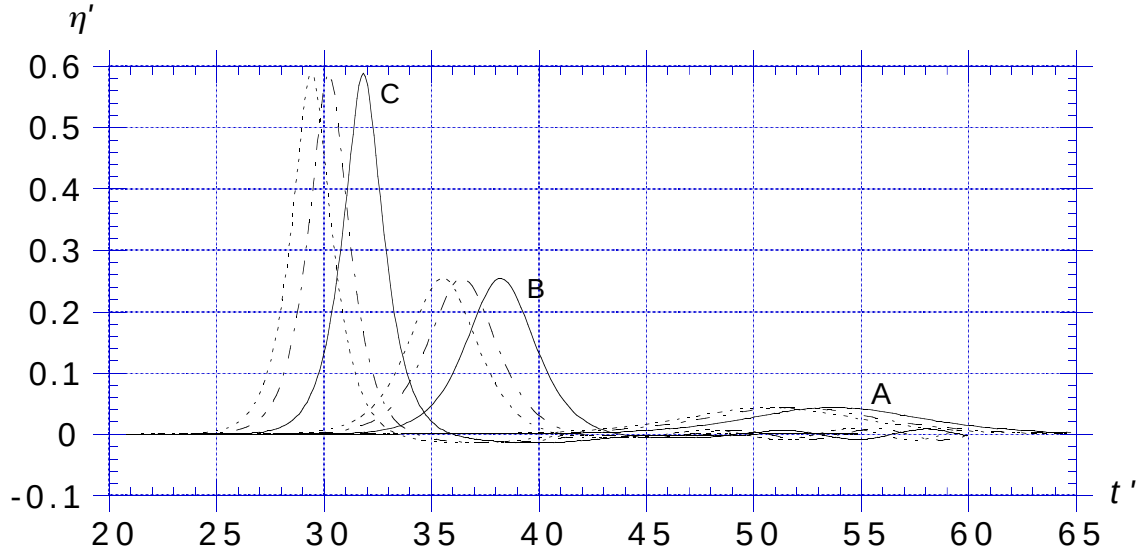

Fig. 17. Free surface elevation at : (- - - - -) gage 1; (— . —) gage 2; and (———) gage 3, for computations with cases A, B, C.

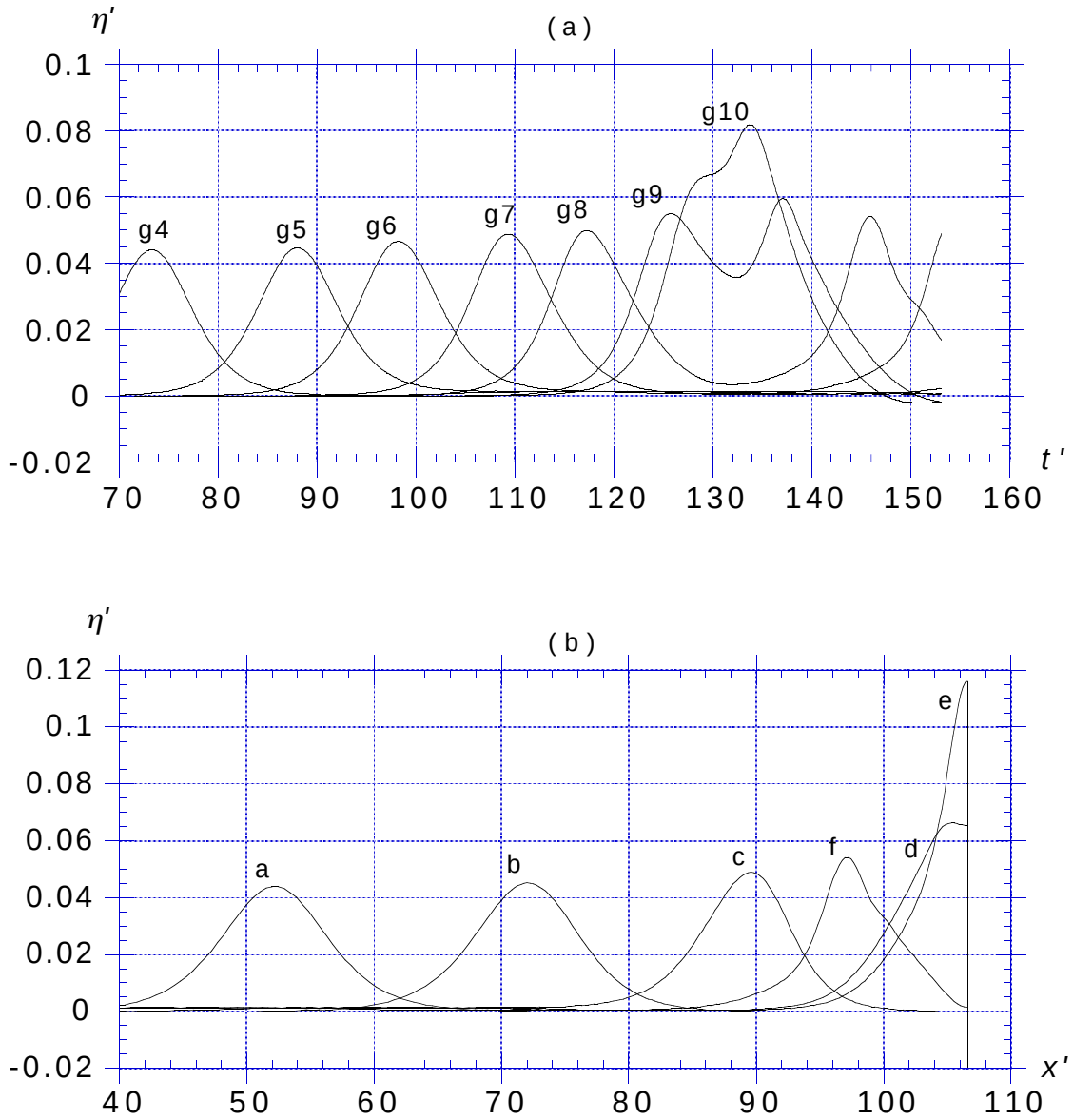

Fig. 18. Case A. (a) Free surface elevation as a function of time at gages 4-10; (b) Free surface profile at $t' =$ a: 71.55; b: 91.04; c: 109.99; d: 128.25; e: 131.25 (runup); and f: 153.12 (reflection).

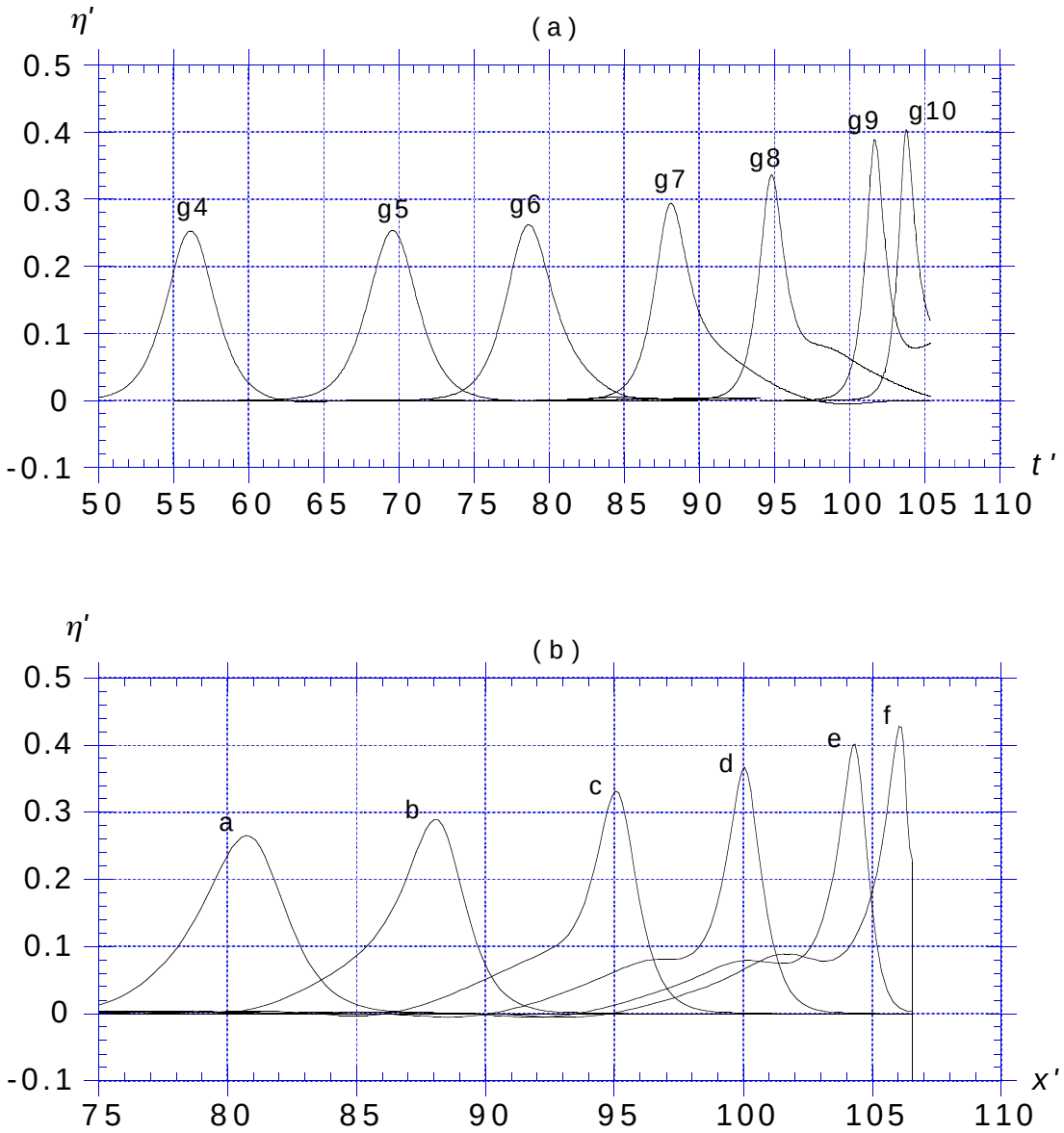

Fig. 19. Case B. (a) Free surface elevation as a function of time at gages 4-10; (b) Free surface profile at $t' =$ a: 80.24; b: 87.20; c: 94.108; d: 99.18; e: 103.92 ; and f: 105.32 (impending runup).

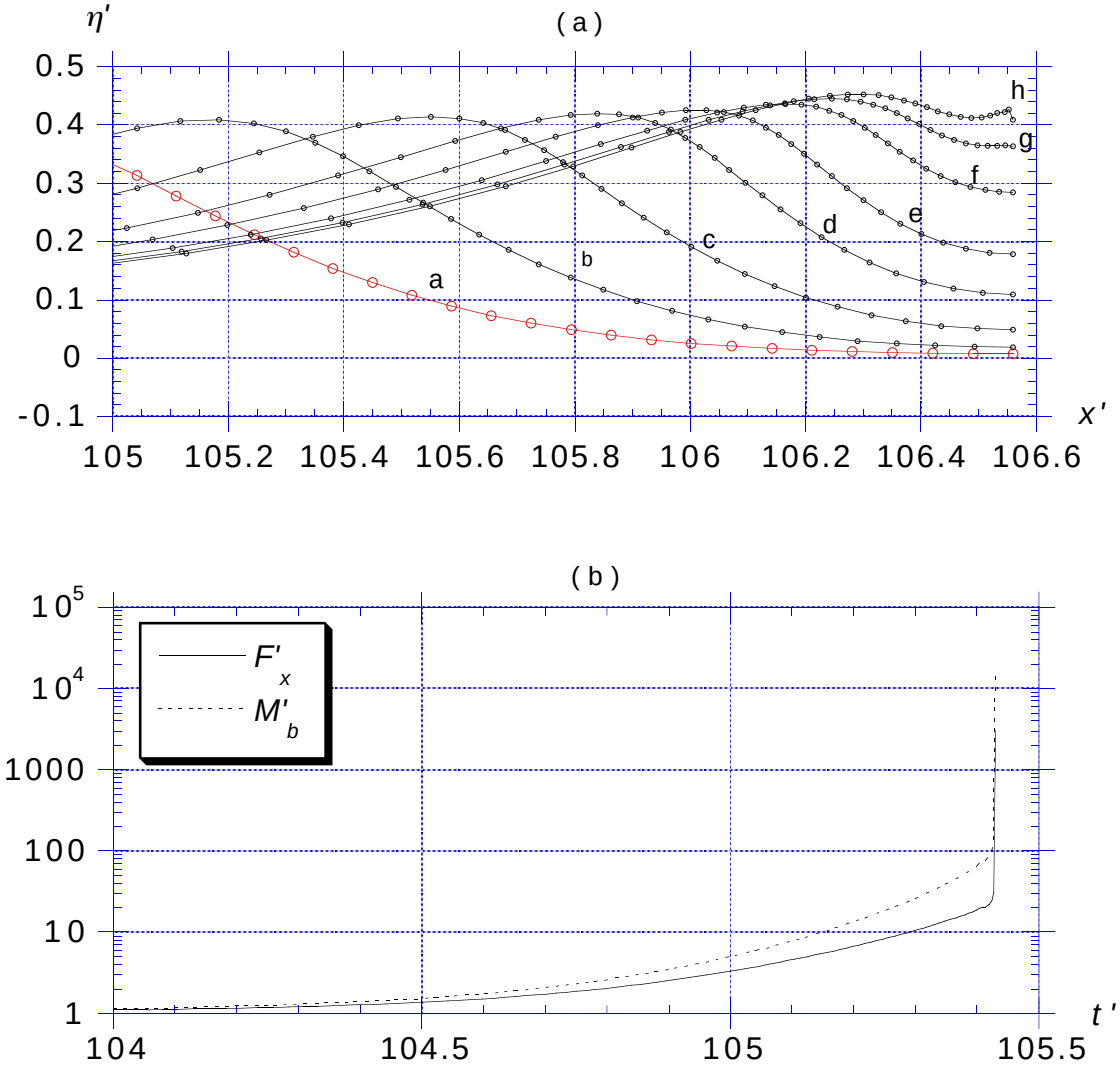

Fig. 20. Case B. after node regridding (a) Free surface profile at $t' =$ a: 104.00 (first regridded profile); b: 104.42; c: 104.78; d: 105.05; e: 105.20 ; f: 105.33; g: 105.39 ; and h: 105.43 (impending upward jet expulsion) ((○) indicate regridded discretization nodes; no scale distorsion); (b) Dimensionless horizontal pressure force, $F'_x = F_x/(\frac{1}{2}\rho g d^2)$ and moment with respect to the bottom, $M'_b = M_b/(\frac{1}{6}\rho g d^3)$, on the vertical wall ($d = 0.22$ is the depth at the wall, and denominators denote still water values).

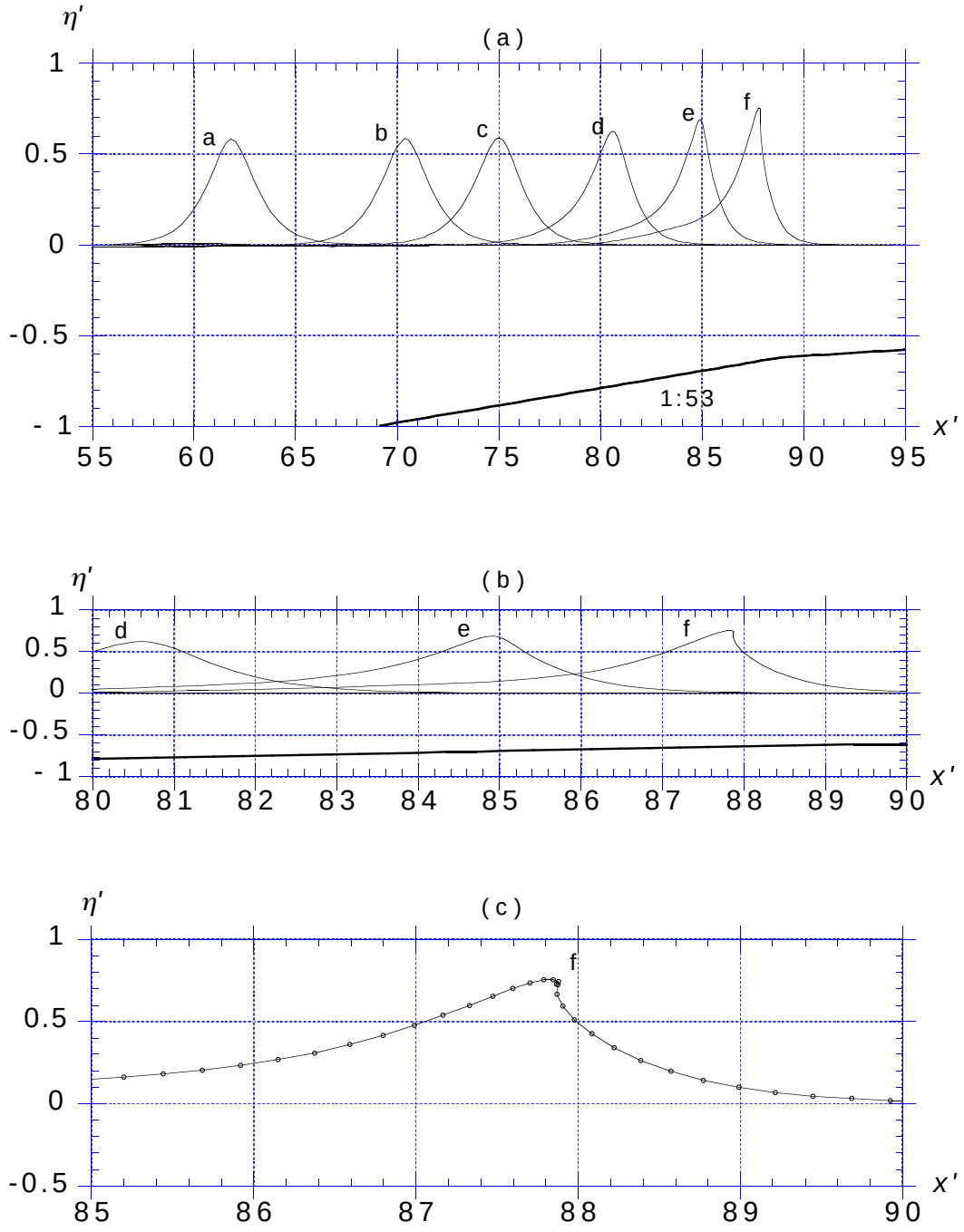

Fig. 21. Case C. (a) Free surface profile at $t' =$ a: 54.21; b: 61.08; c: 64.76; d: 69.23; e: 72.65 ; and f: 74.86 (breaking at $x'_b = 87.85$); (b) blow-up of (a) without distorsion of scales; (c) further blow-up of (b) showing the breaking crest with discretization nodes (○).

water elevation at gages 4-10 shows wave transformation up to runup and reflection from the wall and, in Fig. 18b, selected free surface profiles are given for 6 times (curves a-f), with curve e representing the maximum runup occurring at $t' = 131.25$ (i.e., $t = 19.57$ sec) from the start of wave generation in the model. Maximum runup computed on the wall is $\mathcal{R}' = 0.1163 = 2.643 H'_o$. During these computations, relative errors on wave volume ($v = 0.4842$) and energy ($e = 0.2564$) were less than 0.032 and 0.027%, respectively.

Fig. 19 gives a summary of results for case B. In Fig. 19a, the time history of water elevation at gages 4-10 shows wave transformation up to impending runup on the wall and in Fig. 19b, selected free surface profiles are given for 6 times (curves a-f) with curve f, at $t' = 105.32$, representing the closest time to maximum runup that can be accurately computed in this discretization. Unlike with case A, the much larger wave generated in case B significantly feels the bottom and becomes more and more asymmetric as it propagates towards the wall. This is similar to shoaling computations in Fig. 14. Curves e and f in Fig. 19b even show the formation of a secondary crest behind the main wave crest indicating the initiation of reflection from the steep 1:13 slope and from the wall. During these computations, relative errors on wave volume ($v = 1.202$) and energy ($e = 1.164$) were less than 0.017 and 0.0017%, respectively, up to $t' = 95$. For later times, these errors increased up to 0.39% and 0.085%, respectively, at the time of curve f. These increased errors clearly indicate the need for a finer discretization of the free surface close to the wall, to be able to compute further in time and resolve the "flip-through" motion of the free surface which is about to happen in front of the main crest.

This can be achieved through regridding of the free surface to a finer discretization : 30 nodes are added to the free surface at $t' = 104.00$ (Fig. 20a, curve a), from $x' = 103.13$ to the wall. The new spacing between nodes in the regridded region is approximately 0.07. Computations are accurately pursued in the new discretization up to the time a small jet of water is about to be vertically expelled at the wall (Fig. 20a, curve h, $t' = 105.43$). At this stage, numerical errors reach (an acceptable) 0.25% and one can see in Fig. 20a that small features in free surface shape are quite well resolved. Beyond this time, the few nodes close to the wall are vertically expelled with very large upward velocity and acceleration (thousands of g's) and computations break down. This is consistent with computations by Cooker and Peregrine[14] and Grilli *et al.*[33] and is also supported by experiments in the latter study. For the last computed profile, the runup at the wall is $\mathcal{R}_u = 0.435 = 1.67 H'_o$. After jet expulsion, however, this value is likely to become much larger. As in the previous studies, we also see in Fig. 20b that the computed horizontal pressure force on the wall and moment with respect to the toe of the wall also reach very large (impact) values shortly after the time of curve h in Fig. 20a (0.0033 time unit later).

Fig. 21 gives a summary of results for case C. In Fig. 21a, selected free surface profiles are given for 6 times (curves a-f) with curve f, at $t' = 74.86$ (or $t = 11.16$ sec from the start of wave generation), representing the time at which the wave breaks, with $H'_b = 0.7536, h'_b = 0.644, x'_b = 87.85$, and a breaking index $H_b/h_b = 1.169$. Fig. 21b gives a blow up without scale distorsion of the region of Fig. 21a where breaking occurs and Fig. 21c gives a blow-up of the breaking crest in curve f, with indication of computational points. The breaker shape is fairly well resolved. During these computations, relative errors on wave volume ($v = 1.803$) and energy ($e = 1.663$) were less than 0.05% for most

of the propagation but increased to 0.12 and 0.55%, respectively at the time of breaking, when nodes in the crest move very close to each other (Fig. 21c). To accurately compute results further than this time would require using regridding techniques similar to those in Grilli and Subramanya[39] illustrated by results in Fig. 14b.

It is of interest to note that, according to the (numerical/experimental) studies of breakers by Grilli *et al.*[48], the wave in case C has a slope parameter $S_o = 1.521s/\sqrt{H'_o} = 0.0246 < 0.025$ (with $s = 1:53$) and should thus (barely) break as a spilling breaker. This seems to be supported by results in Fig. 21c when considering the fairly small size of the breaker jet. Empirical relationships based on parameter S_o (best fit through both experimental and numerical results) would further give, for the breaking characteristics at the time the wave front face reaches vertical tangent (i.e., slightly before the time of curve f), $H_b/h_b = 0.985$ and $h'_b = 0.729$, $H'_b = 0.72$. This is also in fairly good agreement with the present results.

In conclusion, for case C, breaking interrupts computations with the model and wave runup cannot be further calculated.

5.5.4. Comparison of numerical results with experiments

During the workshop, participants were provided with surface elevations measured at gages 7 and 9 in the experiments carried out in Vicksburg. Since the wave for case C broke before reaching those gages, a comparison with numerical results has only been made in Fig. 22 for cases A and B and numerical and experimental results have been synchronized in time at the location of gage 7.

For case A (Fig. 22a), the incident profiles at gage 7 are in quite good agreement, and similarly at gage 9. The experimental incident wave just seems a little smaller, which might be due to frictional effects during propagation in the tank. The reflected wave at gage 9 is also slightly smaller in the experiments and propagates through the gage slightly later in time than the computed wave, due to its smaller speed. Overall, the agreement is quite good.

For case B (Fig. 22b), the incident profiles at gage 7 are in quite good agreement, and similarly in gage 9, except that, in this case, the experimental wave is higher and, in fact, has more volume than the numerical wave. The reason for this is unknown. Computations unfortunately had to be interrupted before the reflected wave came back, due to the violent flip-through motion at the wall discussed before.

Acknowledgments

The author wishes to acknowledge support for this research from the NRL-SSC grant N00014-94-1-G607, from the US Department of the Navy Office of the Chief of Naval Research. The information reported in this work does not necessarily reflect the position of the US Government. Frederic Estadieu, a visiting student from ECN Nantes in France is acknowledged for his help in running the computations for Benchmark #3 applications.

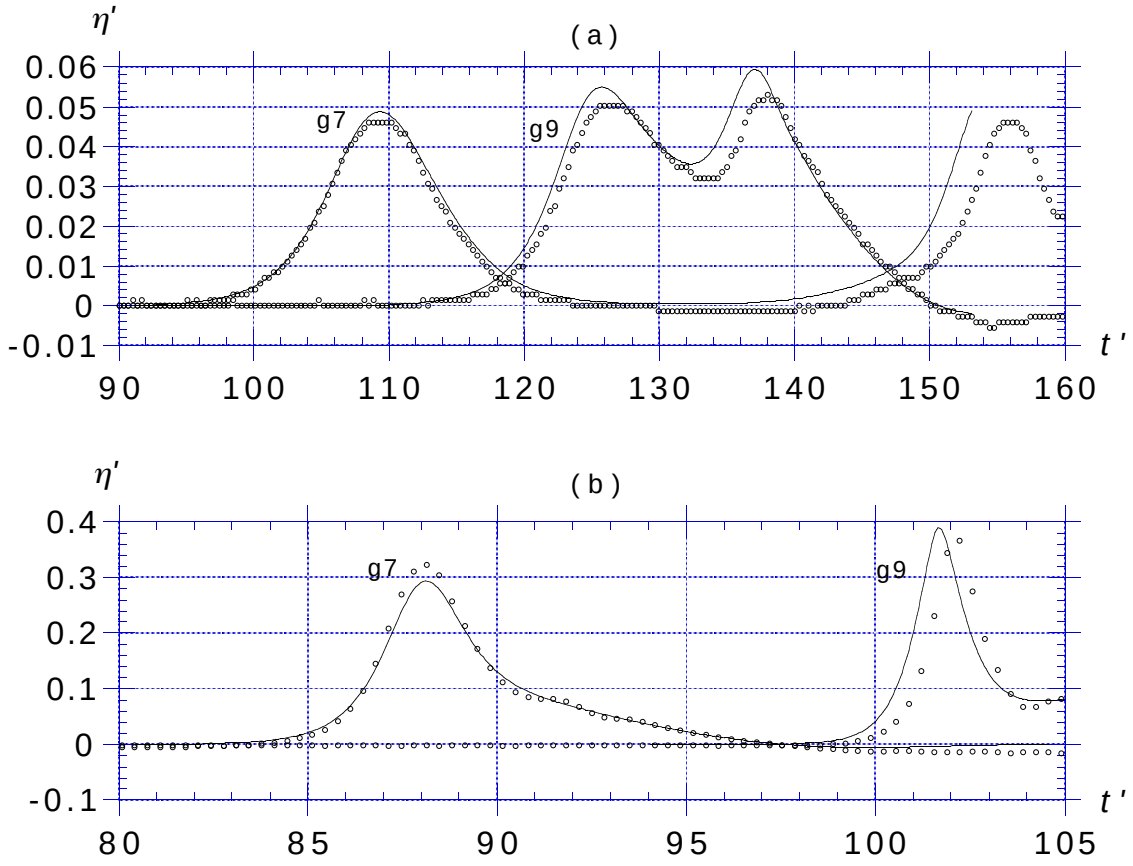

Fig. 22. Comparison of computed (——) and measured (○) free surface elevations $\eta' = \eta/h_o$ at gages 7 (g7) and 9 (g9) as a function of time t', for : (a) case A; (b) case B.

Appendix A Detailed expressions of coefficients in time updating

Detailed expressions of coefficients in Taylor series expansions (14) and (15) are given in the following.

Appendix A.1. Curvilinear coordinates

Derivations are carried out in a curvilinear coordinate system $(\mathbf{s}, \mathbf{n})$ defined along the boundary as (Fig. 3),

$$\mathbf{s} = [\cos\beta\ ,\ \sin\beta]\ ,\ \mathbf{n} = [-\sin\beta\ ,\ \cos\beta] \tag{A.1}$$

$$\cos\beta = \frac{\partial x}{\partial s}\ ,\ \sin\beta = \frac{\partial z}{\partial s} \tag{A.2}$$

where β denotes the angle between the horizontal axis x and the tangential vector $\mathbf{s}$ at the free surface.

Derivatives of vectors (**s**,**n**) with respect to their directions are obtained from Eq. (A.1) as,

$$\frac{\partial \mathbf{s}}{\partial s} = \frac{\partial \beta}{\partial s}\mathbf{n}\ ,\ \frac{\partial \mathbf{n}}{\partial s} = -\frac{\partial \beta}{\partial s}\mathbf{s} \tag{A.3}$$

$$\frac{\partial \mathbf{s}}{\partial n} = \frac{\partial \beta}{\partial n}\mathbf{n}\ ,\ \frac{\partial \mathbf{n}}{\partial n} = -\frac{\partial \beta}{\partial n}\mathbf{s} \tag{A.4}$$

Now, in a family of curves $n = \text{cst}$ and of straight lines $s = \text{cst}$ along the free surface, the derivative $\frac{\partial \beta}{\partial n}$ vanishes in Eq. (A.4).

With definitions in Eqs. (A.1) to (A.4), the curvilinear gradient operator reads,

$$\boldsymbol{\nabla} \equiv \frac{1}{h_s}\frac{\partial}{\partial s}\mathbf{s} + \frac{\partial}{\partial n}\mathbf{n} \tag{A.5}$$

where h_s is a scale factor associated with curves $n = \text{cst}$, defined along the free surface as,

$$-\frac{1}{h_s}\frac{\partial h_s}{\partial n} = \frac{1}{R} = \frac{\partial \beta}{\partial s} \quad \text{with,} \quad h_s = 1 \tag{A.6}$$

where $R(\mathbf{x})$ is the radius of curvature of the free surface. Thus, h_s is independent of s and only depends on n.

Appendix A.2. Taylor series coefficients

The kinematic free surface boundary condition Eq. (2) provides the first-order coefficient in Eq. (14) for the updating of free surface position vector $\mathbf{r}$,

$$\frac{D\mathbf{r}}{Dt} = \frac{\partial \phi}{\partial s}\mathbf{s} + \frac{\partial \phi}{\partial n}\mathbf{n} \tag{A.7}$$

Applying the material derivative Eq. (4) to Eq. (2), we get the general expression for the second-order coefficient in Eq. (14) as,

$$\frac{D^2\mathbf{r}}{Dt^2} = \frac{D\mathbf{u}}{Dt} = \frac{\partial \mathbf{u}}{\partial t} + \mathbf{u}\cdot\boldsymbol{\nabla}\mathbf{u} \tag{A.8}$$

By definition of potential theory, the first term in the right hand side of Eq. (A.8) reads,

$$\frac{\partial \mathbf{u}}{\partial t} = \boldsymbol{\nabla}\frac{\partial \phi}{\partial t} = \frac{\partial^2 \phi}{\partial t \partial s}\,\mathbf{s} + \frac{\partial^2 \phi}{\partial t \partial n}\,\mathbf{n} \tag{A.9}$$

Using the curvilinear system defined above, the second term in the right hand side of Eq. (A.8) becomes,

$$\mathbf{u}\cdot\boldsymbol{\nabla}\mathbf{u} = \boldsymbol{\nabla}\phi\cdot\Big[\frac{1}{h_s}\frac{\partial \boldsymbol{\nabla}\phi}{\partial s}\,\mathbf{s} + \frac{\partial \boldsymbol{\nabla}\phi}{\partial n}\,\mathbf{n}\Big]$$

which, using the orthogonality of $\mathbf{s}$ and $\mathbf{n}$, can be expressed as,

$$\mathbf{u}\cdot\boldsymbol{\nabla}\mathbf{u} = \frac{1}{h_s^2}\frac{\partial \phi}{\partial s}\frac{\partial \boldsymbol{\nabla}\phi}{\partial s} + \frac{\partial \phi}{\partial n}\frac{\partial \boldsymbol{\nabla}\phi}{\partial n}$$

or,

$$\begin{aligned}\mathbf{u}\cdot\boldsymbol{\nabla}\mathbf{u} \;=\; & \frac{1}{h_s^2}\frac{\partial \phi}{\partial s}\Big[\frac{1}{h_s}\Big(\frac{\partial^2 \phi}{\partial s^2}\,\mathbf{s} + \frac{\partial \phi}{\partial s}\frac{\partial \mathbf{s}}{\partial s}\Big) + \frac{\partial^2 \phi}{\partial s \partial n}\,\mathbf{n} + \frac{\partial \phi}{\partial n}\frac{\partial \mathbf{n}}{\partial s}\Big] \\ & + \frac{\partial \phi}{\partial n}\Big[\frac{1}{h_s}\mathbf{s}\,\Big(\frac{\partial^2 \phi}{\partial n \partial s} - \frac{1}{h_s}\frac{\partial h_s}{\partial n}\frac{\partial \phi}{\partial s}\Big) + \frac{\partial^2 \phi}{\partial n^2}\,\mathbf{n}\Big]\end{aligned} \tag{A.10}$$

in which $\frac{\partial \beta}{\partial n} = 0$ and $\frac{\partial h_s}{\partial s} = 0$ were used.

Using Eqs. (A.1)-(A.6), it can be shown that continuity equation $\boldsymbol{\nabla}\cdot\mathbf{u} = 0$ and irrotationality condition $\boldsymbol{\nabla}\times\mathbf{u} = 0$ transform into,

$$\frac{\partial^2 \phi}{\partial s^2} + \frac{\partial^2 \phi}{\partial n^2} - \frac{\partial \beta}{\partial s}\frac{\partial \phi}{\partial n} = 0 \tag{A.11}$$

$$\frac{\partial^2 \phi}{\partial s \partial n} = \frac{\partial^2 \phi}{\partial n \partial s} \tag{A.12}$$

respectively, along the free surface.

Hence, with Eqs. (A.11) and (A.12), Eq. (A.10) can be expressed as,

$$\mathbf{u}\cdot\boldsymbol{\nabla}\mathbf{u} = \Big\{\frac{\partial \phi}{\partial s}\frac{\partial^2 \phi}{\partial s^2} + \frac{\partial \phi}{\partial n}\frac{\partial^2 \phi}{\partial n \partial s}\Big\}\,\mathbf{s} + \Big\{\frac{\partial \phi}{\partial s}\frac{\partial^2 \phi}{\partial n \partial s} - \frac{\partial \phi}{\partial n}\frac{\partial^2 \phi}{\partial s^2} + \frac{\partial \beta}{\partial s}\Big[\Big(\frac{\partial \phi}{\partial s}\Big)^2 + \Big(\frac{\partial \phi}{\partial n}\Big)^2\Big]\Big\}\,\mathbf{n} \tag{A.13}$$

Combining Eqs. (A.8), (A.9), and (A.13), we get the final expression for the second-order coefficient in Eq. (14) as,

$$\begin{aligned}\frac{D^2\mathbf{r}}{Dt^2} \;=\; & \Big\{\frac{\partial^2 \phi}{\partial t \partial s} + \frac{\partial \phi}{\partial s}\frac{\partial^2 \phi}{\partial s^2} + \frac{\partial \phi}{\partial n}\frac{\partial^2 \phi}{\partial n \partial s}\Big\}\,\mathbf{s} + \\ & \Big\{\frac{\partial^2 \phi}{\partial t \partial n} - \frac{\partial \phi}{\partial n}\frac{\partial^2 \phi}{\partial s^2} + \frac{\partial \phi}{\partial s}\frac{\partial^2 \phi}{\partial n \partial s} + \frac{\partial \beta}{\partial s}\Big[\Big(\frac{\partial \phi}{\partial s}\Big)^2 + \Big(\frac{\partial \phi}{\partial n}\Big)^2\Big]\Big\}\,\mathbf{n}\end{aligned} \tag{A.14}$$

Similarly, dynamic free surface boundary condition Eq. (3) provides the first-order coefficient in the Taylor series (15) for the free surface potential updating. Using Eqs.

(A.5) and (A.6) we get,

$$\frac{D\phi}{Dt} = -gz + \frac{1}{2}\left[\left(\frac{\partial\phi}{\partial s}\right)^2 + \left(\frac{\partial\phi}{\partial n}\right)^2\right] - \frac{p_a}{\rho} \tag{A.15}$$

The second-order coefficient in Eq. (15) is obtained by material derivation of Eq. (3) as,

$$\frac{D^2\phi}{Dt^2} = -g\frac{Dz}{Dt} + \frac{1}{2}\,\frac{D}{Dt}(\boldsymbol{\nabla}\phi\cdot\boldsymbol{\nabla}\phi) - \frac{D}{Dt}\left(\frac{p_a}{\rho}\right) \tag{A.16}$$

with, using Eqs. (2), (A.1) and (A.5),

$$\frac{Dz}{Dt} = w = \frac{\partial\phi}{\partial n}\cos\beta + \frac{\partial\phi}{\partial s}\sin\beta \tag{A.17}$$

and, by definition of potential theory,

$$\frac{1}{2}\,\frac{D}{Dt}(\boldsymbol{\nabla}\phi\cdot\boldsymbol{\nabla}\phi) = \mathbf{u}\cdot\frac{D\mathbf{u}}{Dt} = \mathbf{u}\cdot\frac{\partial\mathbf{u}}{\partial t} + \mathbf{u}\cdot(\mathbf{u}\cdot\boldsymbol{\nabla}\mathbf{u}) \tag{A.18}$$

Now, using orthogonality of $\mathbf{s}$ and $\mathbf{n}$, and Eqs. (2), (A.7), (A.9), and (A.13), we get the first term in the right hand side of Eq. (A.18) as,

$$\mathbf{u}\cdot\frac{\partial\mathbf{u}}{\partial t} = \frac{\partial\phi}{\partial s}\frac{\partial^2\phi}{\partial t\partial s} + \frac{\partial\phi}{\partial n}\frac{\partial^2\phi}{\partial t\partial n} \tag{A.19}$$

and the second term as,

$$\mathbf{u}\cdot(\mathbf{u}\cdot\boldsymbol{\nabla}\mathbf{u}) = \frac{\partial\phi}{\partial s}\left[\frac{\partial\phi}{\partial s}\frac{\partial^2\phi}{\partial s^2} + \frac{\partial\phi}{\partial n}\frac{\partial^2\phi}{\partial n\partial s}\right] + \frac{\partial\phi}{\partial n}\left[\frac{\partial\phi}{\partial s}\frac{\partial^2\phi}{\partial n\partial s} - \frac{\partial\phi}{\partial n}\frac{\partial^2\phi}{\partial s^2} + \frac{\partial\beta}{\partial s}(\boldsymbol{\nabla}\phi\cdot\boldsymbol{\nabla}\phi)\right] \tag{A.20}$$

Finally, combining Eqs. (A.16)-(A.20) and Eq. (A.5), we get the final expression for the second-order coefficient in Eq. (15) as,

$$\begin{aligned}\frac{D^2\phi}{Dt^2} \;=\; & \frac{\partial\phi}{\partial s}\left\{\frac{\partial^2\phi}{\partial t\partial s} + \frac{\partial\phi}{\partial s}\frac{\partial^2\phi}{\partial s^2} + \frac{\partial\phi}{\partial n}\frac{\partial^2\phi}{\partial n\partial s}\right\} + \\ & \frac{\partial\phi}{\partial n}\left\{\frac{\partial^2\phi}{\partial t\partial n} - \frac{\partial\phi}{\partial n}\frac{\partial^2\phi}{\partial s^2} + \frac{\partial\phi}{\partial s}\frac{\partial^2\phi}{\partial n\partial s} + \frac{\partial\beta}{\partial s}\left[\left(\frac{\partial\phi}{\partial s}\right)^2 + \left(\frac{\partial\phi}{\partial n}\right)^2\right]\right\} - \\ & g\left\{\frac{\partial\phi}{\partial n}\cos\beta + \frac{\partial\phi}{\partial s}\sin\beta\right\} - \frac{1}{\rho}\frac{Dp_a}{Dt}\end{aligned} \tag{A.21}$$

where $\frac{Dp_a}{Dt}$ is the total rate of change of the free surface atmospheric pressure in time.

Appendix B Generation of exact solitary waves by Tanaka's method

Tanaka's[90] method is based on using Cauchy's integral theorem for the complex velocity potential, in a frame of reference moving with the wave celerity c. In this frame, the crest velocity V_c fully defines the wave field and the dimensionless crest velocity $q_c = V_c/c$ is used as a parameter for the problem. The original method by Tanaka was modified by Cooker [12] to use wave height H' instead of q_c as a parameter.

Main steps in the calculations of *exact* solitary waves of height H' are as follows (superscripts denote iteration numbers),

- An approximate initial crest velocity $\tilde{q_c^o}$ is estimated for the specified H' by interpolation in a table of (H', q_c) values predetermined within the interval $(H' = 0.833197, q_c = 0)$ for the highest possible wave (like found, e.g., in Tanaka [90]) to $(H' = 0, q_c = 1)$ for a flat free surface.
- Velocity on the free surface is calculated for the approximate crest velocity $\tilde{q_c^o}$, using the original Tanaka's method.
- Wave celerity $\tilde{c^o}$ and Froude number [r] $(\tilde{F^2})^o$ are calculated using the free surface velocities and the corresponding wave amplitude $\tilde{H'}^o$ is obtained from Bernoulli equation as,

$$\tilde{H'}^o = \frac{1}{2}\left[1 - (\tilde{q_c}^2)^o\right](\tilde{F^2})^o \tag{B.1}$$

- A better approximation for the crest velocity $\tilde{q_c}^1$ is re-estimated from $(H', \tilde{H'}^o)$ in the table of values (H', q_c).
- And so on, iteratively, until, $\Delta H' = \mid (H' - \tilde{H'}^n)/H' \mid$ is found sufficiently small [s].
- When convergence is reached for both F^2 and H', the wave shape and potential are calculated from free surface velocities. Normal velocity $\frac{\partial \phi}{\partial n}(x, t_o)$ is also calculated on the free surface at this stage (to be used as initial data for the first time step of computations with the BEM model), by noting that for a wave of constant shape,

$$\frac{\partial \phi}{\partial n}(x) = F \sin\beta(x) \tag{B.2}$$

- The wave area (or dimensionless mass) m above still water level and kinetic and potential energies (e_k, e_p) are calculated using standard integrals ($\rho' = g' = 1$),

$$\begin{aligned} m &= \rho' \int_{\Gamma_f} z' dx' \\ e_k &= \frac{1}{2}\rho' \int_{\Gamma_f} \phi \frac{\partial \phi}{\partial n} d\Gamma \\ e_p &= \frac{1}{2}\rho' g' \int_{\Gamma_f} z'^2 dx' \end{aligned} \tag{B.3}$$

- The resulting *exact* solitary wave is finally truncated left and right to points for which free surface elevation, $\eta' = \varepsilon_z H'$ (with $\varepsilon_z \ll 1$, a pre-selected threshold), and wave elevation, potential, and normal velocity are re-interpolated within a constant step grid $\Delta x'_o$, with the crest being located at a specified x'_o value, to be used as initial data in the BEM model.

[r] Tanaka's method involves an iterative solution of Cauchy's integral theorem using the Froude number as the convergence parameter. The convergence criterion selected here is 10^{-10} in relative value of F^2. It was found that 70 to 75 iterations were necessary to achieve convergence within this accuracy.

[s] The convergence criterion selected here is $\Delta H' \leq 10^{-5}$. Three to four iterations only are necessary to achieve convergence within this accuracy.

The overall method is found to be quite computationally efficient. Convergence on both F^2 and H' is reached and all wave data are calculated within less than 0.6s CPU time using 80 points on the free surface to describe the wave (for the author's program on an IBM3090/300).

Appendix C Boundary conditions for piston and flap wavemakers

Velocity and acceleration for points along a plane wavemaker boundary are derived in the following for both piston and flap type wavemakers, to be used as boundary conditions in Eq. (23).

Appendix C.1. Plane paddle wavemaker

If r_g denotes the distance between points $\boldsymbol{\alpha} = (\alpha, \beta)$ and $\mathbf{x}_g = (x_g, z_g)$ on the wavemaker (Fig. C.1), we get,

$$\begin{aligned} \alpha &= x_g + r_g \cos\theta \\ \beta &= z_g + r_g \sin\theta \end{aligned} \tag{C.1}$$

Since r_g is constant with respect to any rigid body motion, we also have,

$$\begin{aligned} \dot{\alpha} &= \dot{x_g} - r_g \sin\theta\, \dot{\theta} = \dot{x_g} - (\beta - z_g)\, \dot{\theta} \\ \dot{\beta} &= \dot{z_g} + r_g \cos\theta\, \dot{\theta} = \dot{z_g} + (\alpha - x_g)\, \dot{\theta} \end{aligned} \tag{C.2}$$

and,

$$\begin{aligned} \ddot{\alpha} &= \ddot{x_g} - r_g \cos\theta\, \dot{\theta}^2 - r_g \sin\theta\, \ddot{\theta} \\ \ddot{\beta} &= \ddot{z_g} - r_g \sin\theta\, \dot{\theta}^2 + r_g \cos\theta\, \ddot{\theta} \end{aligned}$$

or,

$$\begin{aligned} \ddot{\alpha} &= \ddot{x_g} - (\alpha - x_g)\, \dot{\theta}^2 - (\beta - z_g)\, \ddot{\theta} \\ \ddot{\beta} &= \ddot{z_g} - (\beta - z_g)\, \dot{\theta}^2 + (\alpha - x_g)\, \ddot{\theta} \end{aligned} \tag{C.3}$$

Motion and boundary conditions are expressed in the following for two standard types of plane paddle wavemakers.

Appendix C.2. Piston wavemaker

This corresponds to a flat vertical plate with $\theta = \pi/2$, horizontally moving in depth h_o (Fig. 3). The specified horizontal piston motion (stroke) is $x_p(t)$ and $u_p(x_p(t), t) = \dot{x}_p(t)$ is the stroke velocity.

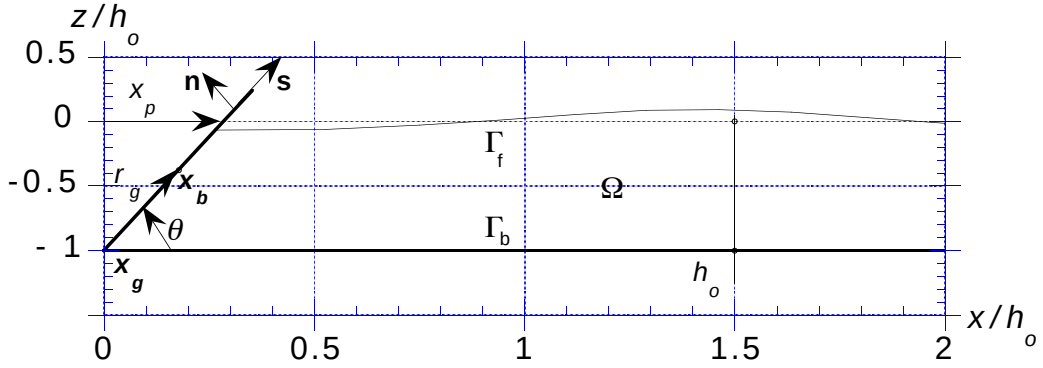

Fig. C.1. Sketch and definitions for a flap wavemaker motion on boundary Γ_{r1} of the computational domain.

Along the wavemaker paddle, by Eqs. (C.1),(C.2),(C.3), we have,

$$\begin{aligned}
&\mathbf{n} = [-1, 0], && \mathbf{s} = [0, 1], && \dot{\theta} = \ddot{\theta} = 0 \\
&\boldsymbol{\alpha} = \mathbf{x}_p = [x_p(t), z], && \dot{\boldsymbol{\alpha}} = \mathbf{u}_p = [u_p(t), 0], && \ddot{\boldsymbol{\alpha}} = \dot{\mathbf{u}}_p = [\dot{u}_p(t), 0] \\
&\dot{\boldsymbol{\alpha}} \cdot \mathbf{n} = -u_p, && \ddot{\boldsymbol{\alpha}} \cdot \mathbf{n} = -\dot{u}_p, && \dot{\boldsymbol{\alpha}} \cdot \mathbf{s} = 0
\end{aligned} \tag{C.4}$$

and from Eqs. (6),(23), and (C.4), boundary conditions on the piston wavemaker boundary read,

$$\begin{aligned}
\overline{\frac{\partial \phi}{\partial n}} &= -u_p(t) \\
\overline{\frac{\partial^2 \phi}{\partial t \partial n}} &= -\dot{u}_p(t) - u_p(t)\frac{\partial^2 \phi}{\partial s^2} \qquad \text{on } \Gamma_{r1}(t)
\end{aligned} \tag{C.5}$$

in which $\frac{\partial^2 \phi}{\partial s^2} = \frac{\partial^2 \phi}{\partial z^2}$ and $\dot{u}_p = \ddot{x}_p(t)$ denotes the specified wavemaker acceleration.

Appendix C.3. Flap wavemaker

This corresponds to a flat plate, hinged at $\mathbf{x}_g = (0, -h_o)$ on the bottom and oscillating with an angle $\theta(t) \in [\pi/2, 0]$ (defined trigonometrically with respect to the bottom; Fig. C.1). The specified horizontal piston motion (stroke) is $x_p(t)$ at $z = 0$ and $u_p(x_p(t), t) = \dot{x}_p(t)$ is the stroke velocity.

Along the wavemaker paddle, we have by Eq. (C.1),

$$\mathbf{n} = [-\sin\theta(t), \cos\theta(t)], \;\; \mathbf{s} = [\cos\theta, \sin\theta], \;\; \boldsymbol{\alpha} = \mathbf{x}_g + r_g \mathbf{s} = [\alpha(t), \beta(t)] \tag{C.6}$$

in which r_g is given by,

$$r_g(t) = \alpha(t)\cos\theta(t) + [\beta(t) + h_o]\sin\theta(t) \tag{C.7}$$

Now, by Eqs. (C.2) and (C.3), with $\dot{\mathbf{x}}_g = \ddot{\mathbf{x}}_g = 0$, we have,

$$\dot{\boldsymbol{\alpha}} = \mathbf{u}_p(t) = [-\beta(t) - h_o, \alpha(t)]\,\dot{\theta}$$

$$\ddot{\boldsymbol{\alpha}} = \dot{\mathbf{u}}_p(t) = [-\beta(t) - h_o, \alpha(t)]\,\ddot{\theta}(t) - [\alpha(t), \beta(t) + h_o]\,\dot{\theta}^2(t) \tag{C.8}$$

Hence, by (C.6),(C.7),(C.8),

$$\begin{aligned}
\dot{\boldsymbol{\alpha}} \cdot \mathbf{n} &= [\alpha(t)\cos\theta(t) + (\beta(t) + h_o)\sin\theta(t)]\,\dot{\theta}(t) \\
&= r_g(t)\,\dot{\theta}(t) \\
\ddot{\boldsymbol{\alpha}} \cdot \mathbf{n} &= [\alpha(t)\cos\theta(t) + (\beta(t) + h_o)\sin\theta(t)]\,\ddot{\theta}(t) \\
&+ [-(\beta(t) + h_o)\cos\theta(t) + \alpha(t)\sin\theta(t)]\,\dot{\theta}^2(t) \\
&= r_g(t)\ddot{\theta}(t) \\
\dot{\boldsymbol{\alpha}} \cdot \mathbf{s} &= [-(\beta(t) + h_o)\cos\theta(t) + \alpha(t)\sin\theta(t)]\,\dot{\theta}(t) \\
&= 0
\end{aligned} \tag{C.9}$$

since one can show, by simple geometric considerations, $[-(\beta + h_o)\cos\theta + \alpha\sin\theta] = 0$.

From Eqs. (6),(23), and (C.9), boundary conditions on the flap wavemaker boundary read,

$$\begin{aligned}
\overline{\frac{\partial\phi}{\partial n}} &= r_g(t)\,\dot{\theta}(t) \\
\overline{\frac{\partial^2\phi}{\partial t\partial n}} &= r_g(t)\,\ddot{\theta}(t) + \dot{\theta}(t)\,[r_g(t)\frac{\partial^2\phi}{\partial s^2} - \frac{\partial\phi}{\partial s}]
\end{aligned} \tag{C.10}$$

After some elementary developments, r_g and time derivatives of $\theta(t)$ in Eq. (C.10) can be expressed as a function of wavemaker stroke $x_p(t)$ and its time derivatives as,

$$\begin{aligned}
\dot{\theta}(t) &= -R(t)\,u_p(t) \\
\ddot{\theta}(t) &= -R(t)\,[\dot{u}_p(t) - 2\,u_p^2(t)\frac{x_p(t)}{h_o}] \\
r_g(t) &= R(t)\,\sqrt{h_o^2 + x_p^2(t)}\,[\alpha(t)\frac{x_p(t)}{h_o} + \beta(t) + h_o]
\end{aligned} \tag{C.11}$$

in which $[\alpha(t), \beta(t)]$ denote coordinates of points along the flap wavemaker and, $R(t) = h_o/(h_o^2 + x_p^2(t))$.

Appendix D Piston wavemaker motion for the generation of first-order solitary and cnoidal waves

Development of Eq. (26) is done in the following for the generation of first-order solitary or cnoidal waves by a piston wavemaker.

Appendix D.1. First-order solitary wave

The surface elevation for a *first-order* solitary wave of height H' in depth h_o is obtained as a permanent wave solution of Boussinesq equations as (e.g. Dean and Dalrymple [17]),

$$\eta'(x',t') = H'\mathrm{sech}^2[\kappa(x'-c't')] \tag{D.1}$$

where $\kappa = \sqrt{3H'}/2$ and the celerity $c' = \sqrt{1+H'}$.

Substituting Eq. (D.1) into Eq. (26) while specifying $x' = x'_p(t)$ throughout the integration gives the piston stroke required for generating the wave.

Since the wave in Eq. (D.1) extends to infinity in both directions, however, before it is used in the model, it is necessary to truncate it at some distance from the origin. Goring [25] introduced the significant horizontal extension of the wave $2\lambda'$ corresponding to a reduction in wave elevation to $\eta' = \varepsilon_z H'$ (with $\varepsilon_z \ll 1$). Using this definition and Eq. (D.1), we get,

$$\begin{aligned} \varepsilon_z H' &= H'\mathrm{sech}^2[\kappa\lambda'] \\ \varepsilon_z^{-\frac{1}{2}} &= \cosh\kappa\lambda' \end{aligned} \tag{D.2}$$

and,

$$\ell = \mathrm{arcosh}[\varepsilon_z{}^{-\frac{1}{2}}] \qquad \text{with} \qquad \lambda' = \frac{\ell}{\kappa} \tag{D.3}$$

Now (Abramowitz and Stegun [1]),

$$\mathrm{arcosh}[\varepsilon_z{}^{-\frac{1}{2}}] = \log\{\varepsilon_z{}^{-\frac{1}{2}}[1+(1-\varepsilon_z)^{\frac{1}{2}}]\} \tag{D.4}$$

Hence, since $\varepsilon_z \ll 1$,

$$\ell \simeq \log\frac{4-\varepsilon_z}{2\varepsilon_z^{\frac{1}{2}}} \tag{D.5}$$

In the numerical applications, we usually select $\varepsilon_z = 0.002$ to which it corresponds $\ell \simeq 3.80$.

Wave generation by the piston wavemaker thus starts at $t'_o = 0$ with $x' = x'_p + \lambda'$. Introducing this initial condition in the theoretical wave profile (D.1) and integrating (26) we get,

$$x'_p(t') = \frac{H'}{\kappa}\left[\tanh\chi(t') + \tanh\kappa\lambda'\right] \quad \text{with} \quad \chi(t') = \kappa(c't' - x'_p(t') - \lambda') \tag{D.6}$$

which is solved for x'_p for any given time t' using Newton iterations.

Wavemaker velocity, $u'_p(t')$ is then computed by Eq. (25) for $\eta'(x'_p(t'),t')$ and acceleration $\dot{u}'_p(t')$ is found by time derivation of the velocity,

$$\begin{aligned} u'_p(t) &= H'(1+H')^{\frac{1}{2}}\frac{1}{\cosh^2\chi(t')+H'} \\ \dot{u}'_p(t) &= \sqrt{3}\,H'^{\frac{3}{2}}(1+H')\frac{\cosh^3\chi(t')\sinh\chi(t')}{(\cosh^2\chi(t')+H')^3} \end{aligned} \tag{D.7}$$

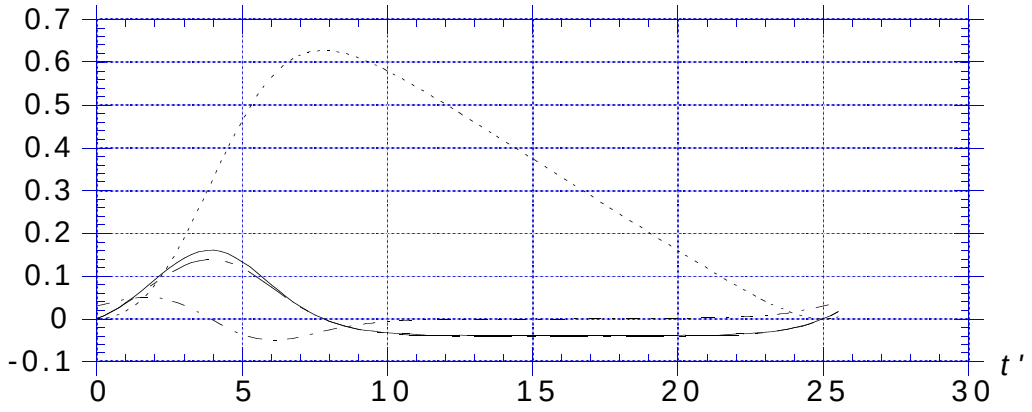

Fig. D.1. Generation of a first-order cnoidal wave by a piston wavemaker. Surface elevation and paddle motion as a function of time t', for $H' = 0.2$, $T' = 25$, with η(——), x_p(- - - -), u_p(- — -) and $\dot{u}_p$(. — .).

These values are introduced in Eq. (C.5) to define boundary conditions for the piston wavemaker.

Initial wavemaker velocity and acceleration at $t'_o = 0$ can be found as functions of H' and ε_z, by introducing Eqs. (D.3) and (D.6) into Eq. (D.7) as,

$$\begin{aligned} u'_p(t'_o) &= H'(1+H')^{\frac{1}{2}} \frac{\varepsilon_z}{1+\varepsilon_z H'} \\ \dot{u}'_p(t'_o) &= \sqrt{3}\, H'^{\frac{3}{2}} (1+H')\, \varepsilon_z \frac{(1-\varepsilon_z)^{\frac{1}{2}}}{(1+\varepsilon_z H')^3} \end{aligned} \tag{D.8}$$

which both are approximately proportional to ε_z, for a given H'. Hence, initial wavemaker acceleration, which should be kept small to avoid initial singularity problems (Section 2.2), is controlled by selecting a small enough truncation parameter ε_z. For $\varepsilon_z = 0.002$ and H'=0.5, for instance, $u_p(t_o) \simeq 0.00122\sqrt{gd}$ and $\dot{u}_p(t_o) \simeq 0.00184g$, which is quite small compared to gravity.

Appendix D.2. First-order cnoidal wave

First-order cnoidal waves are periodic wave solutions of Boussinesq equations. In water of constant depth h_o, a cnoidal wave elevation of height H', period T', and length $L' = c'T'$ is given by (e.g., Dean and Dalrymple [17]),

$$\eta'(x',t') = H'\{B + \mathrm{cn}^2[\frac{2K}{L'}(x' - c't'), m]\} \tag{D.9}$$

in which, $L' = 4K\sqrt{m/(3H')}$, the celerity $c' = \sqrt{1+AH'}$, with $A(m) = (2 - m - 3E/K)/m$, and the dimensionless trough $B(m) = (1 - m - E/K)/m$. Symbol "cn"

denotes the Jacobian elliptic function of parameter m and $(K(m), E(m))$ denote complete elliptic integrals of the 1st and 2nd kind, respectively (Abramowitz and Stegun [1]).

Substituting Eq. (D.9) into Eq. (26) while specifying $x' = x'_p(t)$ throughout the integration gives the piston stroke required for generating the wave.

Wave generation starts for $x'_p = t' = 0$ at a given initial phase $x' = \lambda'$ of the wave. Setting $x' = x'_p + \lambda'$ in Eq. (D.9) and integrating (26), we get the following equation for the stroke $x'_p(t')$,

$$x'_p(\chi(t)) = \frac{L'}{2K} H' \{ \frac{E}{mK}(\chi(t) - \chi_o) - \frac{1}{m}[E(\chi(t), m) - E(\chi_o, m)] \}$$
$$\chi(t) = \frac{2K}{L'}[x'_p(t) + \lambda' - c't'] \tag{D.10}$$

which is solved by Newton iterations for any time t'. In Eq. (D.10), $\chi_o = \lambda'(2K/L')$ and $E(\chi(t), m)$ is the incomplete elliptic integral of the 1st kind.

Finally, $u'_p(t')$ and $\dot{u}'_p(t')$ are obtained by derivation of Eq. (D.10) and introduced into Eq. (C.5) to provide boundary conditions on the wavemaker. For a cnoidal wave of height $H' = 0.2$, and period $T' = 25$, which is close to the upper limit of long wave theory, for instance, using the above equations we get $L' = 25.99$, $c' = 1.040$ and $K = 5.035$, and Fig. D.1 shows the free surface elevation and paddle motion, velocity and acceleration calculated as a function of time for these data.

In the present case, initial acceleration of the wavemaker $\dot{u}'_p(t'_o)$ varies with the selected initial phase λ' and, hence, can be made sufficiently small by adjusting the phase. For $\lambda' = 0$, for instance, initial acceleration is zero. For cnoidal waves, however, this also corresponds to maximum crest elevation and velocity. The origin can be shifted to a point with zero water elevation and velocity by selecting,

$$\lambda' = \frac{L'}{2K}[2K - \mathrm{cn}^{-1}\sqrt{-B}] + x'_p(0) \tag{D.11}$$

where $x'_p(0)$ is obtained from Eq. (D.10) with $\chi = 0$. This is the situation plotted in Fig. D.1. For this case, however, the initial acceleration is no longer zero but, for long waves, it is still quite small compared to gravity ($\mathcal{O}(4c'KH'/L')$; in Fig. D.1 the initial acceleration is about $0.03g$).

Appendix E Boundary conditions for the generation of a sum of sine waves by a flap wavemaker

Eqs. (27) and (28) used for generating sine waves with a flap wavemaker are further detailed in the following.

By analogy with the smooth initial motion obtained in Eq. (D.6) for the generation of solitary waves by a piston wavemaker, the initial damping function for sine waves is selected as,

$$\mathcal{D}(t) = \frac{1 + \varepsilon_z}{2}\left[\tanh \mu(t - t_{\varepsilon_z}) + \frac{1 - \varepsilon_z}{1 + \varepsilon_z}\right] \tag{E.1}$$

with μ, a damping coefficient obtained from the requirement that $\mathcal{D}(0) = 0$ as,

$$\mu = -\frac{1}{2\,t_{\varepsilon_z}} \log \varepsilon_z \tag{E.2}$$

One can easily check that Eqs. (E.1) and (E.2) also satisfy $\mathcal{D}(2\,t_{\varepsilon_z}) = 1 - \varepsilon_z$, which allows to select the rate of damping corresponding to given values of t_{ε_z} and ε_z. For $\varepsilon_z = 0.001$, for instance, we get $\mu \simeq 3.454/t_{\varepsilon_z}$.

In the applications, the time $2t_{\varepsilon_z}$ is selected as an integer multiple N_n of the average wave period $\tilde{T}$ of the wave components to be generated,

$$t_{\varepsilon_z} = \frac{N_n \tilde{T}}{2} \qquad \text{and} \qquad \tilde{T} = \frac{1}{n} \sum_{i=1}^{n} \frac{2\pi}{\omega_i} \tag{E.3}$$

By time derivation of Eq. (27), we get the paddle velocity and acceleration at $z = 0$ as,

$$\begin{aligned}
u_p(t) &= \dot{\mathcal{S}}\mathcal{D} + \mathcal{S}\dot{\mathcal{D}} \qquad \text{and} \qquad \dot{u}_p(t) = \ddot{\mathcal{S}}\mathcal{D} + 2\dot{\mathcal{D}}\dot{\mathcal{S}} + \mathcal{S}\ddot{\mathcal{D}} \\
\dot{\mathcal{S}}(t) &= \sum_{i=1}^{n} \frac{1}{2}\, A_i\, \omega_i \sin(\omega_i t + \varphi_i), \qquad \ddot{\mathcal{S}}(t) = \sum_{i=1}^{n} \frac{1}{2}\, A_i\, \omega_i^2 \cos(\omega_i t + \varphi_i) \\
\dot{\mathcal{D}}(t) &= \frac{\mu}{2} \frac{1 + \varepsilon_z}{\cosh^2 \mu(t - t_{\varepsilon_z})}, \qquad \ddot{\mathcal{D}}(t) = -\mu^2 (1 + \varepsilon_z) \frac{\tanh \mu(t - t_{\varepsilon_z})}{\cosh^2 \mu(t - t_{\varepsilon_z})}
\end{aligned} \tag{E.4}$$

Hence, boundary conditions (C.10) and (C.11) can be defined on the wavemaker.

The initial wavemaker velocity and acceleration at time $t_o = 0$ are obtained from (E.4) as,

$$\begin{aligned}
&\dot{\mathcal{D}}(t_o) = 2\mu\varepsilon_z \frac{1}{1 + \varepsilon_z} \qquad \text{and} \qquad \ddot{\mathcal{D}}(t_o) = 4\mu^2 \varepsilon_z \frac{1 - \varepsilon_z}{(1 + \varepsilon_z)^2} \\
&u_p(t_o) = \mathcal{S}(t_o)\dot{\mathcal{D}}(t_o) \qquad \text{and} \qquad \dot{u}_p(t_o) \simeq 2\dot{\mathcal{D}}(t_o)(\dot{\mathcal{S}}(t_o) + \mu\mathcal{S}(t_o))
\end{aligned} \tag{E.5}$$

Since for $\varepsilon_z \ll 1$, we have $\dot{\mathcal{D}}(t_o) \simeq 2\mu\varepsilon_z$ and $\ddot{\mathcal{D}}(t_o) \simeq 2\mu\dot{\mathcal{D}}(t_o)$. If we further require that $\mathcal{S}(t_o) = 0$ in Eq. (E.5), we get, $u_p(t_o) = 0$ and $\dot{u}_p(t_o) \simeq 4\mu\varepsilon_z \dot{\mathcal{S}}(t_o)$. For $\varepsilon_z = 0.001$, for instance and $\mu \simeq 1$ for $t_{\varepsilon_z} = 3.454$, the initial acceleration is $\dot{u}_p(t_o) \simeq 0.004\dot{\mathcal{S}}(t_o)$, which is thus a rather small fraction of the initial paddle velocity.

Appendix F Generation of second-order solitary and periodic waves using internal source distributions

Wave velocity distributions $u_w(x_s, z, t)$ to be used in source distributions Eqs. (31) and (33) for the generation of waves by internal sources are given in the following for second-order waves. Note that higher-order solutions (even SFW) can be used and this was recently done by Ohyama and Nadaoka[66] for 5th-order Stokes waves.

Appendix F.1. Second-order solitary waves

For a solitary wave whose *first-order* profile is given by Eq. (D.1), the horizontal velocity can be deduced as a function of depth from Boussinesq's theory (see Mei [63]). The horizontal velocity is constant over depth, to the first order in H'. Identical developments can be made up to the 2nd-order accuracy and we get,

$$u_w(x_s, z, t) = \frac{Hg}{c}\text{sech}^2\chi(t)\,[1 + (\frac{\kappa}{h_o})^2(z + h_o)^2(2\tanh^2\chi(t) + \sinh^2\chi(t))] \qquad \text{(F.1)}$$

in which $\chi(t)$ is defined as in Eq. (D.6) and the solitary wave has been limited to its significant part 2λ defined as in Eq. (D.3).

In dimensionless form, Eq. (F.1) reads,

$$u'_w(x'_s, z', t') = \frac{H'}{c'^2}\text{sech}^2\chi(t')\,[1 + (\kappa^2(z' + 1)^2(2\tanh^2\chi(t') + \sinh^2\chi(t'))] \qquad \text{(F.2)}$$

In the implementation of this procedure in the model, source strengths defined based on Eq. (F.1) correspond to Poisson equation's (10) for ϕ. For $\frac{\partial\phi}{\partial t}$, $\frac{\partial u_w}{\partial t}$ is used instead of u_w.

Appendix F.2. Second-order periodic waves

For a wave of period T and height H, the horizontal velocity calculated from Stokes theory in water of depth h_o, up to *second-order* in H/L, reads (Dean and Dalrymple [17]),

$$\begin{aligned} u_w(x_s, z, t) &= \frac{Hg}{2c}\frac{\cosh k(h_o + z)}{\cosh kh_o}\cos(kx_s - \omega t) \\ &- \frac{3H^2\omega k}{16}\frac{\cosh 2k(h_o + z)}{\sinh^4 kh_o}\cos 2(kx_s - \omega t) \end{aligned} \qquad \text{(F.3)}$$

in which, $\omega = 2\pi/T$, is the wave circular frequency, $c = \omega/k$, is the wave celerity and the wavenumber k is given by the linear dispersion relation (28).

To avoid initial singularity during a "cold start", the velocity (F.2) is multiplied by a damping function of a form similar to Eq. (E.1).

Again, source strengths defined by (F.3) correspond to the Poisson equation for ϕ. For $\frac{\partial\phi}{\partial t}$, $\frac{\partial u_w}{\partial t}$ is used instead of u_w.

6. References

1. Abramowitz, M. and Stegun, I.A. *Handbook of Mathematical Functions.* Dover Pub. Inc. New York, 1965.
2. Brebbia, C.A. *The Boundary Element Method for Engineers,* John Wiley and Sons, U.K., 1978.
3. Broeze, J., *Numerical Modelling of Nonlinear Free Surface Waves With a 3D Panel Method*. Ph.D. Dissertation, Enschede, The Netherland, 1993.

4. Brorsen, M. and Larsen, J. Source Generation of Nonlinear Gravity Waves with the Boundary Integral Method. *Coastal Engineering* **11,** 93-113, 1987.
5. Baker, G.R., Meiron, D.I. and Orszag, S.A. Generalized Vortex Method for Free-Surface Flow Problems. *J. Fluid Mech.* **123,** 477-501, 1982.
6. Camfield, F.E. and Street, R.L. Shoaling of Solitary Waves on Small Slopes. *ASCE,* **WW95,** 1-22, 1969.
7. Carrier, G.F. Gravity Waves on Water of Variable Depth. *J. Fluid Mech.* **24** (4), 641-659, 1966.
8. Carrier, G.F. and Greenspan, H.P. Water Waves of Finite Amplitude on a Sloping Beach. *J. Fluid Mech.* **4** (1), 97-110, 1958.
9. Cao, Y., Beck, R.F. and Schultz, W.W. An Absorbing Beach for Numerical Simulations of Nonlinear Waves in a Wave Tank. *Proc. 8th Intl. Workshop Water Waves and Floating Bodies* (St. John's, Newfoundland May 23-26) pps. 17-20, 1993.
10. Cointe, R. Numerical Simulation of a wave Channel. *Engng. Analysis with Boundary Elements* **7** (4), 167-177, 1990.
11. Cointe, R. Quelques aspects de la simulation numérique d'un canal à houle. *Thèse de Docteur de l'Ecole Nationale des Ponts et Chaussées,* 284 pps., 1989.
12. Cooker, M. The Interaction Between Steep Water Waves and Coastal Structures. *Ph.D. Dissertation.* School of Mathematics, University of Bristol, England, 1990.
13. Cooker, M. A Boundary-integral Method for Water Wave Motion Over Irregular Beds. *Engng. Analysis with Boundary Elements* **7** (4), 205-213, 1990.
14. Cooker, M. and Peregrine, D.H. Violent Water Motion at Breaking-Wave Impact. In *Proc. 22nd Intl. Conf. on Coastal Engineering* (ICCE22, Delft, The Netherland, July 90). Vol **1** , pps. 164-176. ASCE edition, 1991.
15. Cooker, M.J., Peregrine, D.H., Vidal, C. and Dold, J.W. The Interaction Between a Solitary Wave and a Submerged Semicircular Cylinder. *J. Fluid Mech.* **215,** 1-22, 1990.
16. Dean, R.G. Stream Function Representation of Nonlinear Ocean Wave. *J. Geophys. Res.* **70,** 4561-4572, 1965.
17. Dean, R.G. and Dalrymple R.A. *Water Wave Mechanics for Engineers and Scientists* Prentice-Hall, 1984.
18. Dold, J.W. and Peregrine, D.H. An Efficient Boundary Integral Method for Steep Unsteady water Waves. *Numerical methods for Fluid Dynamics II* (ed. K.W. Morton and M.J. Baines), pp. 671-679. Clarendon Press, Oxford, 1986.
19. Dommermuth, D.G. and Yue, D.K.P. Numerical Simulation of Nonlinear Axisymmetric Flows with a Free Surface. *J. Fluid Mech.* **178,** 195-219, 1987.
20. Dommermuth, D.G., Yue, D.K.P., Lin, W.M., Rapp, R.J., Chan, E.S. and Melville, W.K. Deep-Water Plunging Breakers : a Comparison between Potential Theory and Experiments. *J. Fluid Mech.* **189,** 423-442, 1988.
21. Driscoll, A.M., Dalrymple, R.A. and Grilli Harmonic Generation and Transmission Past a Submerged Rectangular Obstacle. In *Proc. 23rd Intl. Conf. on Coastal Engineering* (ICCE23, Venice, Italy, Oct. 92) Vol. **1**, pps. 1142-1152. ASCE edition, 1993.
22. Engquist, B. and Majda, A. Absorbing Boundary Conditions for the Numerical

Simulation of Waves. *Math. Comp.* **31,** 629-651, 1977.
23. Fenton, J.D. and Rienecker, M.M. A Fourier Method for Solving Nonlinear Water-Wave Problems : Application to Solitary-Wave Interactions. *J. Fluid Mech.* **118,** 411-443, 1982.
24. Freilich, M.H. and Guza, R.T. Nonlinear Effects on Shoaling Surface Gravity Waves *Phil. Trans. R. Soc. Lond.* **A311,** 1-41, 1984.
25. Goring D.G. Tsunamis - The Propagation of Long Waves onto a Shelf. *W.M. Keck Laboratory of Hydraulics and Water Resources, California Institute of Technology, Report No.* **KH-R-38,** 1978.
26. Gravert, P. Numerische Simulation Extremer Schwerewellen im Zeitbereich mit Direkter Randelementmethode und Zeitschrittverfahren (Ph.D. Dissertation). *Fortschritt-Berichte VDI Verlag Düsseldorf, Reihe 7 No.* **132.** 1987.
27. Greenhow, M. Wedge Entry into Initially Calm Water. *Applied Ocean Res.* **9,** 214-223, 1987.
28. Griffiths, M.W., Easson, W.J. and Greated, C.A. Measured Internal Kinematics for Shoaling Waves with Theoretical Comparisons *J. Waterways, Port Coastal and Ocean Engng.* **118** (3), 280-299, 1992.
29. Grilli, S. Wave Overturning Induced by Moving Bodies. Application to Slender Ship Wave Resistance. *Invited paper* in *Proc. 1st Intl. Conf. on Computational Modelling of Free and Moving Boundary Problems* (Southampton, England, July 91)(ed. L.C. Wrobel & C.A. Brebbia) Vol. **1**, pp. 75-90. Comp. Mech. Pub., de Gruyter, Southampton, 1991.
30. Grilli, S. Modeling of Nonlinear Wave Motion in Shallow Water. Chapter 3 in *Computational Methods for Free and Moving Boundary Problems in Heat and Fluid Flow* (eds. L.C. Wrobel and C.A. Brebbia), pps. 37-65, Comp. Mech. Pub., Elsevier Applied Sciences, London, UK, 1993.
31. Grilli, S. and Horrillo, J. Generation and Absorption of Fully Nonlinear Periodic Waves in a numerical Wave Tank. *J. Engng. Mech.,* (submitted).
32. Grilli, S., Losada, M.A. and Martin, F. Kinematics of Solitary Wave Breaking over Submerged Structures : Comparison between Nonlinear Computations and Experimental Results. In *Proc. 4th Intl. Conf. on Hydraulic Engineering Software* (HYDROSOFT92, Valencia, Spain, July 92) (eds. W.R. Blain and E. Cabrera), Fluid Flow Modelling, pp. 575-586. Comp. Mech. Pub., Elsevier Applied Science, 1992.
33. Grilli, S., Losada, M.A. and Martin, F. Wave Impact Forces on Mixed Breakwaters. In *Proc. 23rd Intl. Conf. on Coastal Engineering* (ICCE23, Venice, Italy, October 92) Vol. **1**, pps. 1161-1174. ASCE edition, 1993.
34. Grilli, S., Losada, M.A. and Martin, F. Characteristics of Solitary Wave Breaking Induced by Breakwaters. in *J. Waterway, Port, Coastal, and Ocean Engng.,* **120** (1), 74-92, 1994.
35. Grilli, S., Losada, M.A., Martin, F. and Svendsen, I.A. Nonlinear Shoaling and Impact of Waves on Coastal Structures. In *Proc. 9th Engng. Mech. Conf.* (College Station, Texas, May 92) (eds. L.D. Lutes and J.M. Niedzwecki), pp. 79-82. ASCE edition, 1992.

36. Grilli, S. Skourup, J. and Svendsen, I.A. An Efficient Boundary Element Method for Nonlinear Water Waves. *Engng. Analysis with Boundary Elements* **6** (2), 97-107, 1989.
37. Grilli, S. and Subramanya, R. Quasi-singular Integrations in the Modelling of Nonlinear Water Waves. *Engng. Analysis with Boundary Elements,* **13** (2), 181-191, 1994.
38. Grilli, S. and Subramanya, R. Recent Advances in the BEM Modelling of Nonlinear Water Waves. Chapter 4 in *Boundary Element Applications in Fluid Mechanics* (ed. H. Power), pps. 91-122. Advances in Fluid Mechanics Series. Comp. Mech. Pub., Southampton, UK, 1995.
39. Grilli, S. and Subramanya, R. Numerical Modeling of Wave Breaking Induced by Fixed or Moving Boundaries. *Computational Mechanics* (in press).
40. Grilli, S., Subramanya, R., Kirby, J.T. and Wei, J. Comparison of Modified Boussinesq and Fully Nonlinear Potential Models for Shoaling Solitary Waves. In *Proc. Intl. Symposium on Waves - Physical and Num. Modelling* (Vancouver BC, Canada, Aug. 1994) (eds. M. Isaacson and M. Quick), Vol. **1**, pps. 524-533, IAHR, 1994.
41. Grilli, S., Subramanya, R., Svendsen, I.A. and Veeramony, J. Shoaling of Solitary Waves on Plane Beaches. *J. Waterway Port Coastal and Ocean Engng.,* **120** (6), 609-628, 1994.
42. Grilli, S. and Svendsen, I.A. The Modelling of Nonlinear Water Wave Interaction with Maritime Structures. *Advances in Boundary Elements* (Proc. 11th Intl. Conf. on Boundary Elements, Cambridge, Massachusetts, USA), Vol. **2** (ed. C.A. Brebbia, J.J. Connor), pp. 253-268. Comp. Mech. Publ. Springer Verlag, Berlin, 1989.
43. Grilli, S. and Svendsen, I.A. The Modelling of Highly Nonlinear Waves : Some Improvements to the Numerical Wave Tank. *Advances in Boundary Elements* (Proc. 11th Intl. Conf. on Boundary Elements, Cambridge, Massachusetts, USA), Vol. **2** (ed. C.A. Brebbia, J.J. Connor), pp. 269-281. Comp. Mech. Pub.. Springer Verlag, Berlin, 1989.
44. Grilli, S. and Svendsen, I.A. Computation of Nonlinear Wave Kinematics during Propagation and Runup on a Slope. *Water Wave Kinematics,* (Proc. NATO-ARW, Molde, Norway, May 89) (ed. A. Torum and O.T. Gudmestad) NATO ASI Series E: Applied Sciences Vol. **178,** 387-412. Klüwer Academic Publishers, 1990.
45. Grilli, S. and Svendsen, I.A. Long Wave Interaction with Steeply Sloping Structures. In *Proc. 22nd Intl. Conf. on Coastal Engineering* (ICCE22, Delft, The Netherland, July 90) Vol. **2**, pps. 1200-1213. ASCE edition, 1991.
46. Grilli, S. and Svendsen, I.A. Corner Problems and Global Accuracy in the Boundary Element Solution of Nonlinear Wave Flows. *Engng. Analysis with Boundary Elements,* **7** (4), 178-195, 1990.
47. Grilli, S. and Svendsen, I.A. The Propagation and Runup of Solitary Waves on Steep Slopes. *Center for Appl. Coastal Res., University of Delaware, Res. Rep. No.* **91-4,** 1991.
48. Grilli, S., Svendsen, I.A. and Subramanya, R., Breaking Criterion and Characteristics for Solitary Waves on Plane Beaches. *J. Waterway Port Coastal and Ocean Engng.* (submitted).

49. Hall, J.V. and Watts, J.W. Laboratory Investigation of the Vertical Rise of Solitary Waves on Impermeable Slopes. *Beach Erosion Board, US Army Corps of Engineer, Tech. Memo. No.* **33,** 14 pp, 1953.
50. Hibberd, S. and Peregrine, D.H. Surf and Run-up on a Beach : a Uniform Bore, *J. Fluid Mech.* **95** (2), 323-345, 1979.
51. Isaacson, M. de St. Q. Nonlinear Effects on Fixed and Floating Bodies. *J. Fluid Mech.* **120,** 267-281, 1982.
52. Israeli, M. and Orszag, S.A. Approximation of Radiation Boundary Conditions. *J. Comp. Phys.* **41,** 115-135, 1981.
53. Jansen, P.C.M. A Boundary Element Model for Nonlinear Free Surface Phenomena. *Delft University of Technology, Department of Civil Engineering Report No.* **86-2,** 1986.
54. Kim, S.K., Liu, P.L.-F. and Liggett, J.A. Boundary integral Equation Solutions for Solitary Wave Generation Propagation and Run-up. *Coastal Engineering* **7,** 299-317, 1983.
55. Kirby, J.T. Intercomparison of Truncated Series Solutions for Shallow Water Waves, *J. Waterways, Port, Coastal and Ocean Engng.* **117** (2), 143-155, 1991.
56. Klopman, G. Numerical Simulation of Gravity Wave Motion on Steep slopes. *Delft Hydraulics Report No.* **H195,** 1988.
57. Kobayashi, N. DeSilva, G.S. and Watson, K.D. Wave Transformation and Swash Oscillation on Gentle and Steep Slope. *J. Geoph. Res.* **94** (C1), 951-966, 1989.
58. Larsen, J. and Dancy, H. Open Boundaries in Short Waves Simulations — A New Approach. *Coastal Engng.* **7,** 285-297, 1983.
59. Le Mehauté, B. Progressive Wave Absorber. *J. Hyd. Res.* **10(2),** 153-169, 1972.
60. Lin, W.M., Newman, J.N. and Yue, D.K. Nonlinear Forced Motion of Floating Bodies. In *Proc. 15th Intl. Symp. on Naval Hydrody., Hamburg, Germany,* 1984.
61. Liu, P.L.-F., Cho, Y.S. and Kim, S.K. A Computer Program for Transient Wave Run-up *Research Report* School of Civil and Environmental Engng., Cornell University, 1992.
62. Longuet-Higgins, M.S. and Cokelet, E.D. The Deformation of Steep Surface Waves on Water - I. A Numerical Method of Computation. *Proc. R. Soc. Lond.* **A350,** 1-26, 1976.
63. Mei, C.C *The Applied Dynamics of Ocean Surface Waves (2nd ed.).* World Scientific, New Jersey, 1989.
64. Nakayama, T. Boundary Element Analysis of Nonlinear Water Wave Problems. *Intl. J. Numer. Meth. Engng.* **19,** 953-970, 1983.
65. New, A.L., McIver, P. and Peregrine, D.H. Computation of Overturning Waves. *J. Fluid Mech.* **150,** 233-251, 1985.
66. Ohyama, T. and Nadaoka, K. Transformation of a Nonlinear Wave Train Passing Over a Submerged Shelf Without Breaking. *Coastal Engng.* **24,** 1-22, 1994.
67. Ohyama, T. and Nadaoka, K. Development of a Numerical Wave Tank for Analysis of Nonlinear and Irregular Wave Fields. *Fluid Dyn. Res.* **8,** 231-251, 1991.
68. Orlanski, I. A Simple Boundary Condition for Unbounded Hyperbolic Flows. *J. Comp. Phys.* **21,** 251-269, 1976.

69. Otta, A.K., Svendsen, I.A. and Grilli, S.T. The Breaking and Runup of Solitary Waves on Beaches. In *Proc. 23rd Intl. Conf. on Coastal Engineering* (ICCE23, Venice, Italy, October 92) Vol. **2**, pps. 1461-1474. ASCE edition, 1993.
70. Otta, A.K., Svendsen, I.A. and Grilli, S.T. Unsteady Free Surface Waves in Region of Arbitrary Shape. *CACR, University of Delaware, Res. Rep. No.* **92-10,** 153pp, 1992.
71. Pedersen, G. and Gjevik, B. Run-up of Solitary Waves *J. Fluid Mech.* **135,** 283-299, 1983.
72. Peregrine, D.H. Long Waves on Beaches, *J. Fluid Mech.* **27** (4), 815-827, 1967.
73. Peregrine, D.H. Breaking Waves on Beaches, *Ann. Rev. Fluid Mech.* **15,** 149-178, 1983.
74. Peregrine, D.H. Computation of Breaking Waves. Chapter in *Water Wave Kinematics* (ed. A. Torum and O.T. Gudmestad), NATO ASI Series E: Applied Sciences Vol. **178,** 475-490. Klüwer Academic Publishers, 1990.
75. Romate, J.E., The Numerical Simulation of Nonlinear Gravity Waves in Three Dimensions using a Higher Order Panel Method. *Ph.D. Dissertation. Department of Applied Math., University of Twente, The Netherland,* 1989.
76. Romate, J.E. The Numerical Simulation of Nonlinear Gravity Waves. *Engng. Analysis with Boundary Elements* **7** (4), 156-166, 1990.
77. Seo, Seung Nam and Dalrymple, R.A. An Efficient Model for Periodic Overturning Waves. *Engng. Analysis with Boundary Elements* **7** (4), 196-204, 1990.
78. Skjelbreia, J.E. Observations of Breaking Waves on Sloping Bottoms by Use of Laser Doppler Velocimetry, *W.M. Keck Laboratory of Hydraulics and Water Ressources, California Institute of Tech., Report No.* **KH-R-48.** 1987.
79. Skourup, J. Analytical Second-order Wavemaker Theory Verified in a Numerical Wave Flume. In *Proc. Coastal 95 Conf.* (Cancun, Mexico, Sept. 95) (eds. Brebbia, Traversoni & Wrobel), pps. 167-174. Comp. Mech. Pub., Southampton, 1995.
80. Skourup, J., Grilli, S. and Svendsen, I.A. Modelling of Steep and Breaking Waves by the Boundary Element Method. *Inst. Hydrodyn. and Hydraulic Engng., Tech. University of Denmark, Progress Rept. No.* **68,** 59-71, 1988.
81. Skyner, D.J., Gray, C. and Greated, C.A. A Comparison of Time-stepping Numerical Prediction with Whole-field Flow Measurements in Breaking Waves, Chapter in *Water Wave Kinematics* (ed. A. Torum and O.T. Gudmestad), NATO ASI Series E: Applied Sciences Vol. **178,** 491-508, 1990.
82. Sobey, R.J. and Bando, K. Variations on Higher-Order Shoaling, *J. Waterways, Port, Coastal and Ocean Engng.* **117** (4), 348-368, 1991.
83. Sommerfeld, A. *Partial Differential Equations in Physics.* Academic Press, New York, 1949.
84. Stiassnie, M. and Peregrine , D.H. Shoaling of Finite Amplitude Surface Waves on Water of Slowly-varying Depth, *J. Fluid Mech.* **97,** 783-805, 1980.
85. Subramanya, R. and Grilli, S.T. Kinematics and Properties of Fully Nonlinear Waves Shoaling and Breaking over a Gentle Slope. In *Proc. Intl. Symposium on Waves - Physical and Num. Modelling* (Vancouver BC, Canada, Aug. 1994) (eds. M. Isaacson

and M. Quick), Vol. **2**, pps. 1106-1115, IAHR, 1994.
86. Subramanya, R. and Grilli, S.T. Domain Regridding in the Computation of Nonlinear Waves. In *Proc. 2nd Intl. Workshop on Bound. Elements in Fluid Mech.* (Southampton, UK, July 1994) (eds. H. Power, C.A. Brebbia and D.B. Ingham), pps. 139-150, Comp. Mech. Pub., Southampton, 1994.
87. Svendsen, I.A. and Grilli, S. Nonlinear Waves on Steep Slopes. *J. Coastal Research* **SI 7,** 185-202, 1990.
88. Svendsen, I.A., Otta, A.K. and Grilli, S. Unsteady Free Surface Waves. In *Proc. I.U.T.A.M. Symp. on Breaking Waves* (Sidney, Australia, July 91) (eds. M.L. Banner and R.H.J. Grimshaw) pp. 229-236, Springer-Verlag, Berlin, 1992.
89. Synolakis, C.E. The Runup of Solitary Waves. *J. Fluid Mech.* **185,** 523-545, 1987.
90. Tanaka, M. The Stability of Solitary Waves. *Phys. Fluids* **29** (3), 650-655, 1986.
91. Tanaka, M., Dold, J.W., Lewy, M. and Peregrine, D.H. Instability and Breaking of a Solitary Wave. *J. Fluid Mech.* **185,** 235-248, 1987.
92. Vinje, T. and Brevig, P. Numerical Simulation of Breaking Waves. *Adv. Water Ressources* **4,** 77-82, 1981.
93. Wei, J., Kirby, J.T, Grilli, S.T. and R., Subramanya, A Fully Nonlinear Boussinesq Model for Surface Waves. I. Highly Nonlinear Unsteady Waves. *J. Fluid Mech.,* **294**, 71-92, 1995.
94. Xü, H. and D.K.P., Yue, Numerical Study of Three Dimensional Overturning Waves. In *Proc. 7th Intl. Workshop on Water Waves and Floating Bodies.* (Val de Reuil, France, May 1992)(ed. R. Cointe), Fluid Flow and Computational Aspects, pp. 303-307, 1992.
95. Yeung, R.W. Numerical Methods in Free Surface Flows. *Ann. Rev. Fluid Mech.* **14,** 395-442, 1982.
96. Zaroodny, S. J. and Greenberg, M. D. On a vortex sheet approach to the numerical calculation of water waves, *J. Comp. Phys.* **11**, 440-446, 1973.
97. Zelt, J.A. and Raichlen, F. A Lagrangian Model for Wave Induced Harbour Oscillations, *J. Fluid Mech.* **213,** 203-228, 1990.